



*Journal of Geophysical Research: Planets*

Supporting Information for

**Overview of the Morphology and Chemistry of Diagenetic Features in the Clay-Rich Glen Torridon Unit of Gale Crater, Mars**

Patrick J. Gasda<sup>1</sup>, J. Comellas<sup>1</sup>, A. Essunfeld<sup>1</sup>, D. Das<sup>2</sup>, A. B. Bryk<sup>3</sup>, E. Dehouck<sup>4</sup>, S. P. Schwenzer<sup>5</sup>, L. Crossey<sup>6</sup>, K. Herkenhoff<sup>7</sup>, J. R. Johnson<sup>8</sup>, H. Newsom<sup>6</sup>, N. L. Lanza<sup>1</sup>, W. Rapin<sup>9</sup>, W. Goetz<sup>10</sup>, P.-Y. Meslin<sup>9</sup>, J. C. Bridges<sup>11</sup>, R. Anderson<sup>7</sup>, G. David<sup>9</sup>, S. M. R. Turner<sup>5</sup>, M. T. Thorpe<sup>12</sup>, L. Kah<sup>13</sup>, J. Frydenvang<sup>14</sup>, R. Kronyak<sup>15</sup>, G. Caravaca<sup>9,16</sup>, A. Ollila<sup>1</sup>, S. Le Mouélic<sup>16</sup>, M. Nellessen<sup>6</sup>, M. Hoffman<sup>6</sup>, D. Fey<sup>16</sup>, A. Cousin<sup>9</sup>, R. C. Wiens<sup>1</sup>, S. M. Clegg<sup>1</sup>, S. Maurice<sup>9</sup>, O. Gasnault<sup>9</sup>, D. Delapp<sup>1</sup>, A. Reyes-Newell<sup>1</sup>

1) Los Alamos National Laboratory, Los Alamos, New Mexico, USA

2) McGill University, Montreal, Canada

3) University of California, Berkeley, CA, USA

4) Université de Lyon, France

5) AstrobiologyOU, School of Environment, Earth and Ecosystem Sciences, The Open University, Milton Keynes, UK.

6) University of New Mexico, Alburquerque, NM, USA

7) U.S. Geological Survey, Flagstaff, AZ, USA

8) Johns Hopkins University Applied Physics Laboratory, Laurel, MD, USA

9) IRAP, Université de Toulouse, CNRS, CNES, Toulouse, France

10) Max Planck Institute for Solar System Research, Göttingen, Germany

11) University Leicester, UK

12) Texas State University; NASA Johnson Space Center, Houston, TX, USA

13) University of Tennessee, Knoxville, TN, USA

14) Globe Institute, University of Copenhagen, Denmark

15) Jet Propulsion Laboratory, Pasadena, CA, USA

16) Laboratoire de Planétologie et Géodynamique, CNRS UMR 6112, Université Nantes, Université Angers, 44322 Nantes, France.

17) Malin Space Science Systems

**Contents of this file**

Text S1 to S9

Figures S1 to S76

Table S1

**Additional Supporting Information (Files uploaded separately)**

HTML Files S1-S2

## Introduction

The following Supporting Information provides additional information and data collected by ChemCam, Mastcam, and MAHLI. The data files include a ChemCam target-level classification and ChemCam observation-point-level chemical information for the diagenetic features observed in Glen Torridon, along with metadata associated with each target and observation point. This supplement provides a complete description of the methods used to classify targets (text S1) and a detailed description of the database (Text S1.1–S1.3). Text S3 provides additional annotated ChemCam Remote Micro Imager (RMI) images, Mastcam images, and Mars Hand Lens Imager (MAHLI) images from the full traverse that help show the reader how the images were classified. Text S4 describes additional chemical ternary diagrams that separate out the classified targets into different bedrock chemical endmembers. Text S5 shows 'edge cases' in the classification dataset, and this section describes how we decided to classify these targets in the target level classification database. Text S5 and its accompanying figures describes CaO and MgO depth profiles that can help determine whether a target is cemented. Text S6 shows phase diagram plots for some of the targets discussed in the main manuscript. Text S7 shows describes the methods for an extended calibration for lithium and related laboratory data that shows how we obtained predicted lithium values in the observation point level databases beyond the range of the current calibration for Li on Mars using ChemCam. Text S8 describes additional data for unique Na and Mg sulfate compositions detected in Glen Torridon. Text S9 lists the Mastcam and MAHLI dataproducts used for figures in the main manuscript.

### **Text S1. Dataproducts Used in Analysis; Database Structure**

We used Remote Micro Imager (RMI) mosaic images colorized by corresponding Mastcam images to look for diagenetic features in all Mount Sharp Group ChemCam targets in Glen Torridon up to the ChemCam anomaly, covering the martian solar day (sol) range 2300 to 3007. Non-colorized versions of these mosaics are available on the Public Data System (PDS).

We only analyzed Mount Sharp Group targets, and not targets from the Siccar Point Group, such as soil, dark-toned float rocks, or targets from the Greenheugh pediment. We used a target-level spreadsheet, with one row per ChemCam target, to document which points in the ChemCam Laser-Induced Breakdown Spectroscopy (LIBS) raster sampled diagenetic features, and what types of features were sampled. We then expanded this spreadsheet to include metadata about each ChemCam target.

In 17% of the ChemCam targets analyzed, an image from the Mars Hand-Lens Imager (MAHLI) instrument included that ChemCam target. In the majority of those instances, the MAHLI image was taken after ChemCam LIBS analysis of the target. When this was the case, the MAHLI image often provided higher-resolution context for the individual observation points in the ChemCam raster. This enabled greater confidence in labeling a point as having sampled specific diagenetic features, especially when such features were small and hard to resolve in the lower-resolution RMI mosaic. After analyzing all the RMI mosaics of Mount Sharp Group ChemCam targets in Glen Torridon up to sol 3007, we compiled the MAHLI images that might include overlap with a ChemCam target that either have the same target name or were recorded at the same target location. The LIBS craters, if any, captured in the MAHLI image were then annotated. Other MAHLI images, which contain the same target name in the filename, often capture the region containing the ChemCam target, but before LIBS analysis.

Moreover, some of these were covered by dust, as they did not have the benefit of dust clearing by ChemCam’s laser, or were not cleaned by the rover arm’s Dust Removal Tool (DRT), which further complicates the classification of these targets. Although this second type of corresponding MAHLI image is less useful for point-by-point analysis of the raster, these ‘before’ images still help provide context and offer a higher-resolution view of the ChemCam target.

When this analysis was complete, every Mount Sharp Group target in Glen Torridon was listed in the target-level spreadsheet, regardless of whether it sampled some diagenetic feature. The type of feature(s) observed in each target and the chemical enrichments present in those feature(s) were also documented in this spreadsheet. To document the chemistry of the features, we first compiled all of the relevant ChemCam data products. We then processed the LIBS data products (CL5\* file types) to obtain major oxide compositions ( $\text{SiO}_2$ ,  $\text{TiO}_2$ ,  $\text{Al}_2\text{O}_3$ ,  $\text{FeO}_{\text{T}}$ ,  $\text{MgO}$ ,  $\text{CaO}$ ,  $\text{Na}_2\text{O}$ ,  $\text{K}_2\text{O}$ , and  $\text{MnO}$ ) for each observation point in the raster (Clegg et al., 2017; Gasda et al., 2021). We also processed the data to obtain minor element compositions for each observation point in the raster (e.g., Payré et al., 2017a). We used this compositional information to create 5 new subsheets: one for each major category of diagenetic feature tracked (nodules, nodular bedrock, veins, cements, dark-toned strata). These are the observation-point-level, or point-level, subsheets where each row contains chemical information and metadata about a unique observation point in a ChemCam raster. Some targets have multiple entries on a single subsheet if more than one observation point from that target hit that type of diagenetic feature. Similarly, a given target may appear in multiple subsheets if some of its observation points sampled different types of diagenetic features.

Because each diagenetic feature is represented with a subsheet, observation points that did not sample a diagenetic feature (“non-diagenetically-interesting points”) are not included in the observation point level subsheets. Therefore, a key difference exists between the target-level sheet and the point-level subsheets: the target-level sheet represents a complete record of all Mount Sharp Group targets in Glen Torridon up to sol 3007. However, the point-level subsheets only contain the points that sampled the specific diagenetic feature tracked in that subsheet.

For specific information about the columns of the target-level sheet, see the Target Classification section. For specific information about the columns of the observation-point-level subsheets, see the Observation Point Classification section. The database, in \*.csv file format, can be found on the PDS (Gasda et al., 2021b).

#### *Text S1.1. Target Classification*

The target classification spreadsheet has two header rows; the first row contains column category labels, and the second row contains specific column headers. After the second row, each row of the sheet contains information about a unique ChemCam target.

#### Column Categories

Identification (ID)

Localization (LOC)

RMI-level diagenesis (RMI-D)  
Raster-level diagenesis (RAS-D)  
Diagenetic feature chemical enrichments (DFCE)  
Geochemical Context (GCON)  
Miscellaneous (MISC)  
ArcGIS category (GIS)

#### Columns by Category

ID columns:

*Target*: The name of the ChemCam target

*SeqID*: The Sequence Identification number for the ChemCam target

*Sol*: The martian solar day this ChemCam target was observed

*Spacecraft Clock Range*: The spacecraft clock values corresponding to the first and last observation points in the raster on this target, separated by a semicolon

*Distance (m)*: The distance from ChemCam to the ChemCam target, measured in meters

*Raster size*: The number of observation points in the raster for this target

LOC columns:

*Elevation (m)*: The elevation of the target with respect to the mean Mars datum, measured in meters

*Latitude (dd)*: Decimal degrees latitude of the target relative to Mars Orbital Laser Altimeter (MOLA 2000)

*Longitude (dd)*: Decimal degrees longitude of the target relative to MOLA 2000

*Easting (m)*: Meters (East: +; West: -)

*Northing (m)*: Meters (North: +; South: -)

RMI-D columns:

*RMI has veins*: A one or zero indicating whether a vein was (1) or was not (0) seen in the remote micro image (RMI) taken with the ChemCam observation

*RMI has nodules*: A one or zero indicating whether nodules were (1) or were not (0) seen in the remote micro image (RMI) taken with the ChemCam observation

*RMI has nodules with diagenetic halos*: A one or zero indicating whether nodules with diagenetic halos were (1) or were not (0) seen in the remote micro image (RMI) taken with the ChemCam observation

*RMI has dark strata nodules/ceements*: A one or zero indicating whether dark strata nodules or cements were (1) or were not (0) seen in the remote micro image (RMI) taken with the ChemCam observation

RAS-D columns:

*Raster Hits Diagenetic Feature*: A one or zero indicating whether any diagenetic feature (vein; concretion; nodular bedrock; nodules with diagenetic halos; or calcium-sulfate cement) was (1) or was not (0) sampled with the laser in one or more observation point in this ChemCam target

*Raster hits veins*: A one or zero indicating whether a vein was (1) or was not (0) directly sampled with the laser in one or more observation point in this ChemCam target

*Raster hits nodules*: A one or zero indicating whether nodules were (1) or were not (0) directly sampled with the laser in one or more observation point in this ChemCam target

*Raster hits nodular bedrock*: A one or zero indicating whether the bedrock surrounding nodules, not the nodules themselves, was (1) or was not (0) directly sampled with the laser in one or more observation point in this ChemCam target

*Raster hits nodules with diagenetic halos*: A one or zero indicating whether nodules with diagenetic halos were (1) or were not (0) directly sampled with the laser in one or more observation point in this ChemCam target

*Raster hits calcium-sulfate cement*: A one or zero indicating whether calcium-sulfate cement was (1) or was not (0) directly sampled with the laser in one or more observation point in this ChemCam target

*Vein points*: A semicolon-separated list of the observation points that directly sampled vein material on this ChemCam target; if 0, then no observation points directly sampled veins

*Nodule points*: A semicolon-separated list of the observation points that directly sampled nodules on this ChemCam target; if 0, then no observation points directly sampled nodules

*Nodular bedrock points*: A semicolon-separated list of the observation points that sampled the bedrock surrounding nodules, not the nodules themselves, on this ChemCam target; if 0, then no observation points directly sampled nodular bedrock

*Nodule-with-diagenetic-halo points*: A semicolon-separated list of the observation points that directly sampled nodules with diagenetic halos on this ChemCam target; if 0, then no observation points directly sampled nodules with diagenetic halos

*Calcium-sulfate cement points*: A semicolon-separated list of the observation points that directly sampled calcium-sulfate cement material on this ChemCam target; if 0, then no observation points directly sampled calcium-sulfate cement (calcium-sulfate cement points are enriched in Ca and exhibit S detection). Calcium-sulfate cement points are mutually exclusive with nodular bedrock points, although some nodular bedrock points exhibit enrichment in Ca and have S present. These points are noted in the observation-point-level subsheets.

#### DFCE columns:

The diagenetic feature chemical enrichment columns compile information from the enrichment columns of the observation-point-level subsheets for the three largest categories of the diagenetic features: veins, nodules, and nodular bedrock. A single observation point can have multiple chemical enrichments but only one strongest enrichment. For a detailed description of the enrichment determination process, see the Methods section of the manuscript.

#### *Vein enrichments*:

Not Applicable: Raster did not sample a vein on this target

NE: None of the observation points that sampled a vein on this target were enriched in any of the following elements: Na, Mg, Ca, Mn, Fe

Semicolon-separated list (or single entry if only one): the chemical enrichment(s) exhibited by observation points that sampled a vein on this target

*Vein strongest enrichments:*

Not Applicable: Raster did not sample a vein on this target

NE: None of the observation points that sampled a vein on this target were enriched in any of the following elements: Na, Mg, Ca, Mn, Fe

Semicolon-separated list (or single entry if only one): the strongest chemical enrichment(s) exhibited by observation points that sampled a vein on this target

*Nodule enrichments:*

Not Applicable: Raster did not sample nodules on this target

NE: None of the observation points that sampled nodules on this target were enriched in any of the following elements: Na, Mg, Ca, Mn, Fe

Semicolon-separated list (or single entry if only one): the chemical enrichment(s) exhibited by observation points that sampled nodules on this target

*Nodule strongest enrichments:*

Not Applicable: Raster did not sample nodules on this target

NE: None of the observation points that sampled nodules on this target were enriched in any of the following elements: Na, Mg, Ca, Mn, Fe

Semicolon-separated list (or single entry if only one): the strongest chemical enrichment(s) exhibited by observation points that sampled nodules on this target

*Nodular bedrock enrichments:*

Not Applicable: Raster did not sample nodular bedrock on this target

NE: None of the observation points that sampled nodular bedrock on this target were enriched in any of the following elements: Na, Mg, Ca, Mn, Fe

Semicolon-separated list (or single entry if only one): the chemical enrichment(s) exhibited by observation points that sampled nodular bedrock on this target

*Nodular bedrock strongest enrichments:*

Not Applicable: Raster did not sample nodular bedrock on this target

NE: None of the observation points that sampled nodular bedrock on this target were enriched in any of the following elements: Na, Mg, Ca, Mn, Fe

Semicolon-separated list (or single entry if only one): the strongest chemical enrichment(s) exhibited by observation points that sampled nodular bedrock on this target

*Hits vein with mixed composition:* A one or zero indicating whether the raster does (1) or does not (0) contain at least one observation point that sampled a vein and registered  $\text{CaO} < 20 \text{ wt.\%}$  or  $\text{FeO}_T > 13 \text{ wt.\%}$

*Hits vein with pure composition:* A one or zero indicating whether the raster does (1) or does not (0) contain at least one observation point that sampled a vein and registered  $\text{CaO} \geq 20 \text{ wt.\%}$  and  $\text{FeO}_T \leq 13 \text{ wt.\%}$

*Hits vein with non-CaO-rich composition:* A one or zero indicating whether the raster does (1) or does not (0) contain at least one observation point which, per the RMI, seems to have sampled a vein, but does not register a CaO wt.% prediction that is enriched with respect to the local bedrock (these observation points all contain specific notes in the Notes column of the Veins subsheet)

GCON columns:

*Formation*: Geologic formation for this ChemCam target (all are Mount Sharp Group)

*Stratigraphic Member*: Stratigraphic member for this ChemCam target (one of: Jura; Knockfarril Hill (KfH); Glasgow; KH-GG transition)

*Chemical Endmember*: Chemical endmember for this ChemCam target, used in determining chemical enrichment: coherent; rubbly; Glasgow; Hutton; Groken/Mary Anning. The “Coherent” label appears three ways in the database: “Coherent”, “Coherent-default”, and “Coherent-missing.” We used the classification by Dehouck et al. (2022) to assign labels to individual observation points. For a detailed description of this labeling process, see the Chemical Endmember Label Assignment section of the Supplement. When the unique identifier for an observation point existed in the (Dehouck et al., 2022) database, and the word “coherent” was present in the label for that observation point, we applied the label “Coherent.” When the unique identifier for the observation point was in that database, but the label in the (Dehouck et al., 2022) database did not satisfy any of the criteria to have a specific label parsed, we assigned it “Coherent-default.” And when the unique identifier for an observation point was simply missing from that database, we labeled it “Coherent-missing.” We used Spacecraft Clock, a 9-digit number measuring seconds from January 1st, 2000, parsed from the filename, as the unique identifier for observation points.

MISC columns:

*Corresponding MAHLI Target;Sol*: MAHLI target name and sol number for the MAHLI image overlapping this ChemCam target, separated by a semicolon, if such an image was recorded for this target.

*Notes*: Miscellaneous notes about the target or occasionally about the corresponding MAHLI image.

Often to draw attention to oddities and justify classification in strange cases.

GIS columns:

To plot targets with ArcGIS, we checked applicability for each target across 16 attributes:

- 1: Target sampled special veins (MgO-enriched or MnO-, FeOT-enriched veins)
- 2: Target sampled MnO-enriched nodule
- 3: Target sampled FeOT-enriched nodule
- 4: Target sampled MgO-enriched nodule
- 5: Target sampled CaO-enriched nodule
- 6: Target sampled Na<sub>2</sub>O-enriched nodule
- 7: Target sampled NE nodule (not enriched)
- 8: Target sampled MnO-enriched nodular bedrock
- 9: Target sampled FeOT-enriched nodular bedrock
- 10: Target sampled MgO-enriched nodular bedrock
- 11: Target sampled CaO-enriched nodular bedrock
- 12: Target sampled Na<sub>2</sub>O-enriched nodular bedrock
- 13: Target sampled NE nodular bedrock (not enriched)

- 14: Target sampled CaSO<sub>4</sub>-cemented nodular bedrock
- 15: Target sampled CaSO<sub>4</sub> cement
- 16: Target sampled or saw vein

If attribute “k” was applicable to a target, the column “GIS k” received the number “k” in that target’s row. If none of the attributes were applicable to a given target, then that target got a “0” in the “GIS o” column. The “Minimum GIS label” column took the minimum number from among the applicable attributes for a given target to filter importance of attributes hierarchically. The expanded GIS label columns GIS o – GIS 16 are included along with the “Minimum GIS label” column to allow for simple plotting of different slices of the target classification by diagenetic attribute.

#### *Text S1.2. Observation Point Classification*

Using the semicolon-separated lists of observation points from the target classification database RAS-D columns, we created five observation-point-level subsheets, or point-level subsheets: one for each type of diagenetic feature tracked. This resulted in the following: nodules.csv, nodule-rich-bedrock.csv, veins.csv, cements.csv, and dark-strata.csv. Each subsheet contains exclusively the ChemCam observation points that sampled the type of diagenetic feature after which the subsheet is named. These subsheets include identification metadata for the observation point, as well as its Major Oxide Composition predictions (MOC) and Minor Element values (ME).

#### Column Categories

- Identification (ID)
- Localization (LOC)
- Major Oxide Composition (MOC)
- Laser metadata (LASER)
- Minor Elements (ME)
- Chemical Enrichment (CE)
- Miscellaneous (MISC)

#### Columns by Category

ID columns:

*File*: The ChemCam filename corresponding to the observation point represented in that row of the subsheet and processed to obtain compositional information

*Spacecraft Clock*: A 9-digit number measuring seconds from January 1st, 2000, parsed from the filename, used as the unique identifier for this observation point

*Target*: The name of the ChemCam target of which this observation point is a member

*SeqID*: The Sequence ID number for the ChemCam target of which this observation point is a member

*Sol*: The martian solar day on which the ChemCam target of which this observation point is a member was observed

*Observation Point*: The number (1-indexed) for this observation point in the context of its ChemCam target’s raster

LOC columns:

*Elevation*: The elevation of the target with respect to the mean Mars datum, measured in meters

MOC columns:

The information in the Major Oxide Composition columns is derived from processing ChemCam spectral data (Clegg et al., 2017; Gasda et al., 2021). For each quantified element, there are three informational columns: The predicted compositional value (in weight percent, or wt.%); the accuracy for that value (RMSEP, wt%); and the standard deviation in predictions for that element across the laser shots for the observation point.

$\text{SiO}_2$ : Predicted silicon dioxide composition for this observation point (measured in weight percent, or wt.%)

$\text{SiO}_2 \text{ RMSEP}$ : Root Mean Square Error Prediction for the predicted silicon dioxide composition for this observation point (measured in weight percent, or wt.%)

$\text{SiO}_2 \text{ shots stdev}$ : Standard Deviation in silicon dioxide predictions across the laser shots comprising this observation point (wt%)

$\text{TiO}_2$ : Predicted titanium dioxide composition for this observation point (measured in weight percent, or wt.%)

$\text{TiO}_2 \text{ RMSEP}$ : Root Mean Square Error Prediction for the predicted titanium dioxide composition for this observation point (measured in weight percent, or wt.%)

$\text{TiO}_2 \text{ shots stdev}$ : Standard Deviation in titanium dioxide predictions across the laser shots comprising this observation point

$\text{Al}_2\text{O}_3$ : Predicted aluminum oxide composition for this observation point (measured in weight percent, or wt.%)

$\text{Al}_2\text{O}_3 \text{ RMSEP}$ : Root Mean Square Error Prediction for the predicted aluminum oxide composition for this observation point (measured in weight percent, or wt.%)

$\text{Al}_2\text{O}_3 \text{ shots stdev}$ : Standard Deviation in aluminum oxide predictions across the laser shots comprising this observation point

$\text{FeO}_T$ : Predicted total iron oxide composition for this observation point (measured in weight percent, or wt.%)

$\text{FeO}_T \text{ RMSEP}$ : Root Mean Square Error Prediction for the predicted total iron oxide composition for this observation point (measured in weight percent, or wt.%)

$\text{FeO}_T \text{ shots stdev}$ : Standard Deviation in total iron oxide predictions across the laser shots comprising this observation point

$\text{MgO}$ : Predicted magnesium oxide composition for this observation point (measured in weight percent, or wt.%)

$\text{MgO} \text{ RMSEP}$ : Root Mean Square Error Prediction for the predicted magnesium oxide composition for this observation point (measured in weight percent, or wt.%)

$\text{MgO} \text{ shots stdev}$ : Standard Deviation in magnesium oxide predictions across the laser shots comprising this observation point

$\text{CaO}$ : Predicted calcium oxide composition for this observation point (measured in weight percent, or wt.%)

*CaO RMSEP*: Root Mean Square Error Prediction for the predicted calcium oxide composition for this observation point (measured in weight percent, or wt.%)

*CaO shots stdev*: Standard Deviation in calcium oxide predictions across the laser shots comprising this observation point

*Na<sub>2</sub>O*: Predicted sodium oxide composition for this observation point (measured in weight percent, or wt.%)

*Na<sub>2</sub>O RMSEP*: Root Mean Square Error Prediction for the predicted sodium oxide composition for this observation point (measured in weight percent, or wt.%)

*Na<sub>2</sub>O shots stdev*: Standard Deviation in sodium oxide predictions across the laser shots comprising this observation point

*K<sub>2</sub>O*: Predicted potassium oxide composition for this observation point (measured in weight percent, or wt.%)

*K<sub>2</sub>O RMSEP*: Root Mean Square Error Prediction for the predicted potassium oxide composition for this observation point (measured in weight percent, or wt.%)

*K<sub>2</sub>O shots stdev*: Standard Deviation in potassium oxide predictions across the laser shots comprising this observation point

*MnO*: Predicted manganese oxide composition for this observation point (measured in weight percent, or wt.%)

*MnO RMSEP*: Root Mean Square Error Prediction for the predicted manganese oxide composition for this observation point (measured in weight percent, or wt.%)

*MnO shots stdev*: Standard Deviation in manganese oxide predictions across the laser shots comprising this observation point

*Sum of Oxides*: Sum of the wt.% predictions for SiO<sub>2</sub>, TiO<sub>2</sub>, Al<sub>2</sub>O<sub>3</sub>, FeO<sub>T</sub>, MgO, CaO, Na<sub>2</sub>O, K<sub>2</sub>O, and MnO for this observation point

#### LASER columns:

*Distance (m)*: The distance from ChemCam to this observation point, measured in meters

*Laser Power*: The laser power used in the LIBS analysis of this observation point

*Spectrum Total*: The total intensity in all spectrometers of the averaged spectrum for this observation point

#### ME columns:

The information in the Minor Elements columns is derived from processing ChemCam spectral data (e.g., Payré et al., 2017a). For each of the minor elements Li, Rb, and Sr, there are three columns: peak area, prediction, and prediction RMSE. The numbers in the “peak area” columns represent the area under the curve fitted to the peaks in the ChemCam spectrum associated with these elements. The peak area values provide a qualitative measure of the abundance (generally, higher peak area corresponds to more of that element). The “prediction” columns give the predicted concentration of the element (Payre et al., 2017a) in parts per million (ppm). The “prediction RMSE” columns give the accuracy of the predictions in the “prediction” columns.

*Cr (peak area)*: Peak area for the chromium peak(s) in the ChemCam spectrum for this observation point

*Li (peak area)*: Peak area for the lithium peak(s) in the ChemCam spectrum for this observation point  
*Li prediction (ppm)*: Li prediction using for predictions  $\leq$  72 ppm (Payré et al., 2017a) and for predictions  $>$  72 ppm (Supplement Text S6).

*Li prediction RMSE (ppm)*: Accuracy for Li prediction using (Payré et al., 2017a) for predictions  $\leq$  72 ppm and for predictions  $>$  72 ppm (Supplement Text S6).

*Rb (peak area)*: Peak area for the rubidium peak(s) in the ChemCam spectrum for this observation point  
*Rb prediction (ppm)*: Rb prediction using (Payré et al., 2017a)

*Rb prediction RMSE (ppm)*: Accuracy for Rb prediction using (Payré et al., 2017a)

*Sr (peak area)*: Peak area for the strontium peak(s) in the ChemCam spectrum for this observation point

*Sr prediction (ppm)*: Sr prediction using (Payré et al., 2017a)

*Sr prediction RMSE (ppm)*: Accuracy for Sr prediction using (Payré et al., 2017a)

#### CE columns:

See the Definitions subsection of Methods section of manuscript for a detailed description of how chemical enrichments are determined for ChemCam observation points.

*Na<sub>2</sub>O-rich*: A one or zero indicating whether this observation point is (1) or is not (0) enriched in Na<sub>2</sub>O with respect to the median bedrock for its chemical endmember

*MgO-rich*: A one or zero indicating whether this observation point is (1) or is not (0) enriched in MgO with respect to the median bedrock for its chemical endmember

*CaO-rich*: A one or zero indicating whether this observation point is (1) or is not (0) enriched in CaO with respect to the median bedrock for its chemical endmember

*MnO-rich*: A one or zero indicating whether this observation point is (1) or is not (0) enriched in MnO with respect to the median bedrock for its chemical endmember

*FeO<sub>T</sub>-rich*: A one or zero indicating whether this observation point is (1) or is not (0) enriched in FeO<sub>T</sub> with respect to the median bedrock for its chemical endmember

*Strongest Enrichment*: The oxide (one of Na<sub>2</sub>O, MgO, CaO, MnO, or FeO<sub>T</sub>) that has the highest degree of enrichment determined by the ratio of the predicted observation point oxide composition (wt.%) and the median bedrock oxide composition value (wt.%).

#### GCON columns:

*Chemical Endmember*: Chemical endmember for this observation point, used in determining chemical enrichment: coherent; rubbly; Glasgow; Hutton; Groken/Mary Anning. The “Coherent” label appears three ways in the subsheet: “Coherent”, “Coherent-default”, and “Coherent-missing.” We used the classification by Dehouck et al., (2021) to assign labels to individual observation points. For a detailed description of this labeling process, see the [Chemical Endmember Label Assignment](#) section of the Supplement. We used Spacecraft Clock, a 9-digit number measuring seconds from January 1st, 2000, parsed from the filename, as the unique identifier for observation points.

#### MISC columns:

Not all of the columns listed in the MISC category appear in every point-level subsheet. Some appear in only one of the point-level subsheets, while others appear in several subsheets. The subsheets in which each MISC-category column appears are listed in brackets after the column name.

*Notes (all)*: Miscellaneous notes about the observation point or occasionally about the target this point is a part of. Often to draw attention to oddities and justify classification.

*P detected (nodules, nodule-rich bedrock)*: A one or zero indicating whether phosphorus was (1) or was not (0) detected in the ChemCam spectrum at 602.5, 603.5, or 255.4 nm (e.g., Payré et al., 2017b; Meslin et al., 2018) for this observation point. If this observation point's spectrum was not analyzed for phosphorus detection, that is stated explicitly in this column.

*S detected (nodule-rich bedrock, cements)*: A one or zero indicating whether sulfur was (1) or was not (0) detected in the ChemCam spectrum for this observation point (e.g., Payré et al., 2017b). If this observation point's spectrum was not analyzed for sulfur detection, that is stated explicitly in this column.

*Vein composition (veins)*: A qualitative description of the composition of the vein sampled by this observation point: pure ( $>20$  wt.% CaO and  $<13$  wt.% FeOT); mixed ( $\leq 20$  wt.% CaO or  $\geq 13$  wt.% FeOT); or non-CaO-rich (not enriched in CaO with respect to the median bedrock value for its chemical endmember; more detail in the *Notes* accompany each instance of this composition)

*B detected (veins)*: A numerical value representing boron peak area (Gasda et al., 2017) in the spectrum for this observation point, indicating that it was analyzed for boron detection. If this observation point's spectrum was not analyzed for boron detection, that is stated explicitly in this column.

#### *Text S1.3. Chemical Endmember Label Assignment*

To rigorously determine chemical enrichments with respect to the median values for the local bedrock (Table S1), we had to determine the chemical endmember for each observation point. Table S1 summarizes the median values of the local bedrock (all observation points not on diagenetic features determined through our classification, out of focus points, or regolith). In Table S1, we list both the RMSEP accuracy and the interquartile range. RMSEP accuracy is used to determine enrichments in the database and subsheets, and the interquartile range is shown on ternary plots in the main manuscript and in the supplement. We did this using data from Dehouck et al. (2022), which contained almost every ChemCam observation point in this analysis with notes regarding the “unit,” or chemical endmember, for that observation point.



We assigned chemical endmembers as follows:

*Rubbly*: If the sol was outside the range (2825, 2922) and the word “rubbly” (case-insensitive) appeared in the notes in the classification by Dehouck et al., (2021), it was labeled “Rubbly”

*Coherent*: If the sol was outside the range (2829, 2923) and the word “rubbly” did not appear in the notes in the classification by Dehouck et al. (2022) but the word “coherent” *did* appear, the point was labeled “Coherent”

*Hutton*: These targets are intended to be the targets that correspond to the top of Tower and Western buttes, which had a unique chemical signature (see manuscript). If none of the conditions for labeling the point “Groken/Mary Anning”, “Rubbly”, or “Coherent” applied, but any of the following four conditions applied, it was labeled “Hutton”: (1) the phrase “top tower” appeared in the notes (case-insensitive); (2) the phrase “top western” appeared in the notes (case-insensitive).

*Glasgow*: These targets are intended to be the targets in the Glasgow stratigraphic unit, but that were not in the locations labeled “Hutton” (see manuscript). If none of the conditions for labeling the point “Groken/Mary Anning”, “Rubbly”, “Coherent”, or “Hutton” applied, but the term “Glasgow” appeared in the notes (case-insensitive), it was labeled “Glasgow.”

*Groken/Mary Anning*: These targets are intended to be the targets that correspond to the Groken and Mary Anning drill sample sites. If the sol for a point fell between 2825 and 2922, inclusive [2825, 2922], it was labeled “Groken/Mary Anning.”

*Coherent-default*: If none of the aforementioned conditions applied, but the filename or Spacecraft Clock was present in the classification by Dehouck et al. (2022), it was labeled “Coherent” by default, and this was indicated by the label containing the word “default.”

*Coherent-missing*: If the unique identifier for this observation point was missing from the classification by Dehouck et al. (2022), entirely, it was labeled “Coherent” by default, and the fact that it was missing was indicated by the label containing the word “missing.”

## **Text S2. Diagenetic Features observed over traverse**

In Figures S1–S35 we show ChemCam, Mastcam, and MAHLI targets that illustrate the large diversity of features observed in Glen Torridon. These images are annotated to show the presence of diagenetic features and are described in the manuscript.



Figure S1: Kilmarie Drill Hole Mastcam image (2387MR0126780001002184C00) showing typical cross-cutting veins in the bedrock in the Jura member in GT; Drill hole is ~4 cm in size. Nearby Ca-sulfate ChemCam target River Spey (sol 2399) is labeled.

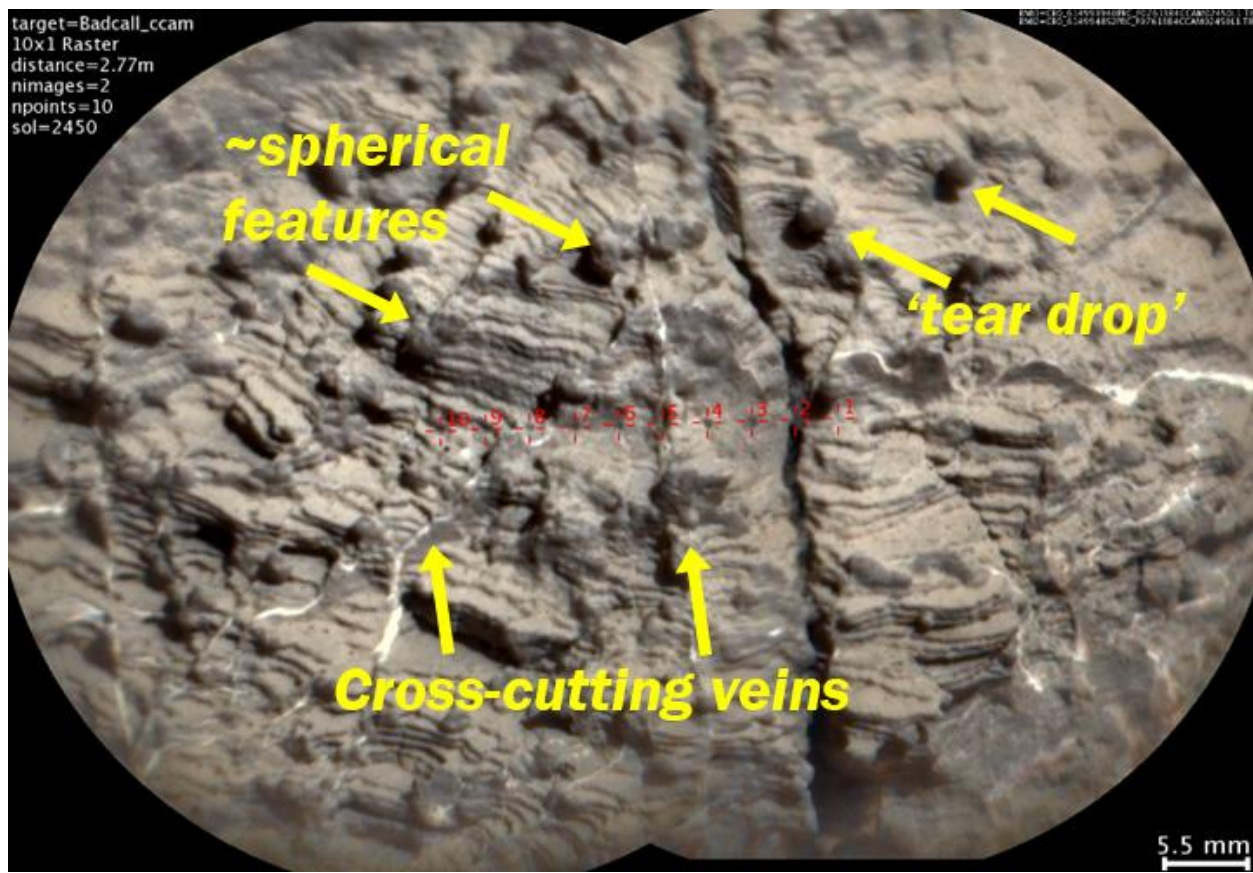


Figure S2: The Badcall ChemCam target RMI (sol 2450) colorized with Mastcam image 2450MR0130010001003711Coo.

**Sol 2450 – Target Badcall**  
**Focus merge product from ~ 5 cm standoff**

Rotated 90°

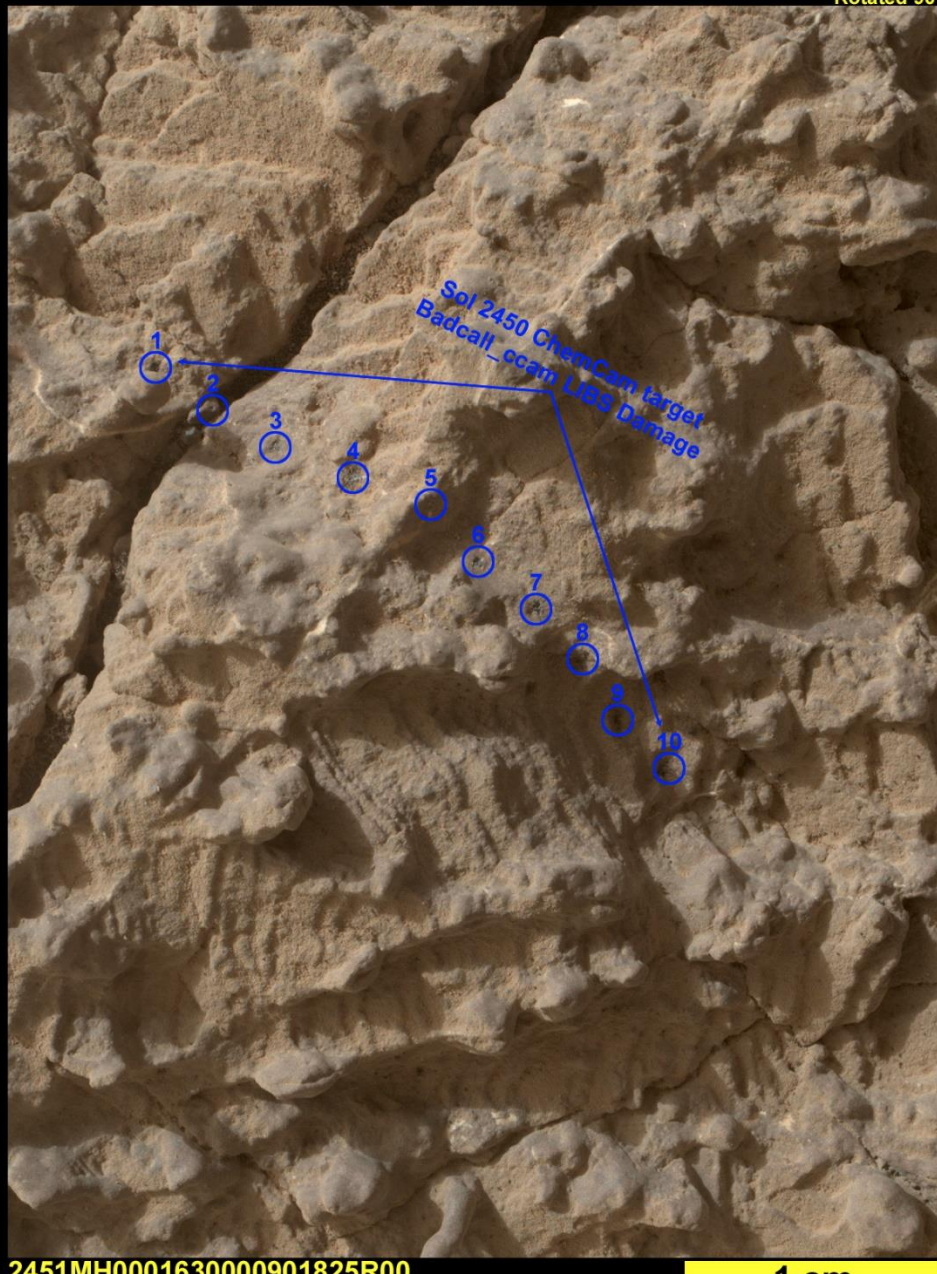


Figure S3: The Badcall ChemCam target MAHLI observation (sol 2451) from ~5 cm standoff with LIBS pits annotated (2451MH0001630000901825R00).

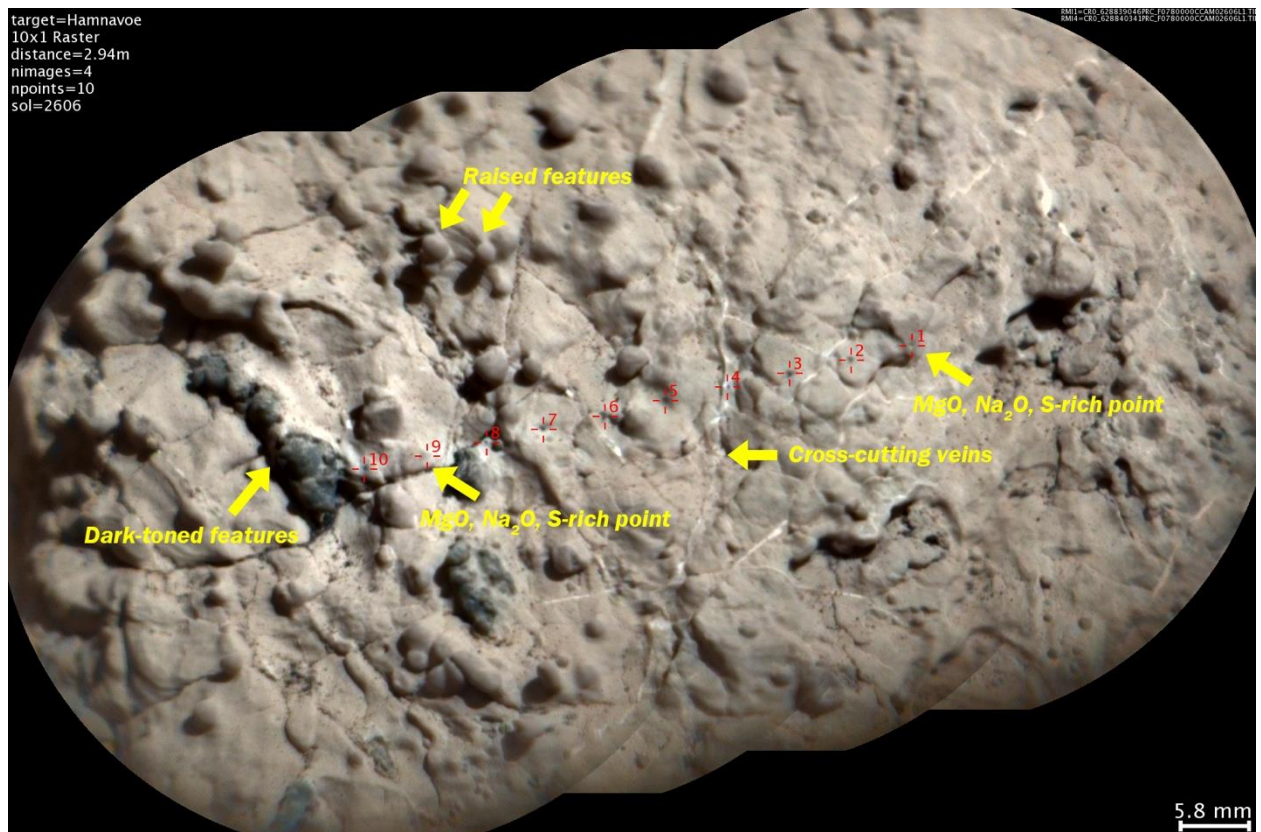


Figure S4: The Hamnavoe ChemCam target RMI (sol 2606) colorized with Mastcam image 2606MR0136860011102041Coo.

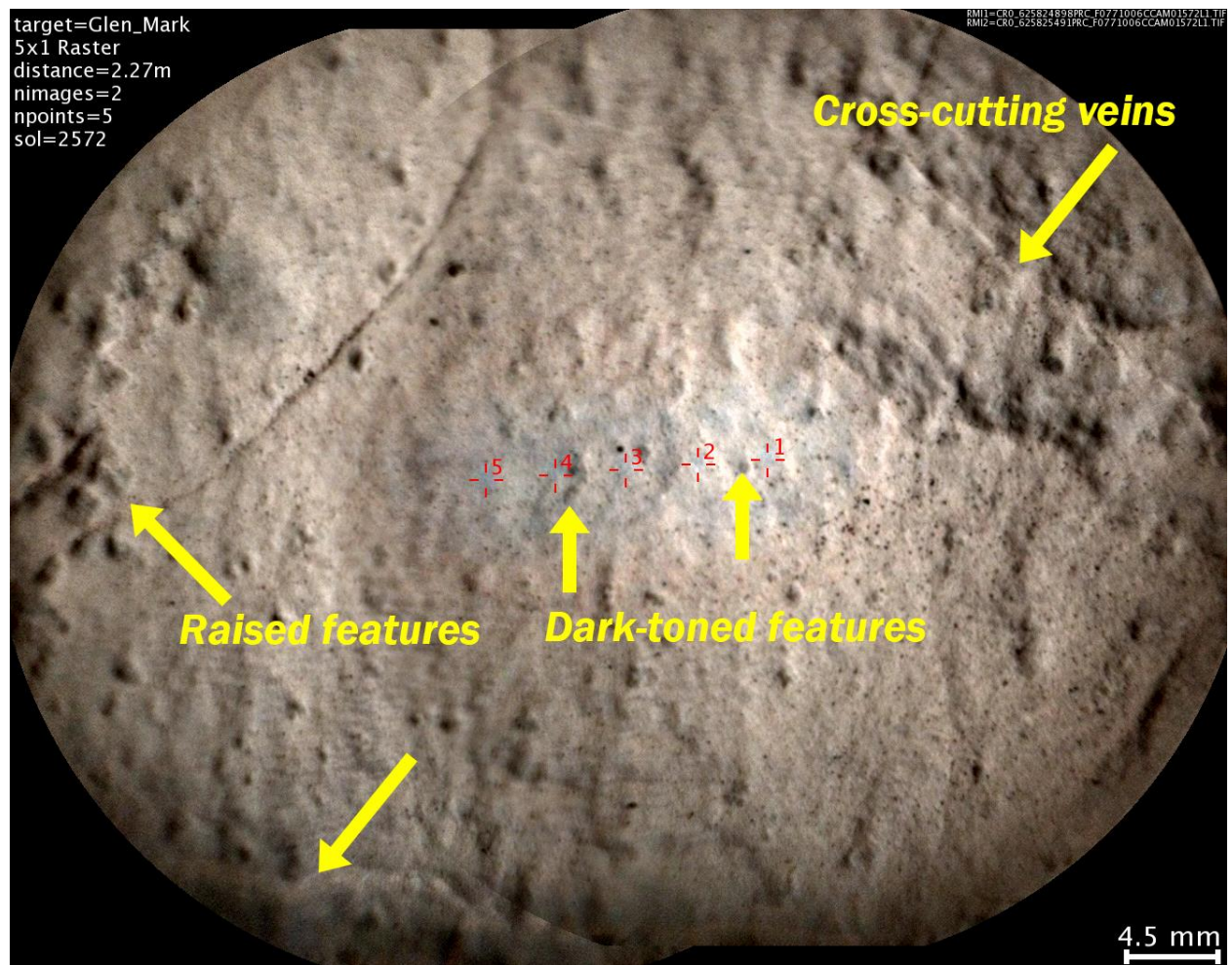


Figure S5: The Glen\_Mark ChemCam target RMI (sol 2572) colorized with Mastcam image 2572MR0135040001100180Coo.

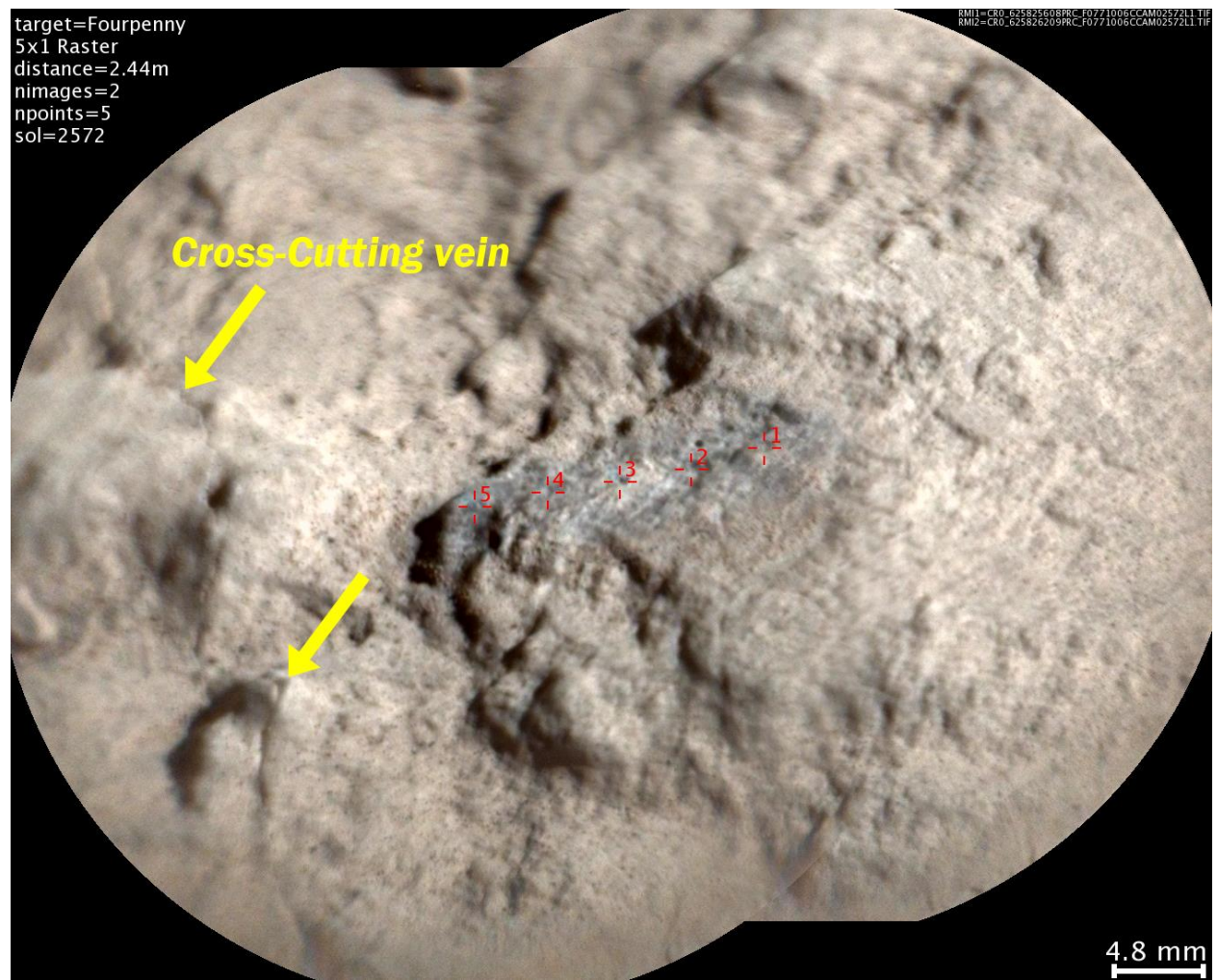


Figure S6: The Fourpenny ChemCam target RMI (sol 2572) colorized with Mastcam image 2572MR0135050001100181Coo.

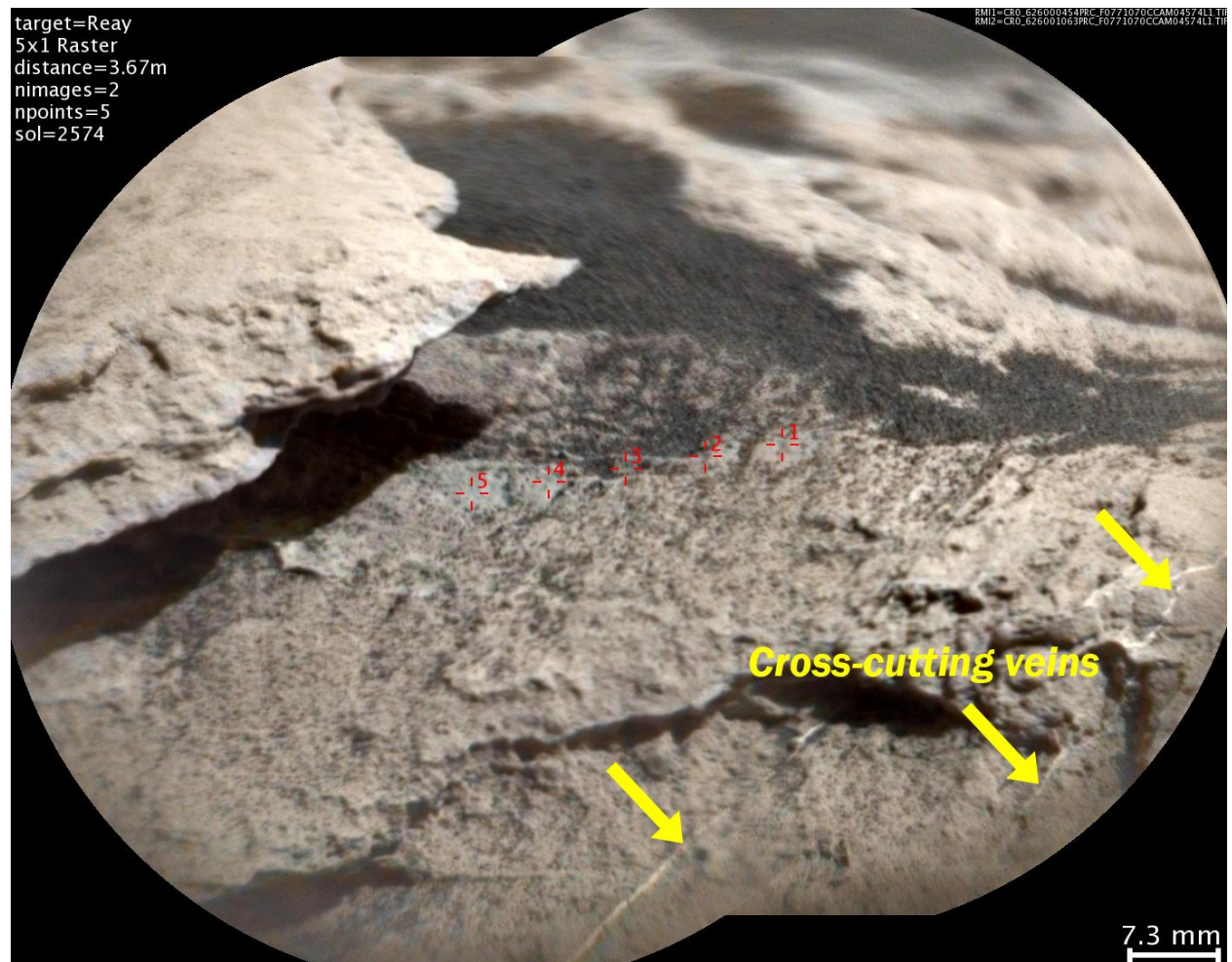


Figure S7: The Reay ChemCam target RMI (sol 2574) colorized with Mastcam image 2575MR0135280011100325Coo.

**Sol 2581 – Target Conachair – After DRT**  
**Focus merge product from ~1 cm standoff**

Rotated 90°

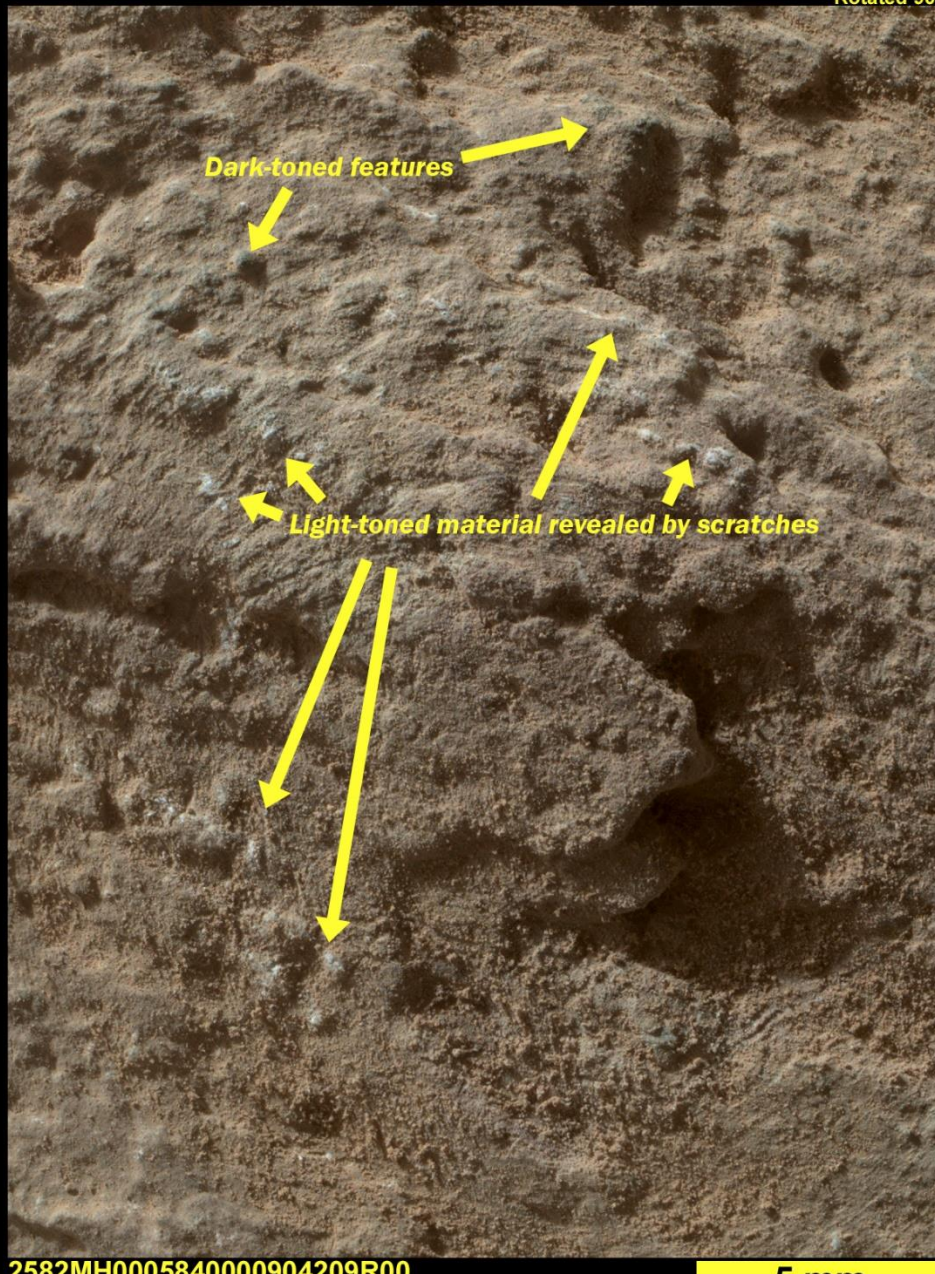
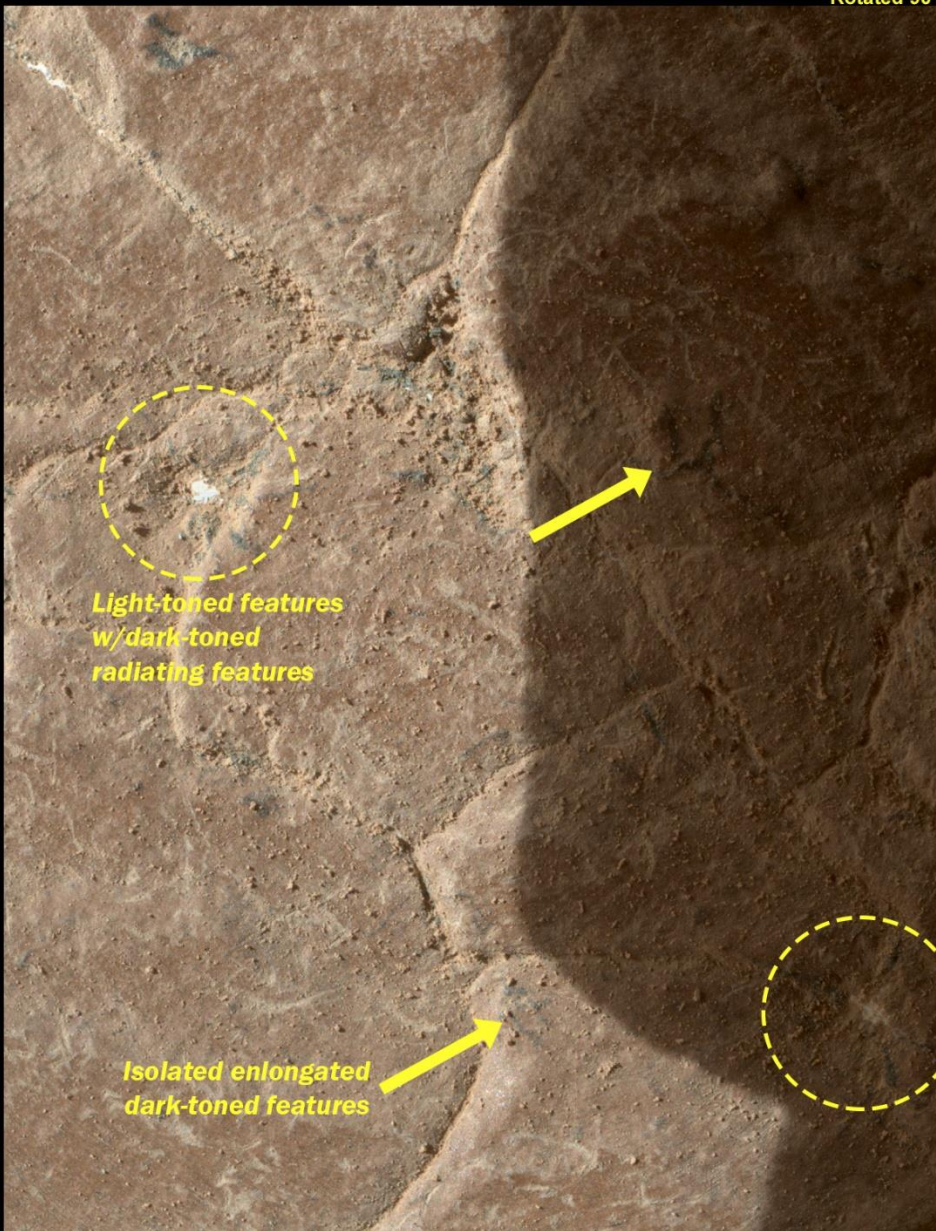


Figure S8: The Conachair MAHLI target (sol 2582) from ~1 cm standoff (2581MH0005840000904209R00). There is no ChemCam target associated with this observation.

**Sol 2597 – Target Everbay – After DRT**  
**Focus merge product from ~ 1 cm standoff**

Rotated 90°



2597MH0001930001000105R00

5 mm

Figure S9: The Everbay MAHLI target (sol 2597) from ~1 cm standoff (2597MH0001930001000105R00). There is a ChemCam target associated with this observation (Everbay\_ccam, sol 2598), but the ChemCam target is not visible in the MAHLI image.

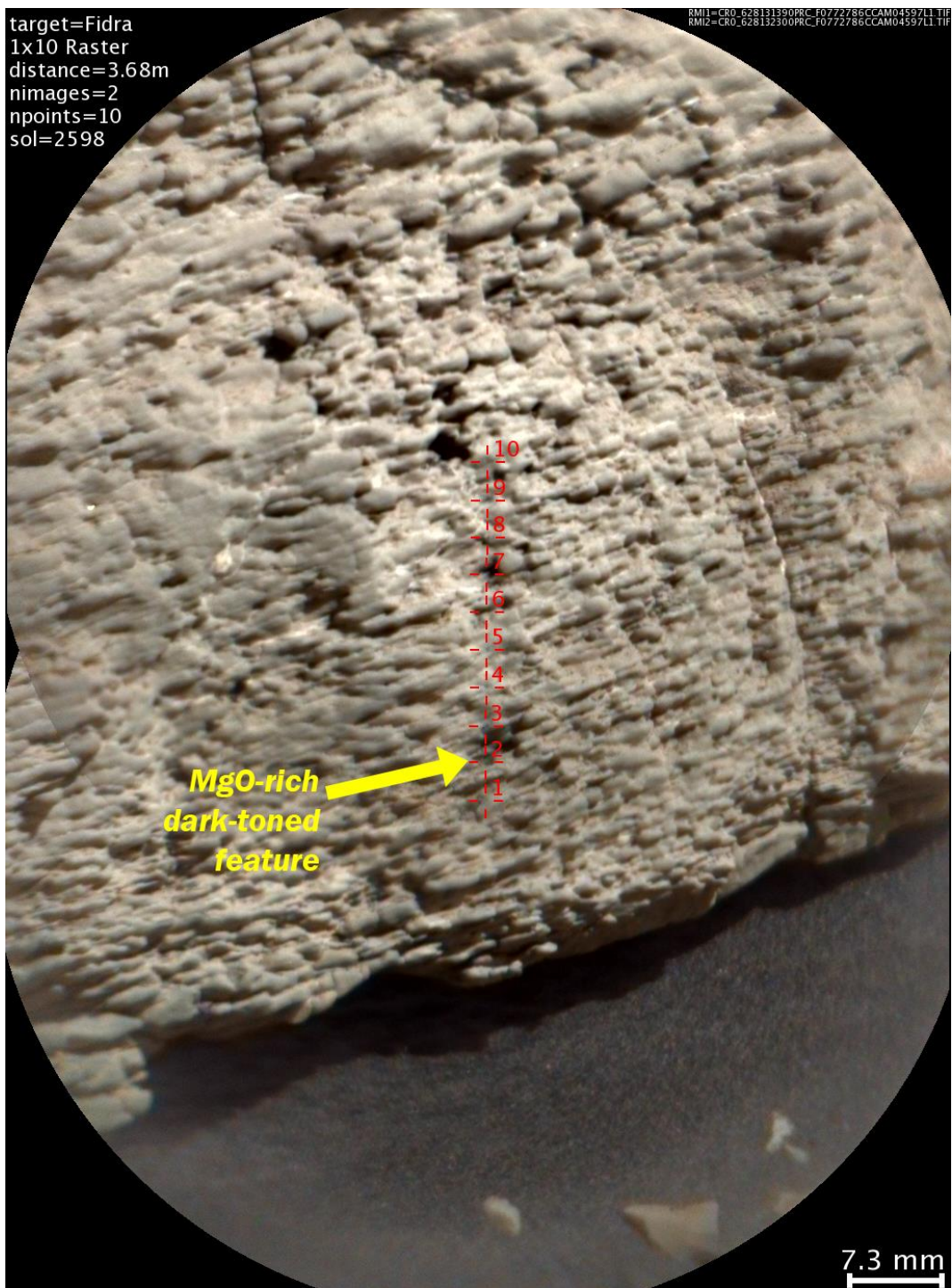


Figure S10: The Fidra ChemCam target RMI (sol 2598) colorized with Mastcam image 2598MR0136580001101072Coo.



Figure S11: The Balgy ChemCam target RMI (sol 2645) colorized with Mastcam image 2645MR0138510001103560Coo.

**Sol 2749 – Target Glasgow\_1 – Before DRT**  
**Image acquired from ~ 5 cm standoff**

Rotated 270°

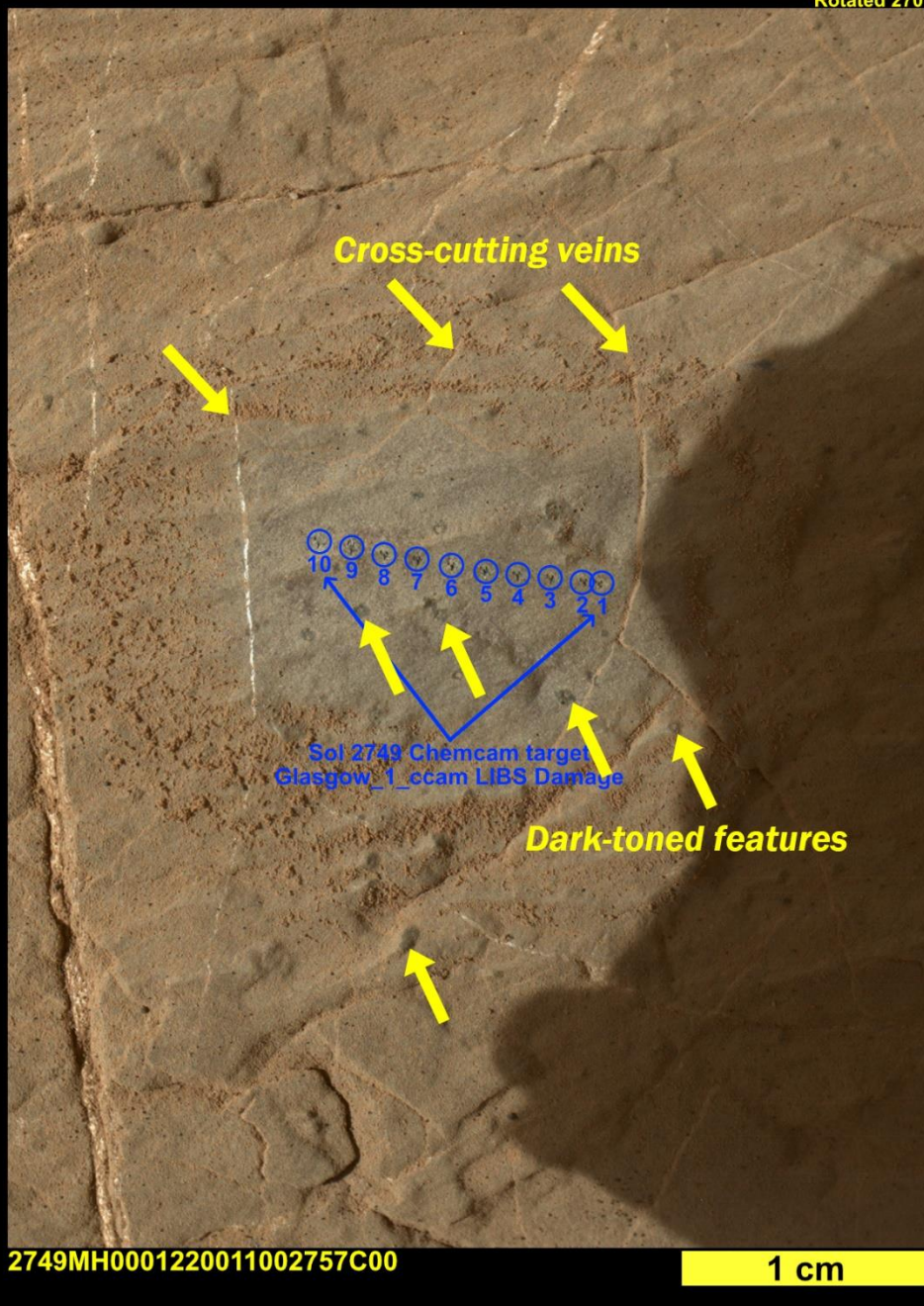


Figure S12: The Glasgow DRT (pre-drill) MAHLI target (sol 2749) from ~5 cm standoff with LIBS pits annotated (2749MH0001220011002757C00).

Sol 2747 – Target Troon

**Focus merge product from ~ 5 cm standoff**

Rotated 270°

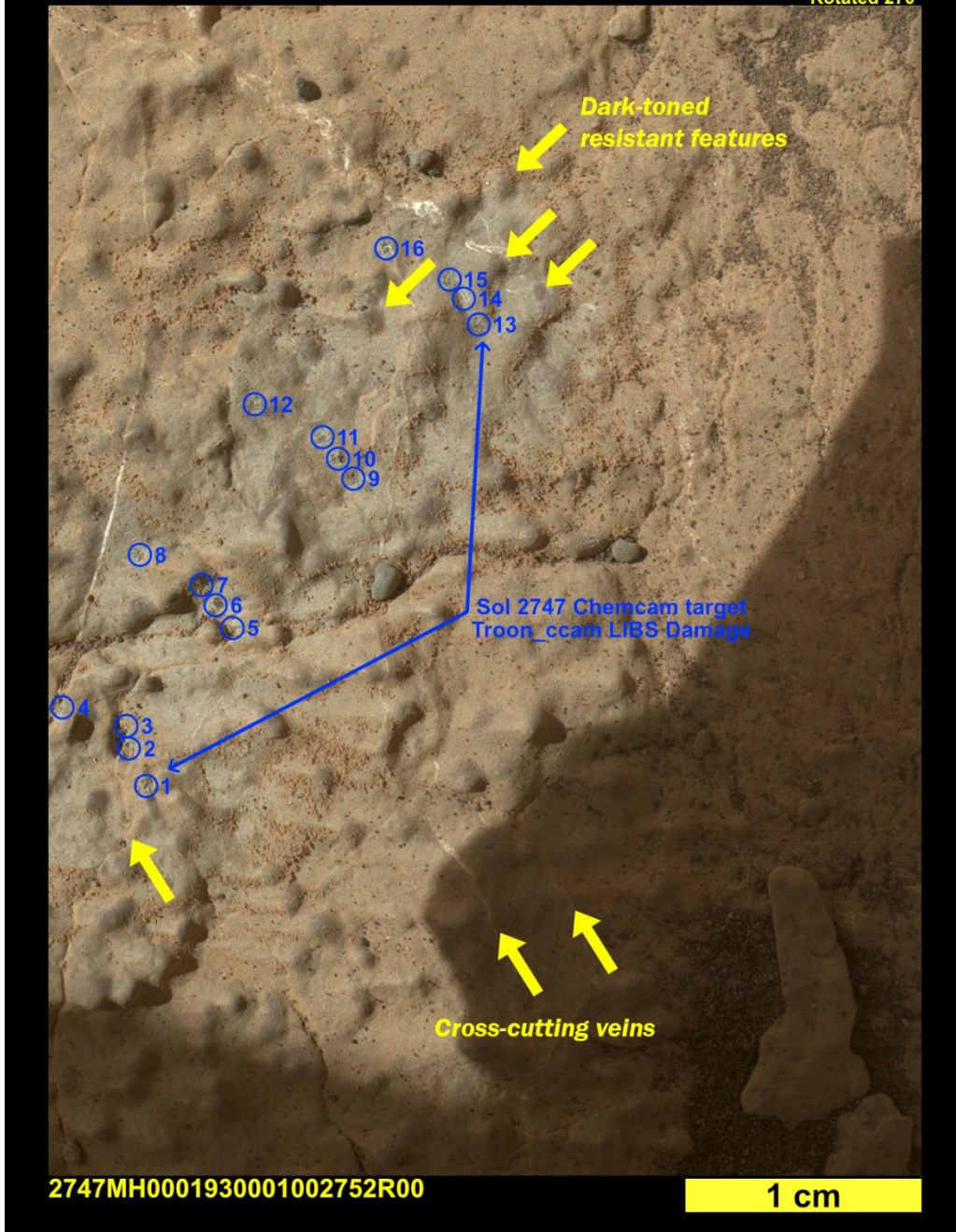


Figure S13: The Troon MAHLI target (sol 2747) from ~5 cm standoff with LIBS pits annotated (2747MH0001930001002752R00).



Figure S14: The Large\_Island ChemCam target RMI (sol 2750) colorized with Mastcam image 2750MR014200001201255Coo.

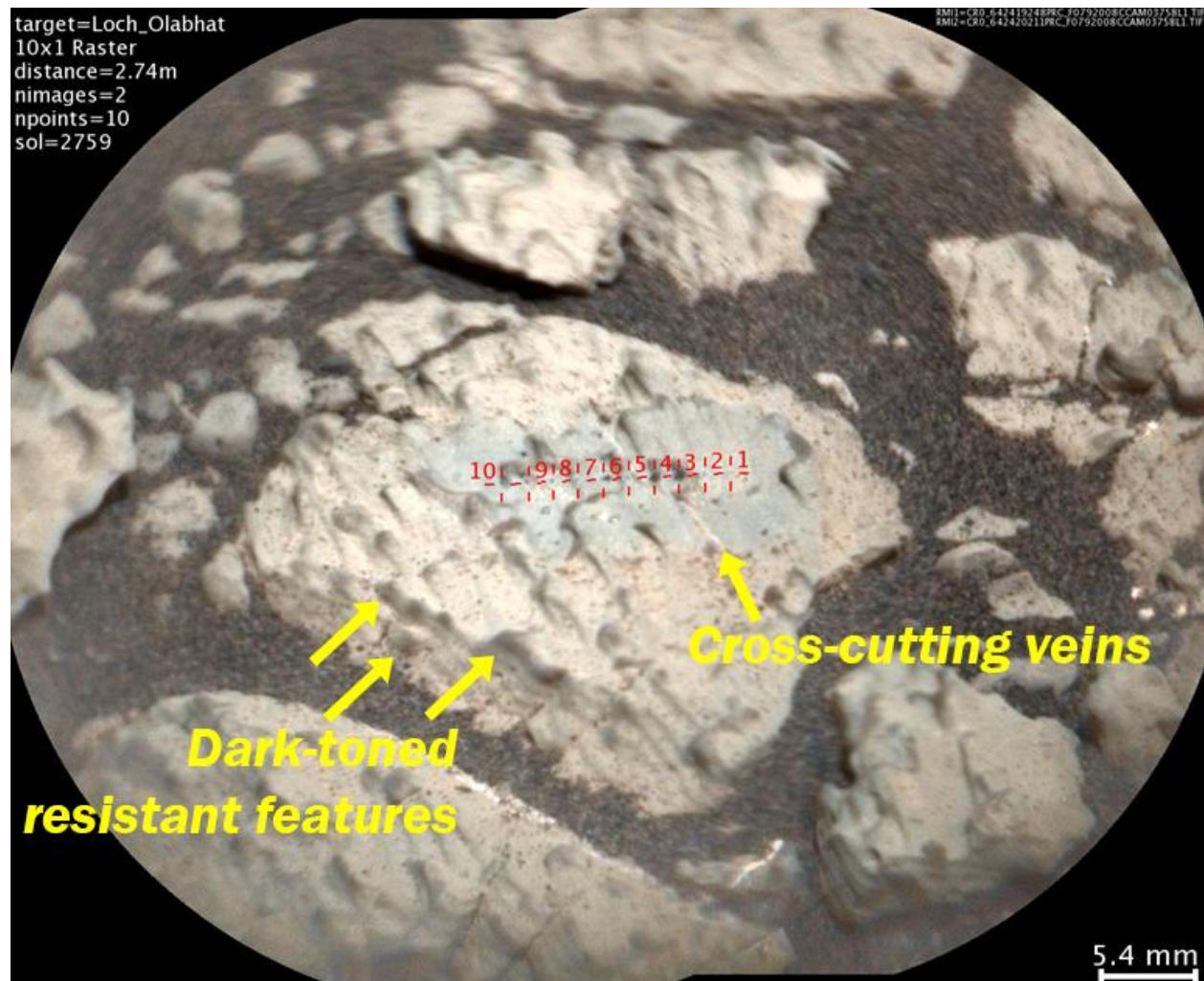


Figure S15: The Loch\_Olabhat ChemCam target RMI (sol 2759) colorized with Mastcam image 2759MR0144660001201676Coo.



Figure S16: The Bearsden ChemCam target RMI (sol 2735) colorized with Mastcam image 2735MR0143310051200645C00. Exposure in this figure is affected overexposure on the large patch of vein material.

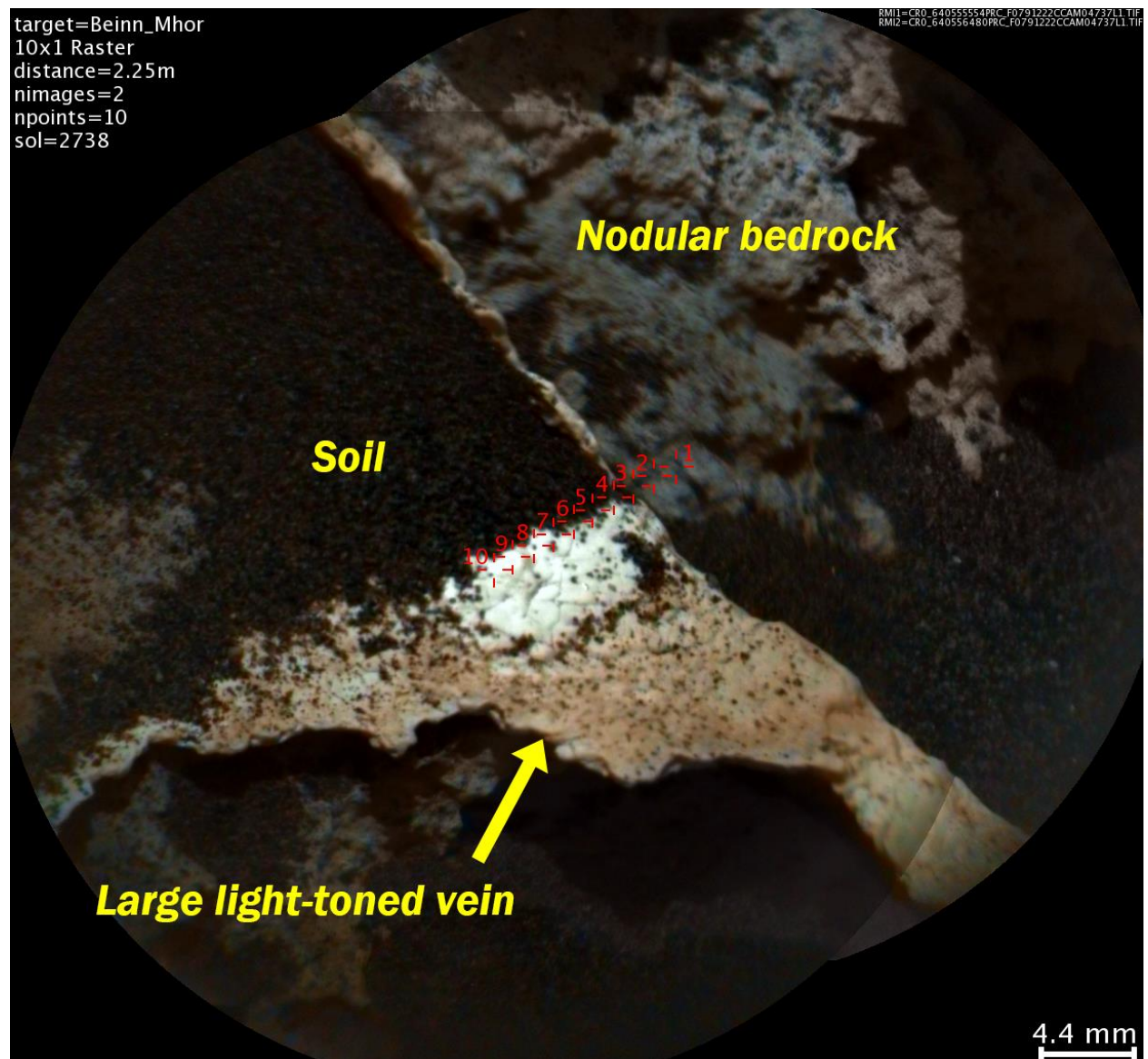


Figure S17: The Beinn\_Mohr ChemCam target RMI (sol 2738) colorized with Mastcam image 2738MR0143560001200767Coo. Exposure in this figure is affected by overexposure on the large patch of vein material.

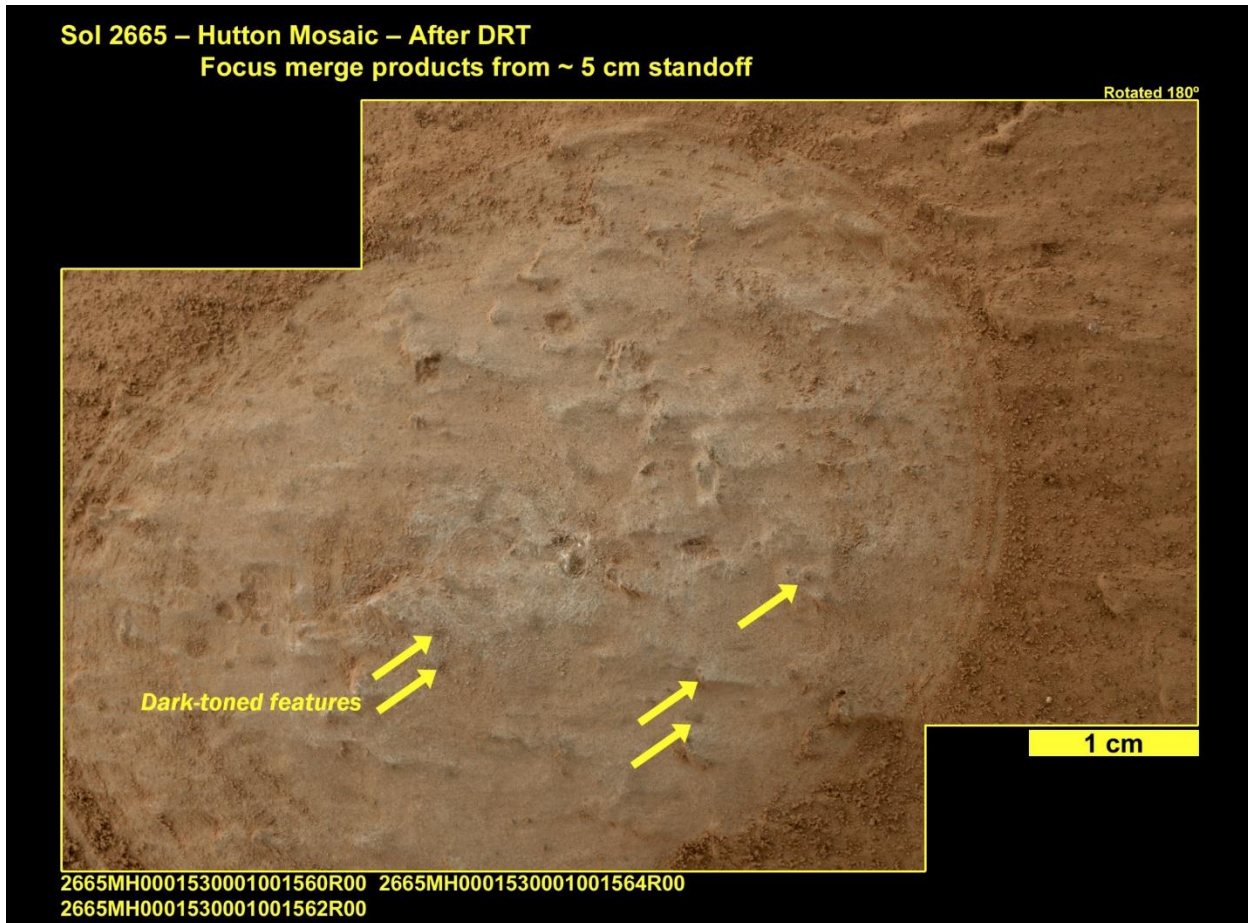


Figure S18: The Hutton DRT (pre-drill) MAHLI target (sol 2665) from ~5 cm standoff (2665MH0001530001001560R00; 2665MH0001530001001562R00; 2665MH0001530001001564R00). This MAHLI mosaics was recorded before the Hutton\_ccam target was performed on sol 2666.

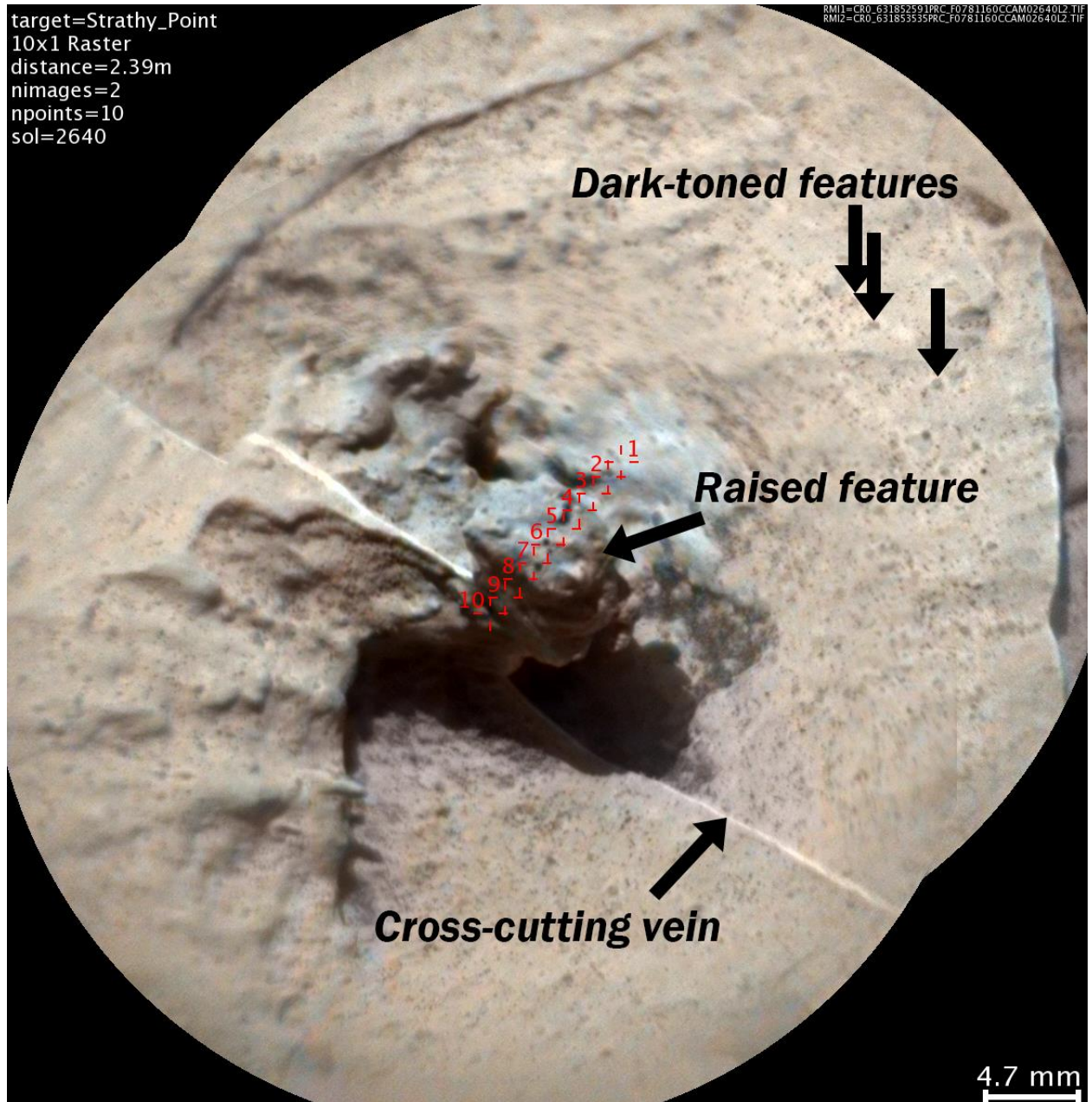


Figure S19: The Strathy\_Point ChemCam target RMI (sol 2640) colorized with Mastcam image 2642MR0138340011103411C00.

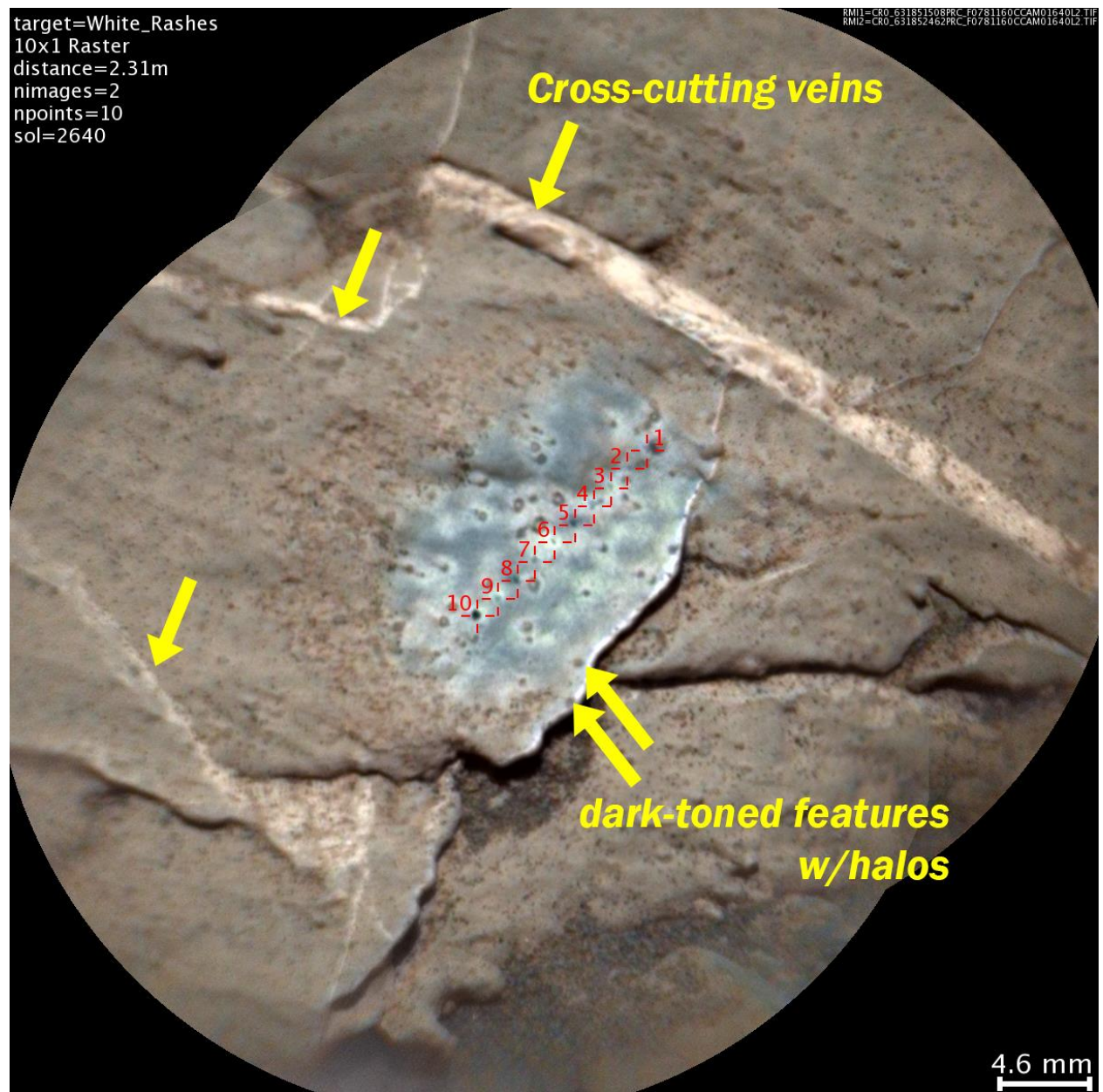


Figure S20: The White\_Rashes ChemCam target RMI (sol 2640) colorized with Mastcam image z642MR0138330011103409C00.

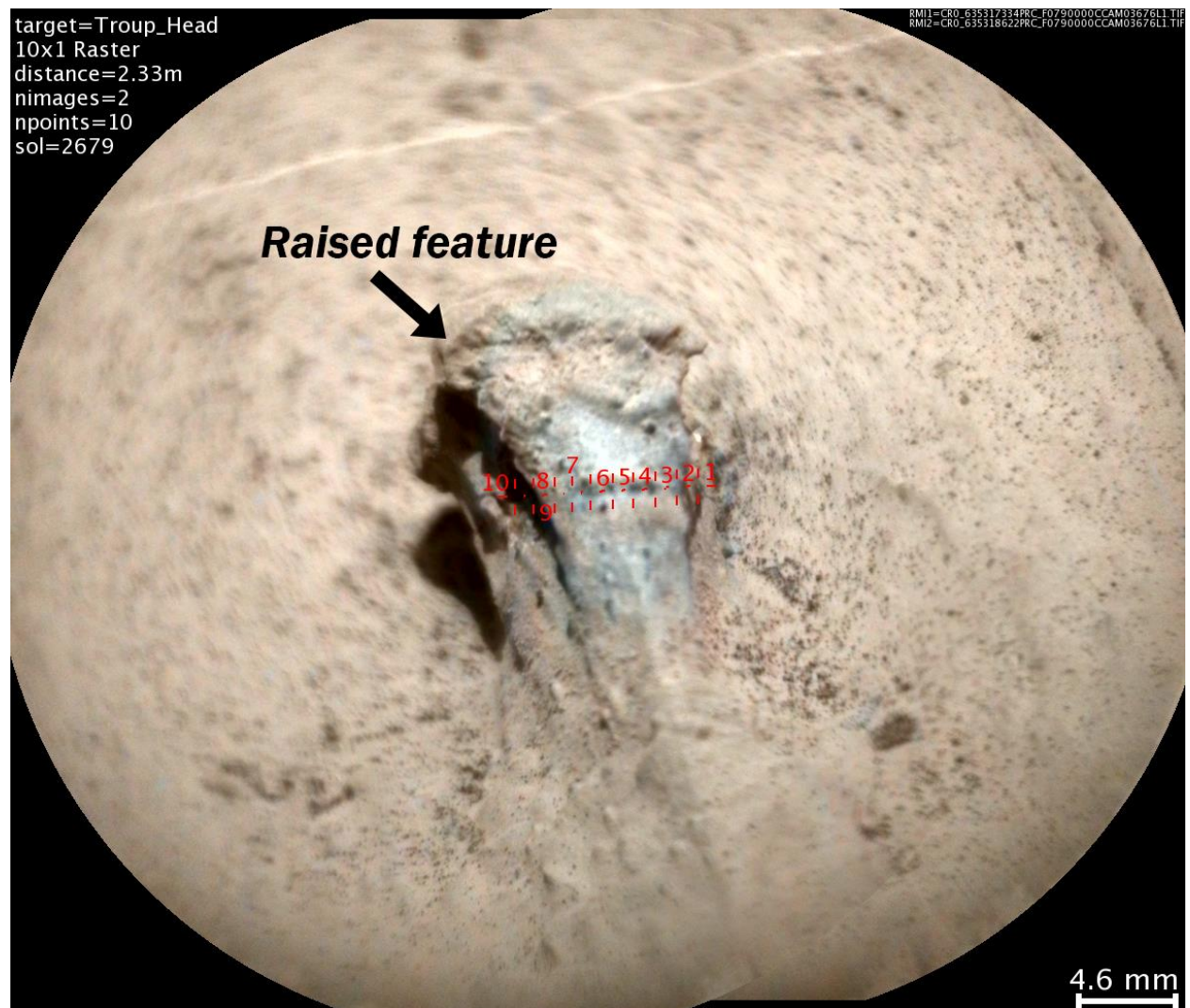


Figure S21: The Troup\_Head ChemCam target RMI (sol 2679) colorized with Mastcam image 2679MR0140260000604591Coo.



Figure S22: The Abernethy\_ccam ChemCam target RMI (sol 2642) colorized with Mastcam image 2642MR0138320051103400C00.

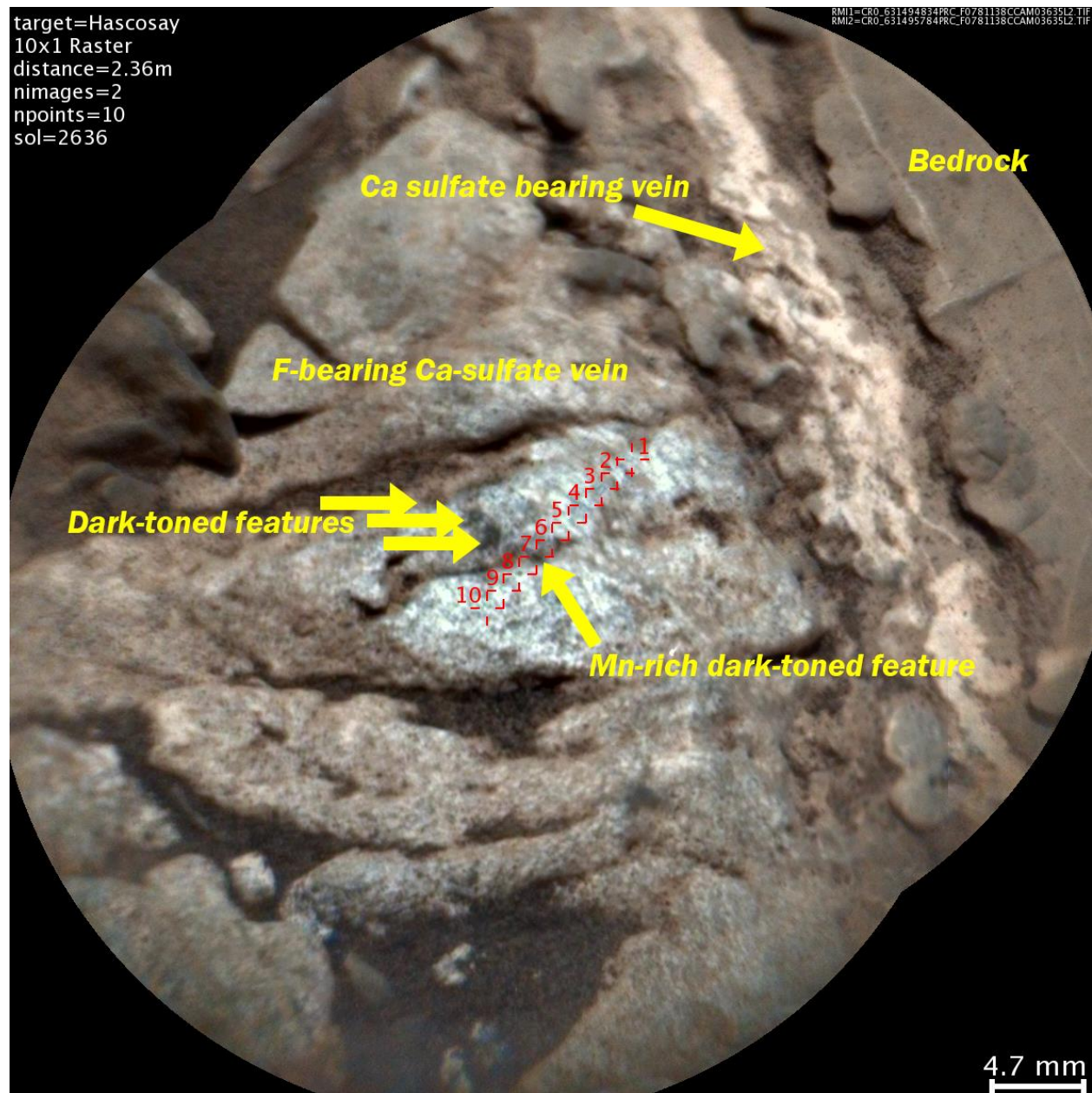


Figure S23: The Hascosay ChemCam target RMI (sol 2636) colorized with Mastcam image 2636MR013806001103108C00.

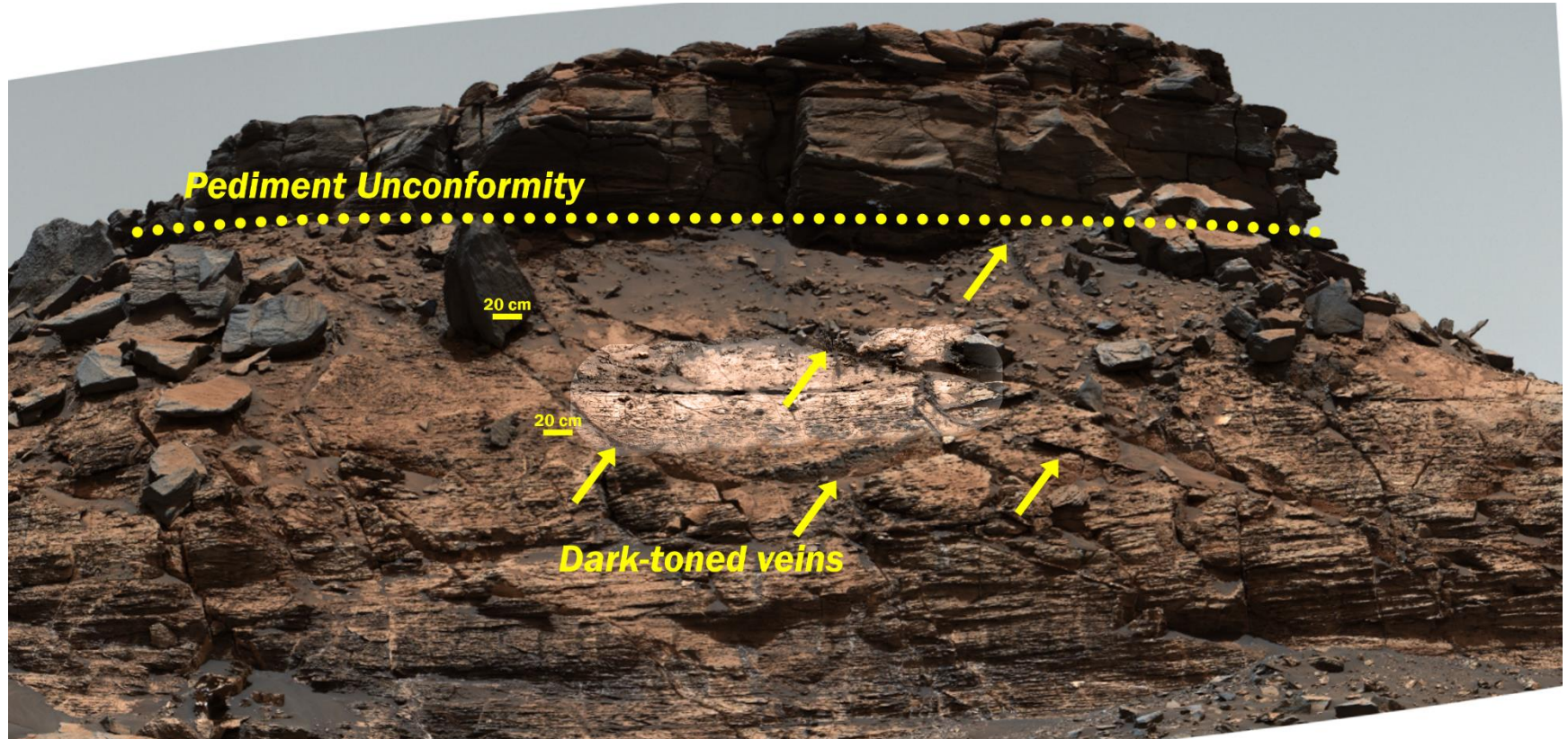


Figure S24: The Haymarket ChemCam target long distance RMI (sol 2772) overlaid on part of the Mastcam mosaic image of Tower Butte from the Glasgow Drill sample site on sol 2751 (2751MR0144230001201257C00; 2751MR0144230011201258C00; 2751MR0144230021201259C00; 2751MR0144230031201260C00; 2751MR0144230041201261C00; 2751MR0144230051201262C00; 2751MR0144230061201263C00; 2751MR0144230071201264C00; 2751MR0144230081201265C00; 2751MR0144230091201266C00; 2751MR0144230101201267C00; 2751MR0144230111201268C00; 2751MR0144230121201269C00; 2751MR0144230131201270C00; 2751MR0144230141201271C00; 2751MR0144230151201272C00; 2751MR0144230161201273C00; 2751MR0144230171201274C00; 2751MR0144230181201275C00; 2751MR0144230191201276C00; 2751MR0144230201201277C00; 2751MR0144230211201278C00; 2751MR0144230221201279C00; 2751MR0144230231201280C00; 2751MR0144230241201281C00; 2751MR0144230251201282C00; 2751MR0144230261201283C00; 2751MR0144230271201284C00; 2751MR0144230281201285C00; 2751MR0144230291201286C00; 2751MR0144230301201287C00; 2751MR0144230311201288C00; 2751MR0144230321201289C00; 2751MR0144230331201290C00; 2751MR0144230341201291C00;

2751MR0144230351201292C00; 2751MR0144230361201293C00; 2751MR0144230371201294C00; 2751MR0144230381201295C00;  
2751MR0144230391201296C00; 2751MR0144230401201297C01; 2751MR0144230411201298C00; 2751MR0144230421201299C00;  
2751MR0144230431201300C00; 2751MR0144230441201301C00; 2751MR0144230451201302C00; 2751MR0144230461201303C00;  
2751MR0144230471201304C00; 2751MR0144230481201305C00; 2751MR0144230491201306C00; 2751MR0144230501201307C00;  
2751MR0144230511201308C00; 2751MR0144230521201309C00; 2751MR0144230531201310C00; 2751MR0144230541201311C00;  
2751MR0144230551201312C00; 2751MR0144230561201313C00).

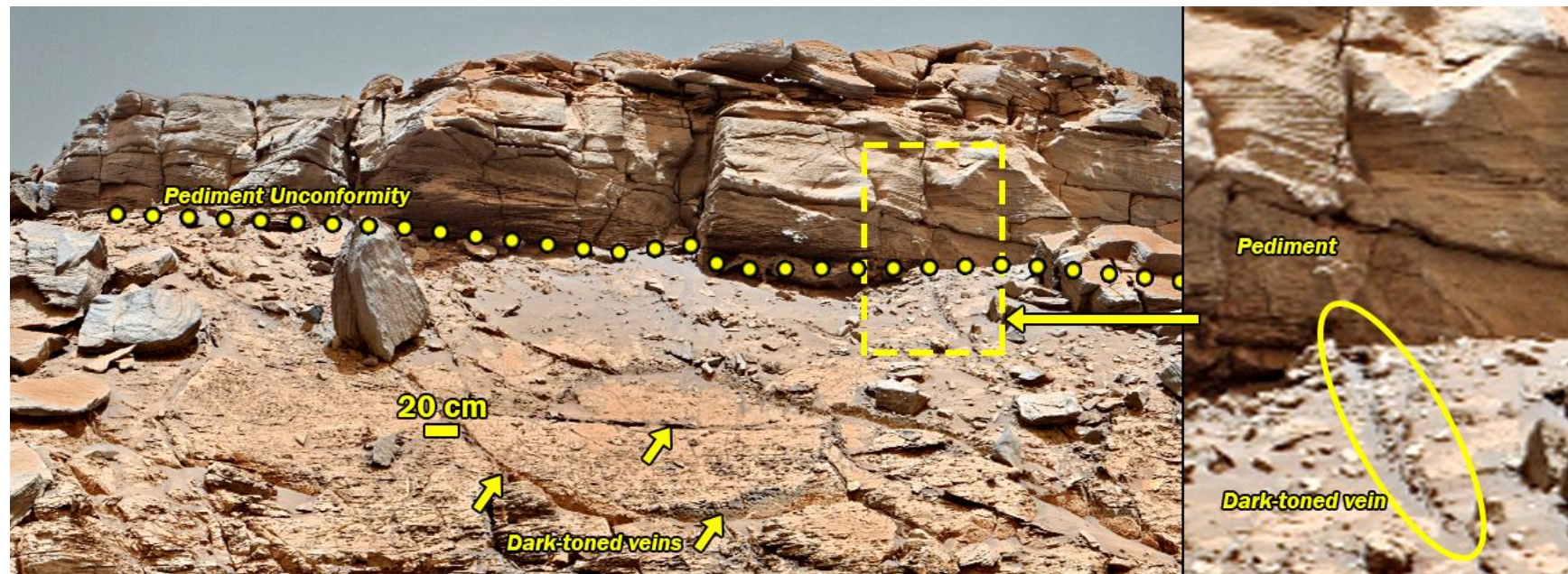


Figure S25: Brightened and annotated version of Figure S24 to better analyze the shadowed regions beneath the pediment unconformity where a dark-toned vein appears truncated by the Pediment unconformity (inset).

**Sol 2826 – Target Breamish – After DRT**  
**Focus merge product from ~ 2 cm standoff**

Rotated 180°

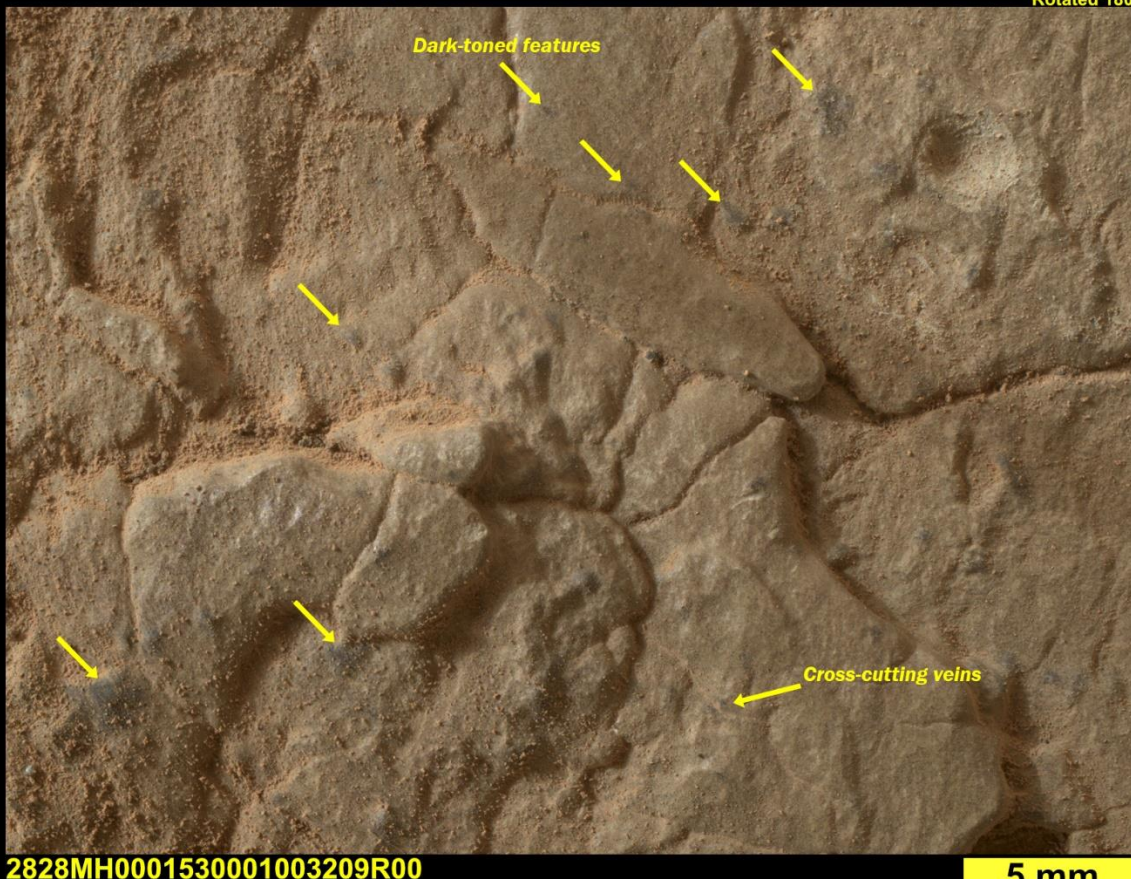


Figure S26: The Breamish MAHLI target (sol 2826) from ~2 cm standoff (2828MH0001530001003209R00). This MAHLI image was recorded before the Breamish\_ccam target was performed on sol 2828.



Figure S27: The Smugglers\_Cave ChemCam target RMI (sol 2936) colorized with Mastcam image 2936MR0153140001301117Coo.

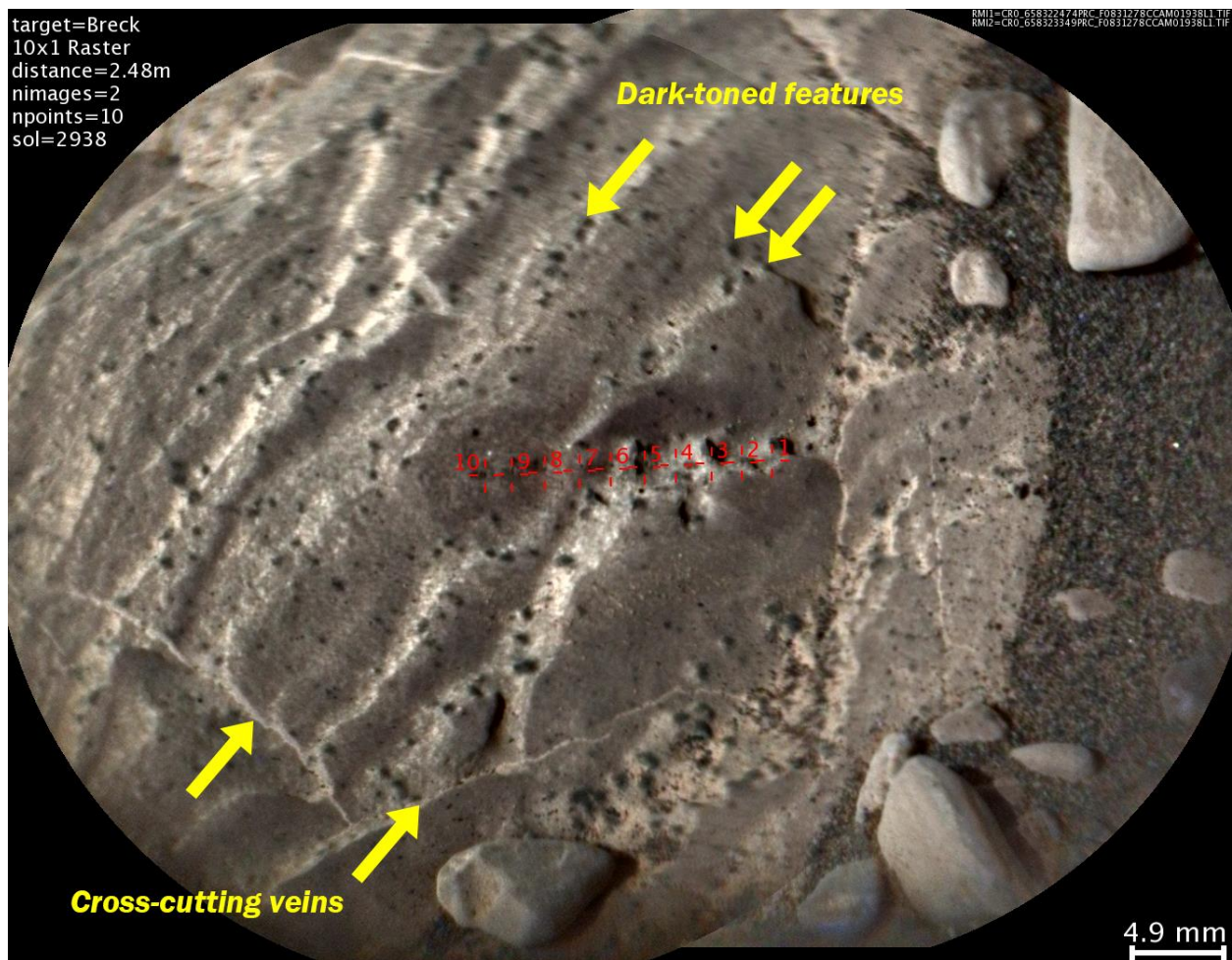


Figure S28: The Breck ChemCam target RMI (sol 2938) colorized with Mastcam image 2938MR0153310001301346Coo.

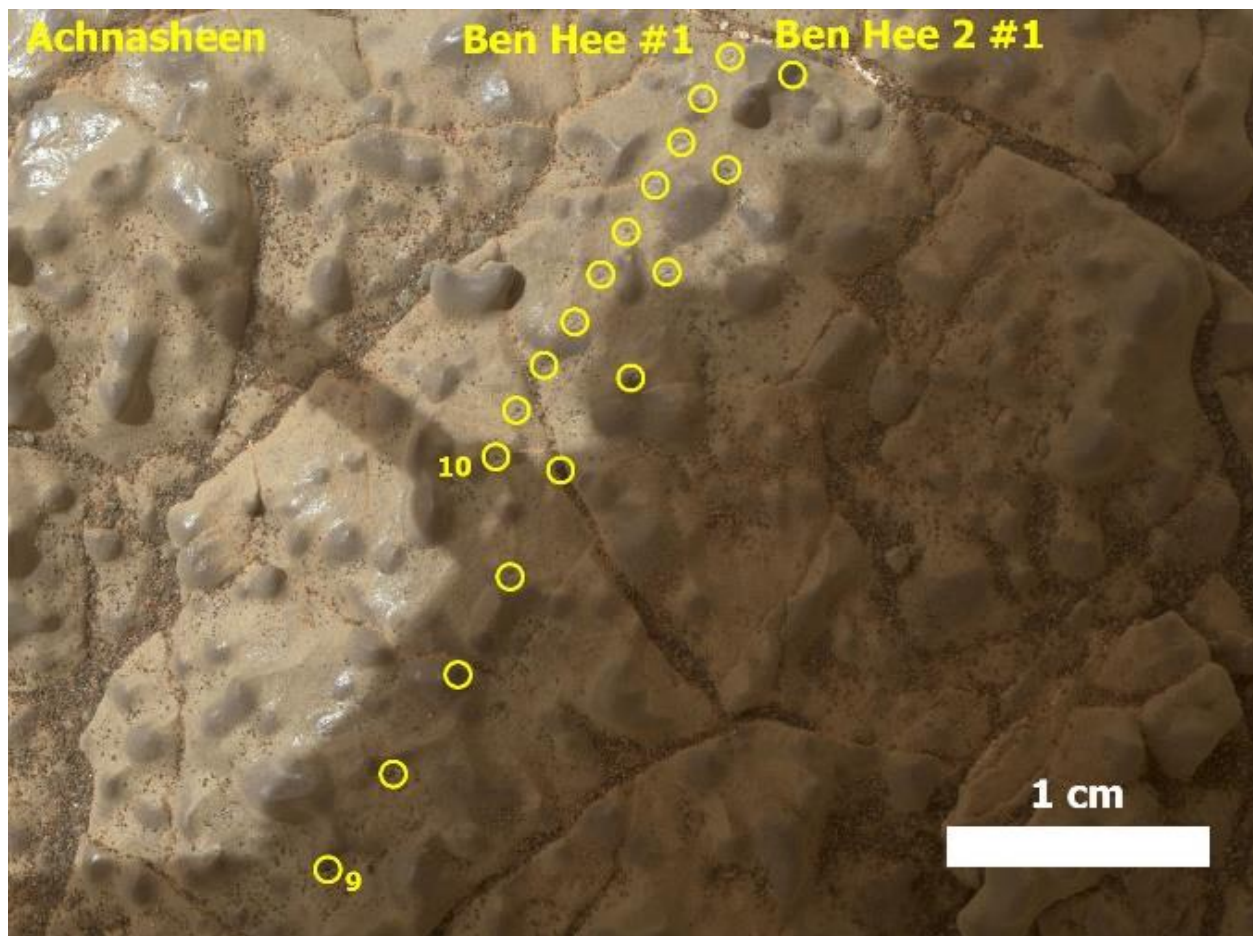


Figure S29: The Ben\_Hee and Ben\_Hee\_2 ChemCam targets (sol 2960 and 2962) annotated on the Achnasheen MAHLI target from ~5 cm standoff (2965MH0002650001004439Roo).

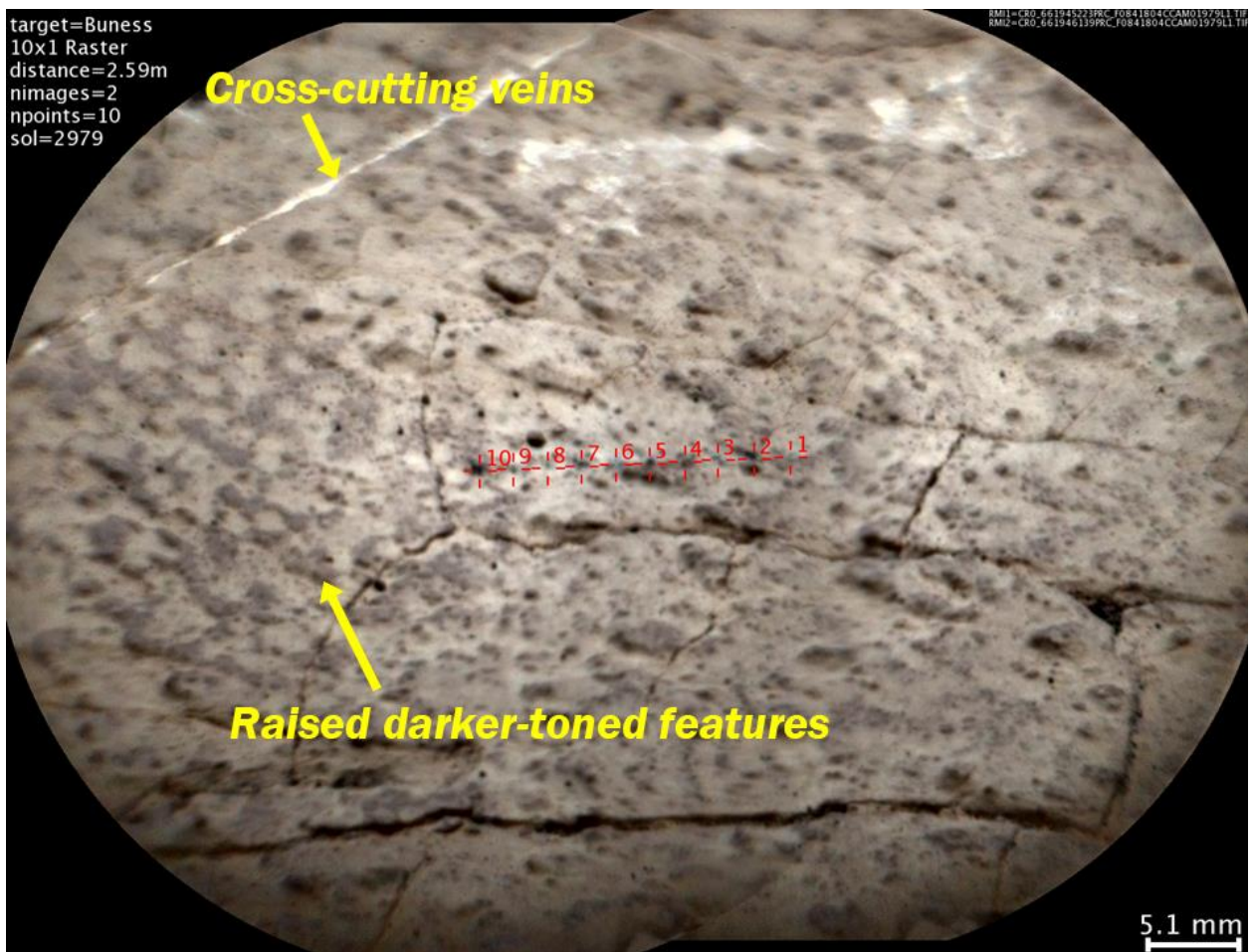


Figure S30: The Buness ChemCam target RMI (sol 2979) colorized with Mastcam image 2979MR0155570001303102Coo.

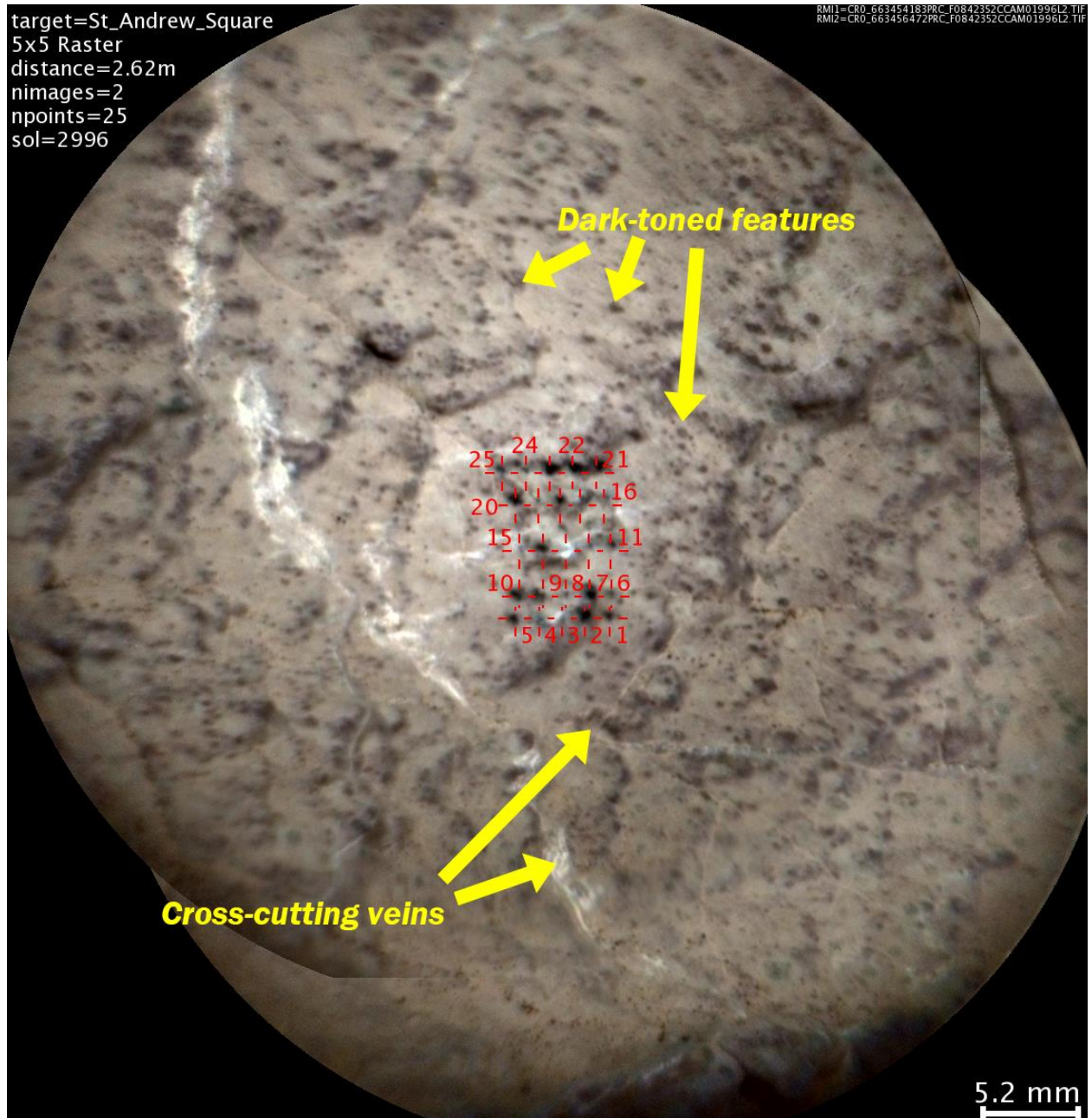


Figure S31: The St\_Andrew\_Square ChemCam target RMI (sol 2996) colorized with Mastcam image 2997MR0156280151303365Coo.

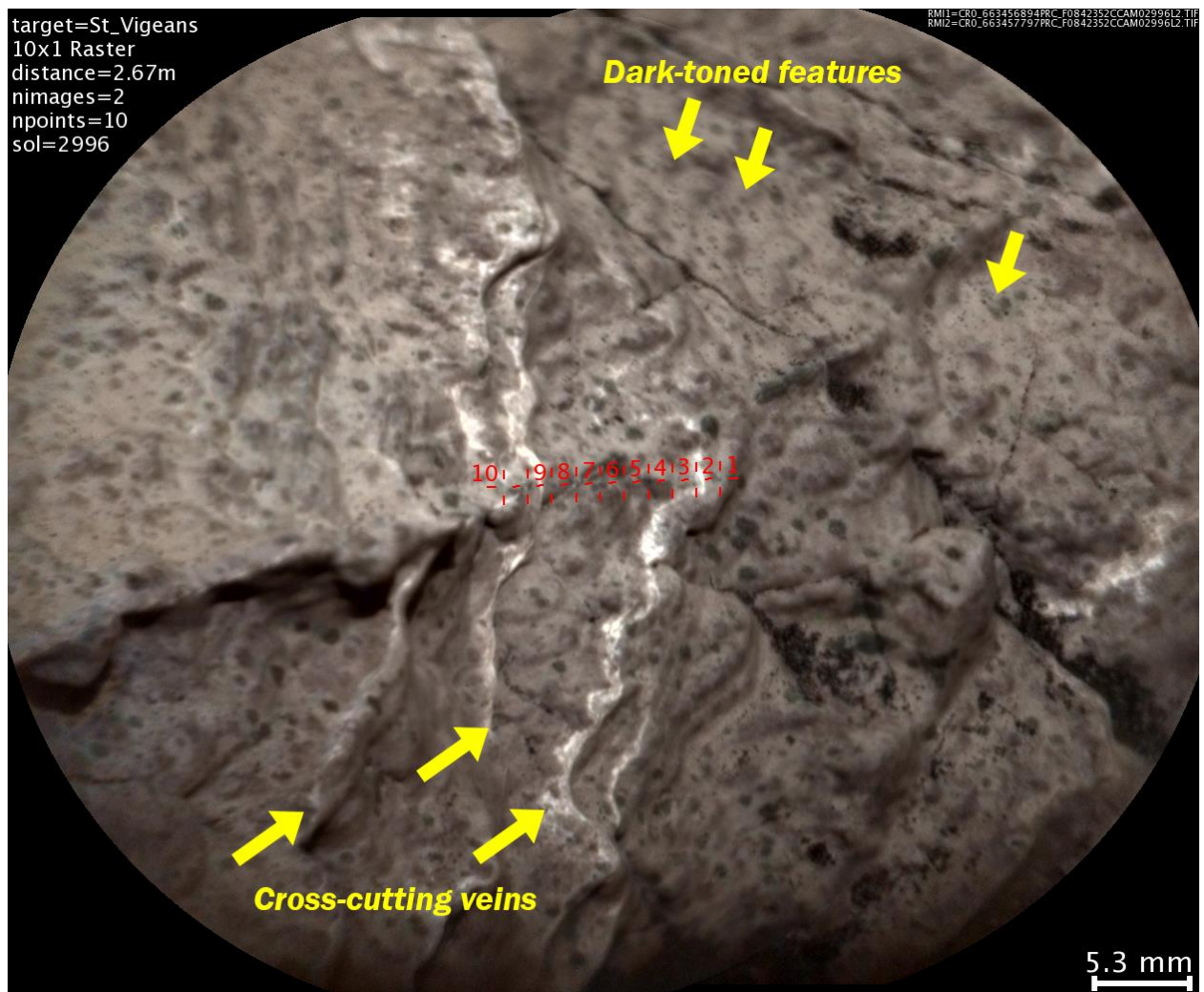


Figure S32: The St\_Vigeans ChemCam target RMI (sol 2996) colorized with Mastcam image 2997MR0156280151303365Coo.

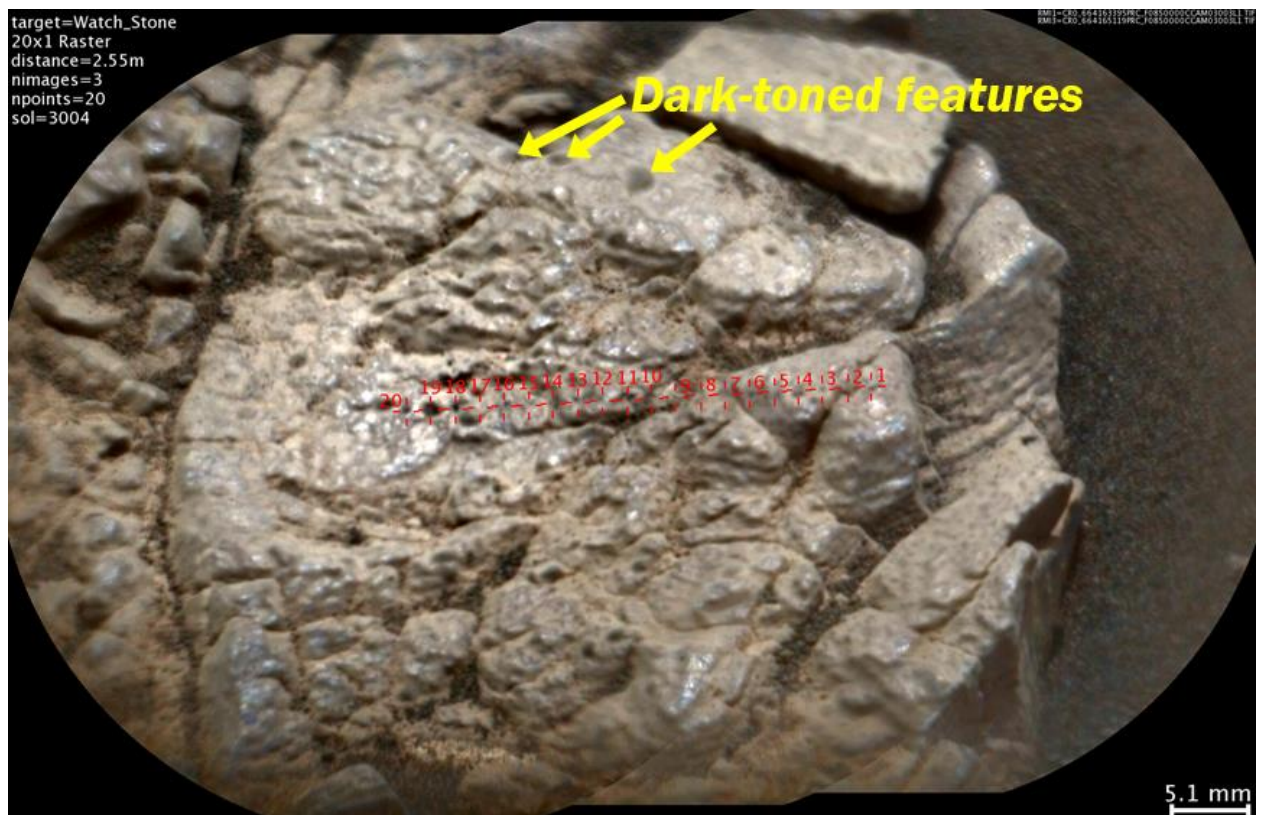


Figure S33: The Watch\_Stone ChemCam target RMI (sol 3004) colorized with Mastcam image 3004MR0156600001303567Coo.

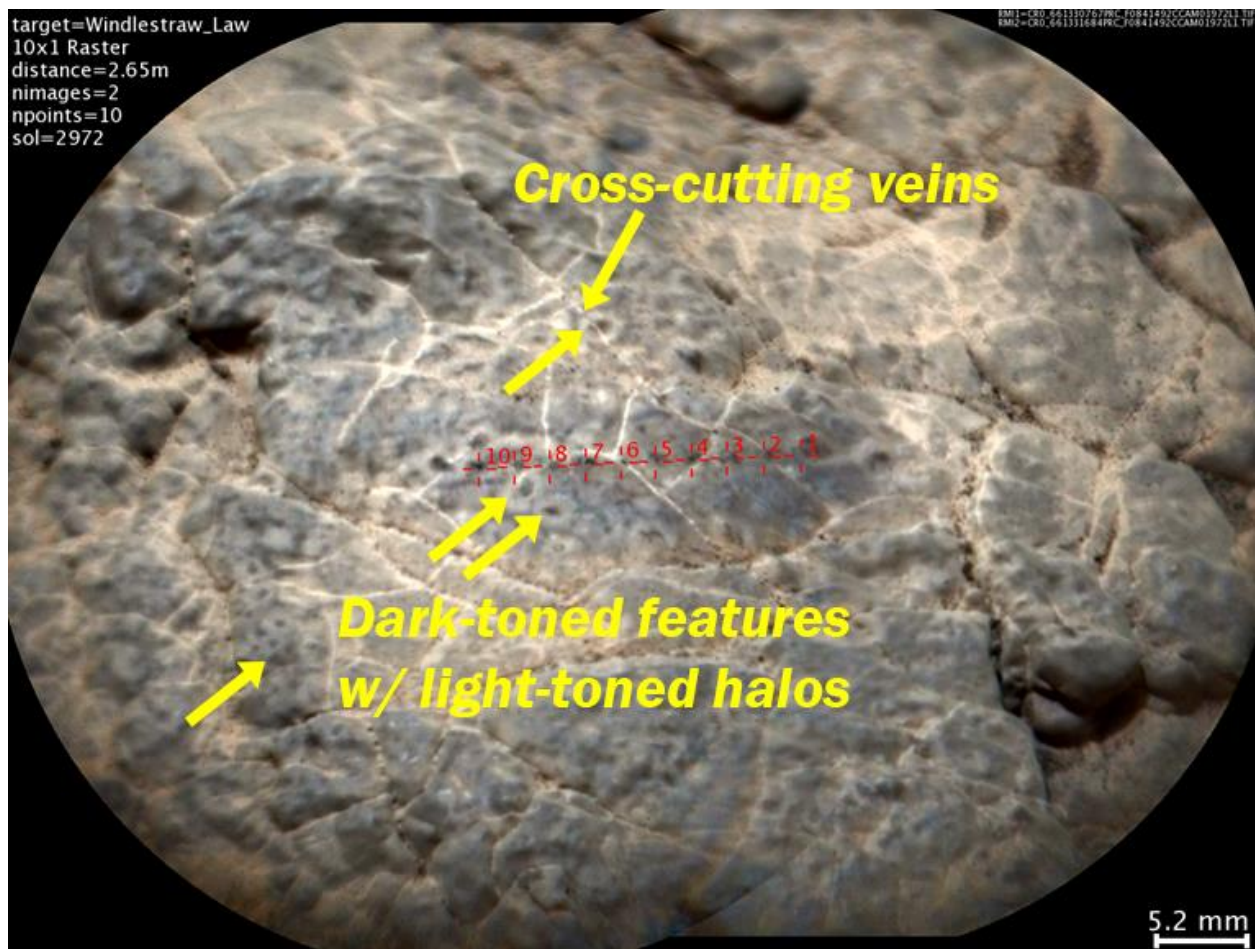


Figure S34: The Windlestraw\_Law ChemCam target RMI (sol 2972) colorized with Mastcam image 2972MR0155160061302928C00.



Figure S35: The Tomb\_of\_the\_Eagles ChemCam target RMI (sol 3003) colorized with Mastcam image 3003MR0156530001303507Coo.

### **Text S3. Ternary Diagrams Separated by Chemical Endmember**

In the main manuscript Fig 8, we plot all of the chemical endmembers and diagenetic categories on the same set of MgO-CaO- $\text{FeO}_T$  and MgO-MnO- $\text{FeO}_T$  ternary plots. For clarity, we also made interactive \*.html versions of these plots available for this supplement. These plots allow you to hover with your mouse over an individual observation point to see more information about it, and include zoom and pan features for the diagrams.

In addition, we have included here ternary diagrams that only plot the diagenetic features in each of the separate chemical endmembers, along with the median bedrock composition and the interquartile range of that median bedrock composition (see Table S1). These diagrams help illustrate the trends, if any, in diagenetic data in individual chemical endmembers. Figures S36–S40 show the ternary diagrams for coherent, rubbly, Glasgow, Hutton, and Groken/Mary Anning, respectively. These ternary diagrams plot diagenetic feature observation points based on their strongest enrichment compared to the bedrock composition.

Figures S36 and S37 show the ternary plots for the coherent and rubbly endmembers. These two endmembers are generally from the Jura and Knockfarril Hill stratigraphic members, but do not include the Groken/Mary Anning drill area that is part of KfH. These stratigraphic members generally did not have many small-scale diagenetic features, besides the Ca-sulfate veins, and a limited number of nodular targets at e.g., Harlaw Rise, the lower sections of the buttes, and the Benches (see manuscript). Hence, these two plots have a small number of data points. Nevertheless, these plots still show the strong Ca-sulfate mixing trends, and relationships between  $\text{FeO}_T$ , MgO, and MnO. For Coherent targets (Figure S36), besides a single high-MnO nodule point, the composition of the nodules (green points) tends to overlap with the composition of the nodule-rich bedrock points (black points). There may be a slight trend in the nodule-rich bedrock observation points to higher  $\text{FeO}_T$ , but these points did not exceed our criteria for  $\text{FeO}_T$  enrichment based on the ChemCam RMSEP. For rubbly targets (Figure S37), there were more nodule points enriched in CaO, MgO, and MnO, but these generally overlap with the composition of the nodular bedrock. The nodule-rich material and the nodules tend to be enriched in MnO compared to the median bedrock composition. There may be a slight trend in the nodule observation points along the  $\text{FeO}_T$ -MgO axis to higher  $\text{FeO}_T$  and MgO compositions, but these observation points did not exceed our criteria for  $\text{FeO}_T$  enrichment based on the ChemCam RMSEP.

Figure S38 shows the ternary plots for the Glasgow endmember. Besides the targets that belong to the Hutton endmember, The Glasgow endmember corresponds to the Glasgow stratigraphic unit. Most of the diagenetic ChemCam points in the database are in the Glasgow endmember. There is a strong mixing trend with Ca-sulfate. There is a trend along the  $\text{FeO}_T$  and MgO axis with some spread due to mixing with Ca-sulfate. The non-enriched nodules tend to fall on the  $\text{FeO}_T$ -rich side of the bedrock composition, but these observation points did not exceed our criteria for  $\text{FeO}_T$  enrichment based on the ChemCam RMSEP. This trend is extended by the nodules that are enriched in MgO and  $\text{FeO}_T$ . While there are a few MnO-rich nodules in Glasgow, there is no obvious trend between the nodules and the bedrock. The trend in the MnO nodules does not intersect the median bedrock composition; these nodules are slightly enriched in MgO and follow a trend that is similar to the trend of the nodules at

Groken/Mary Anning. The majority of these MnO-rich nodules in the Glasgow member were observed at the end of the second traverse near the polygonally fractured unit (see main manuscript). Hence, the MnO-rich nodules in Glasgow may be more closely related to the MnO-rich nodules at the Groken drill sample location.

Figure S39 shows the ternary plots for the Hutton endmember. These targets were located near the Hutton drill sample location at the top of Tower butte and at the top of Western Butte. These targets had the most extreme chemical compositions for MgO and FeO<sub>T</sub> in the MgO and F-rich linear features and MnO and FeO-rich dark-toned veins, respectively. The trends on the MgO-CaO-FeO<sub>T</sub> are less obvious due to mixing trend with Ca-sulfate. The nodules form a strong trend along the MgO-FeO<sub>T</sub> axis on the MgO-MnO-FeO<sub>T</sub> ternary diagram and illustrate the relationship between the linear features and the bedrock at Hutton. The relationship between the dark-toned veins and the bedrock and other diagenetic features at the Hutton location is not obvious, and this may be due to the low accuracy of the ChemCam MOC model for very high FeO<sub>T</sub> observation points (see manuscript).

Figure S40 shows the ternary plots for the Groken/Mary Anning endmember. These targets were located near the Groken/Mary Anning drill sample location. The bedrock and the nodular bedrock at this location was both enriched in MgO and MnO. There are strong mixing trends with Ca-sulfate that include the nodular bedrock and the material between the MnO-rich nodules in the Ayton ChemCam targets (see manuscript, Fig 7). There is a strong trend in MgO-FeO<sub>T</sub> to high FeO<sub>T</sub> in the dark strata, which is a unique category of diagenetic material only found at the Groken/Mary Anning drill location. The dark strata are also notably depleted in MnO compared to the bedrock and nodular bedrock at this location. However, there are four MnO-rich nodules observed with ChemCam within the dark strata that overlap with the Groken-type MnO-rich nodules. The bedrock, nodular bedrock, and MnO-rich nodules form a strong trend in this location. However, the nodules and the nodular bedrock overlap in MgO; these observation points did not exceed our criteria for MgO enrichment based on the ChemCam RMSEP.

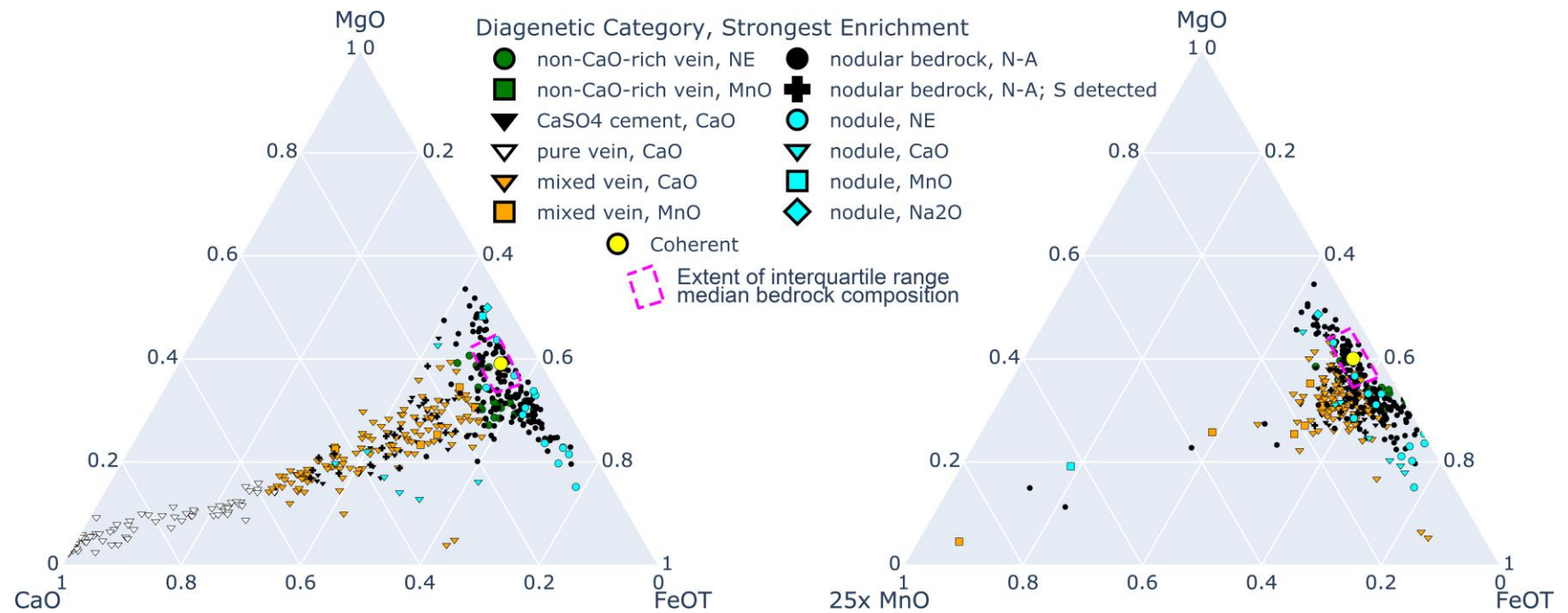


Figure S36: Ternary diagrams for the Coherent endmember bedrock and diagenetic features, categorized by diagenetic type and strongest enrichment. The median bedrock composition is plotted with the yellow symbol and the interquartile range is shown by the pink dashed area. Left: MgO-CaO-FeOT; Right: MgO-MnO-FeOT. The MgO-MnO-FeOT plot does not include the pure CaO veins.

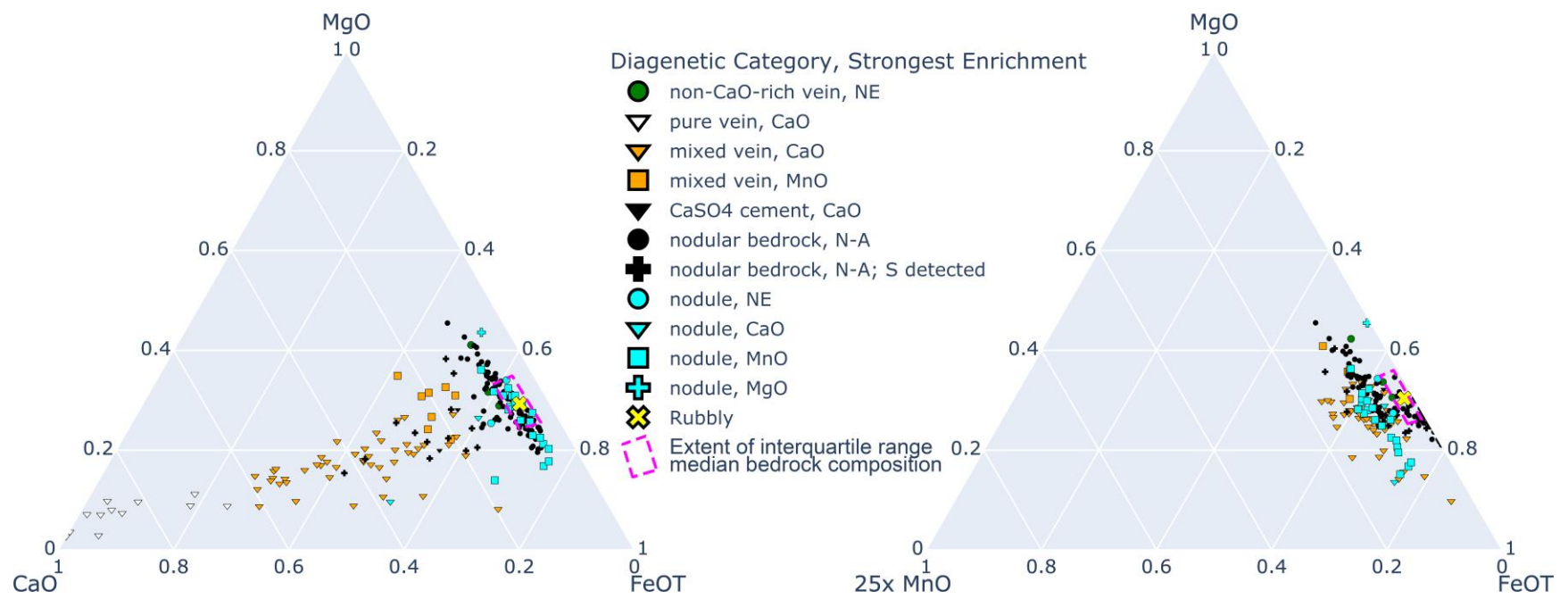


Figure S37: Ternary diagrams for the rubby endmember bedrock and diagenetic features, categorized by diagenetic type and strongest enrichment. The median bedrock composition is plotted with the yellow symbol and the interquartile range is shown by the pink dashed area. Left:  $\text{MgO}-\text{CaO}-\text{FeOT}$ ; Right:  $\text{MgO}-\text{MnO}-\text{FeOT}$ . The  $\text{MgO}-\text{MnO}-\text{FeOT}$  plot does not include the pure CaO veins.

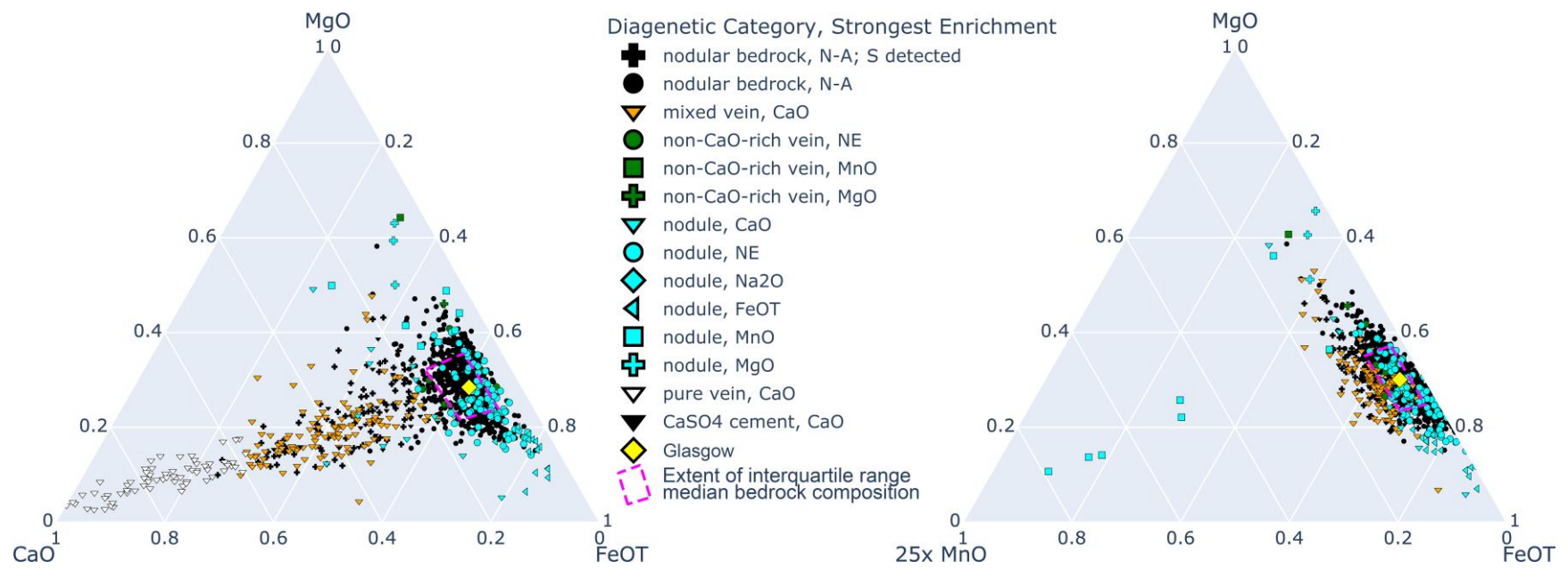


Figure S38: Ternary diagrams for the Glasgow endmember bedrock and diagenetic features, categorized by diagenetic type and strongest enrichment. The median bedrock composition is plotted with the yellow symbol and the interquartile range is shown by the pink dashed area. Left: MgO-CaO-FeOT; Right: MgO-MnO-FeOT. The MgO-MnO-FeOT plot does not include the pure CaO veins.

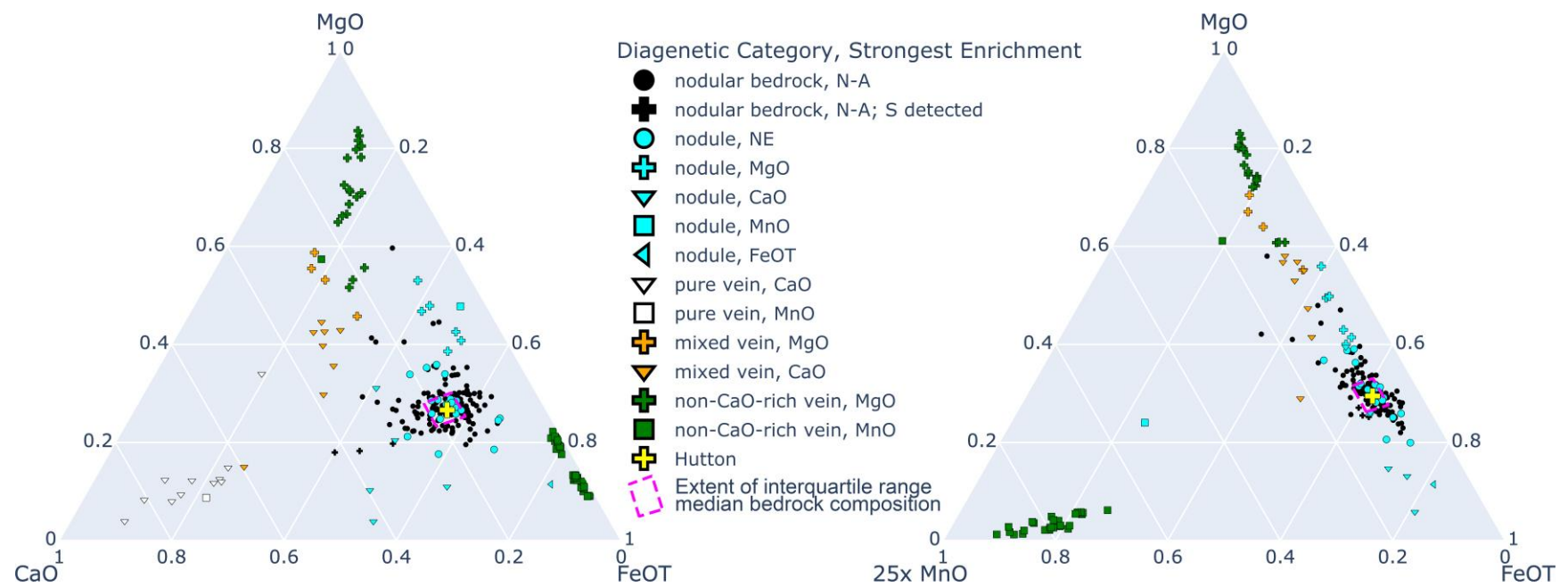


Figure S39: Ternary diagrams for the Hutton endmember bedrock and diagenetic features, categorized by diagenetic type and strongest enrichment. The median bedrock composition is plotted with the yellow symbol and the interquartile range is shown by the pink dashed area. Left: MgO-CaO-FeOT; Right: MgO-MnO-FeOT. The MgO-MnO-FeOT plot does not include the pure CaO veins.

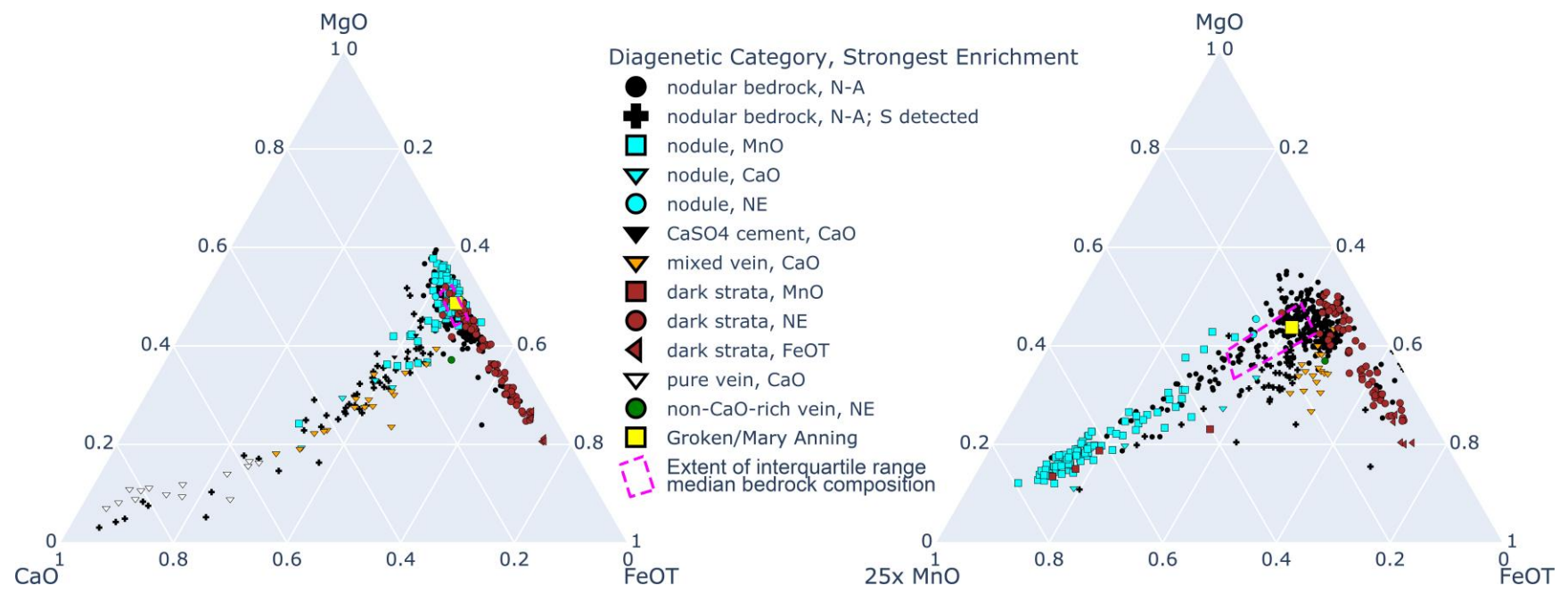
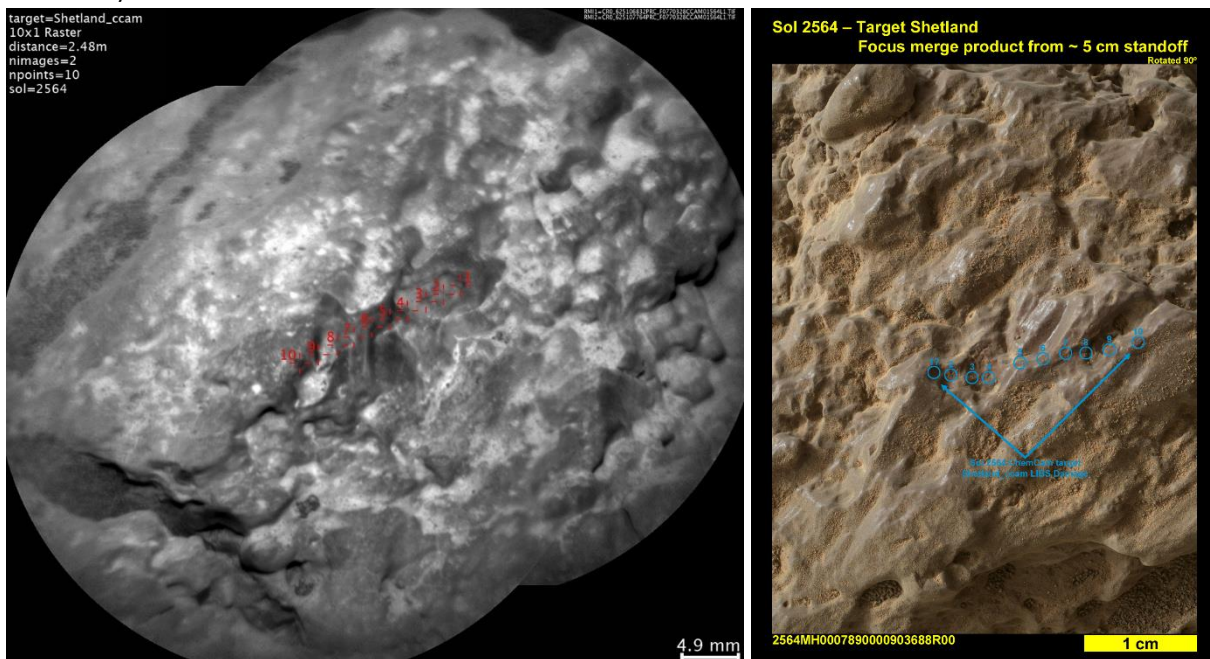


Figure S40: Ternary diagrams for the Groken/Mary Anning endmember bedrock and diagenetic features, categorized by diagenetic type and strongest enrichment. The median bedrock composition is plotted with the yellow symbol and the interquartile range is shown by the pink dashed area. Left: MgO-CaO-FeOT; Right: MgO-MnO-FeOT. The MgO-MnO-FeOT plot does not include the pure CaO veins.

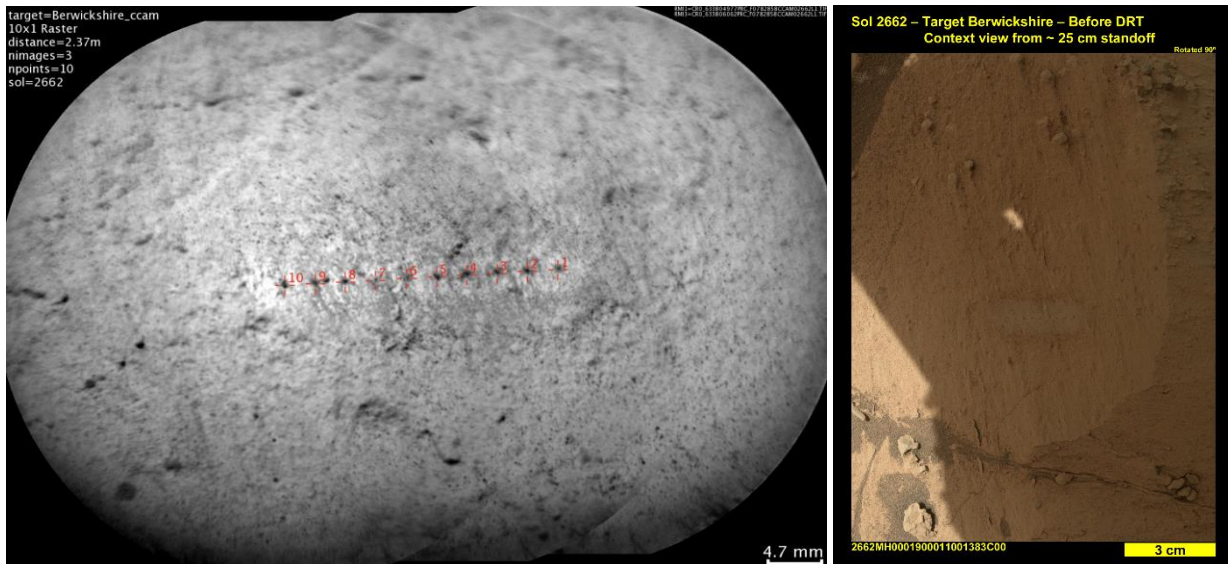
#### Text S4. Rubbly vs. Nodular; Nodules Out of Scope of RMI

Some ChemCam targets in the rubbly chemical endmember appear nodular at first glance, e.g., Shetland\_ccam (shown below); South\_Ronaldsay\_ccam; Blawhorn\_ccam; and Gorgie\_ccam (Figure S41). The target Shetland\_ccam has the appearance of being nodular because the polished texture and sun illuminating from the left contribute to the appearance of angular clasts (Figures S41). But the chemical endmember for this target is “rubbly”, and with the context provided by its corresponding MAHLI image, we determined that it simply had a rubbly texture, and was not nodular. Shetland\_ccam alone is shown below because it is representative of this phenomenon, which occurred in all four of the targets mentioned above. In these instances, we used the corresponding MAHLI images to obtain higher-resolution color context for the surrounding rock and determined that what appeared nodular was in fact just the rubbly nature of the rocks. This was further supported by these targets belonging to the rubbly chemical endmember.



Figures S41: The Shetland\_ccam ChemCam target RMI (sol 2564) and corresponding MAHLI image from ~5 cm standoff (2564MH0007890000903688R00).

In rare instances, as with the target Berwickshire\_ccam (Fig S42), and Everbay\_ccam (Fig S9), no nodules were visible in the RMI, yet the observation points were still classified as hitting nodule-rich bedrock. This is because we observed nodules in the Mastcam and MAHLI images corresponding to this target, but the RMI was zoomed in sufficiently far that it missed these nodules. In the corresponding MAHLI image (S42, right), several nodules can be seen near where the LIBS raster sampled. Thus, this target was classified as hitting nodule-rich bedrock. This is an instance of nodules outside the scope of the target’s RMI contributing to its nodular classification.



Figures S42: The Berwickshire\_ccam ChemCam target (sol 2662) and corresponding MAHLI image from ~25 cm standoff (2662MH0001900011001383Roo).

#### Text S5. CaO and MgO depth profiles

Throughout the traverse through Glen Torridon, CaO-rich targets were observed. CaO-rich targets were observed in both regular bedrock and nodule-rich bedrock. When a target was CaO-rich, as defined by our criterion based on RMSEP of an observation point compared to the local bedrock composition, we classified these targets as Ca-sulfate cemented when S was detected in the ChemCam spectra and when veins were not visible in RMI or MAHLI images of the target. In some cases, these targets are either relatively light-toned, or light-toned grains were observed embedded within the matrix of the target.

To analyze depth profiles, one must take into account the LIBS spot size, which varies from 100-500  $\mu\text{m}$  depending on the distance to the target and whether best focus was achieved, the amount of material ablated by each LIBS shot. LIBS depth profiles remove about 1-10  $\mu\text{m}$  per shot so that after a 30 shot depth profile, LIBS ablates up to ~300  $\mu\text{m}$  of rock. Comparing this value to the size of grains within a target can help determine whether a target is fine or coarse grained (Figure 2 in Rivera-Hernandez et al., 2019). In addition, MAHLI can reasonably discriminate 35  $\mu\text{m}$  size features in materials. In targets observed in Glen Torridon, in many cases, the targets with CaO enrichments did not display veins or grains that we could not attribute to the CaO enrichments or S detections. Hence, the features in these rocks are at least smaller than 35  $\mu\text{m}$  and could take multiple shots to penetrate through grains this size during a depth profile. In other cases, larger grains are present and MAHLI can distinguish them, making grains at least 35  $\mu\text{m}$ . These larger grains are still smaller than the spot size for LIBS; to penetrate through during a LIBS depth profile, it could take many 10s of shots (i.e., the entire depth profile). Either case could be consistent with cements. Since cements are usually thin coatings on grains, or pore fills between grains, they could be much thinner than a grain. LIBS depth profiles through coatings of known thickness have been tested previously and show that the chemical trends

are not as obvious and do not have sharp boundaries (Lanza et al., 2015). Hence, a depth profile may show a clear transition from one grain to another or from a grain into a thin coating like a cement.

Depth profiles may also help determine whether cements are present, but they are not definitive evidence of a cement, or of the lack of a cement. Taking the above factors into account, a depth profile is going to record the proportion of rock grains and the cement, if any, within the area of the LIBS spot. We will only see variations in the chemistry if the proportion of rock grains and cement change over the course of a depth profile (i.e., within the layers orthogonal to the LIBS ablation direction). This change in proportion must also change the chemistry enough such that in the oxide chemistry rises above the accuracy threshold that would indicate the chemistry has changed significantly. In many cases, the rock is homogeneous; i.e., the proportion of rock grains to cement does not change relative to the depth ablated during a LIBS analysis. In the cases where there are grains and cement that are larger than the depth that the laser is ablating with each shot, and the proportion of rock grain to cement is changing within the spot size, then a trend or variation in the oxide data may be present.

Figures S43-S59 show depth profiles for CaO and MgO in every observation point with likely Ca-sulfate cement. Each figure is sorted by endmember bedrock (coherent bedrock in Figs S43-S46; Hutton bedrock in S47; rubbly bedrock in Fig S48; Glasgow bedrock in S49-S55; and Mary Anning / Groken bedrock in S56-S59) and then in chronological order. Error bars (RMSEP) are plotted for each laser shot in depth profile. The first 5 points of each depth profile, overlain on each plot with a grey box, are contaminated with surface dust. MgO is plotted to determine if any potential Mg-sulfate is present in these targets. If the magnitude of MgO (Table S1) is, or rises above, the bedrock endmember composition, this may indicate that Mg-sulfate is present in the material. However, MgO is a major mineral oxide in the bedrock, and typically the MgO trend has a negative correlation with CaO, indicating the Mg is not present as a sulfate in most of these targets. In cases where MgO is significantly higher than the chemical endmember composition, and CaO and MgO are anti-correlated, this may indicate Mg-sulfate is present. In one target in the coherent bedrock and notably near to the sulfate unit, Ayre of Tonga, MgO and CaO have a positive correlation that could indicate Mg-sulfate (Fig S44). However, MgO in this target does not rise significantly above the bedrock MgO composition for the coherent endmember (7.35 wt% MgO), making it unlikely that this target has Mg-sulfate present.

We do observe depth trends that could indicate a Ca-sulfate within the targets. An overall positive trend in the target (e.g., Auchterarder Fig S43) could indicate the transition from rock at the surface to more predominately sulfate beneath the surface. Other targets have a “wedge” shaped or “S” shaped profiles (e.g. Gannet Fig S43), which could indicate a depth profile through a grain at the surface, sulfate layers, and then other grains. This situation could be indication of a cement that is ~10-20  $\mu\text{m}$  thick, or a very thin vein. Other targets show no trend but are enriched in CaO. This could indicate that the rock is very fine-grained or is homogeneous with respect to the proportion of grains and sulfates in the rock.

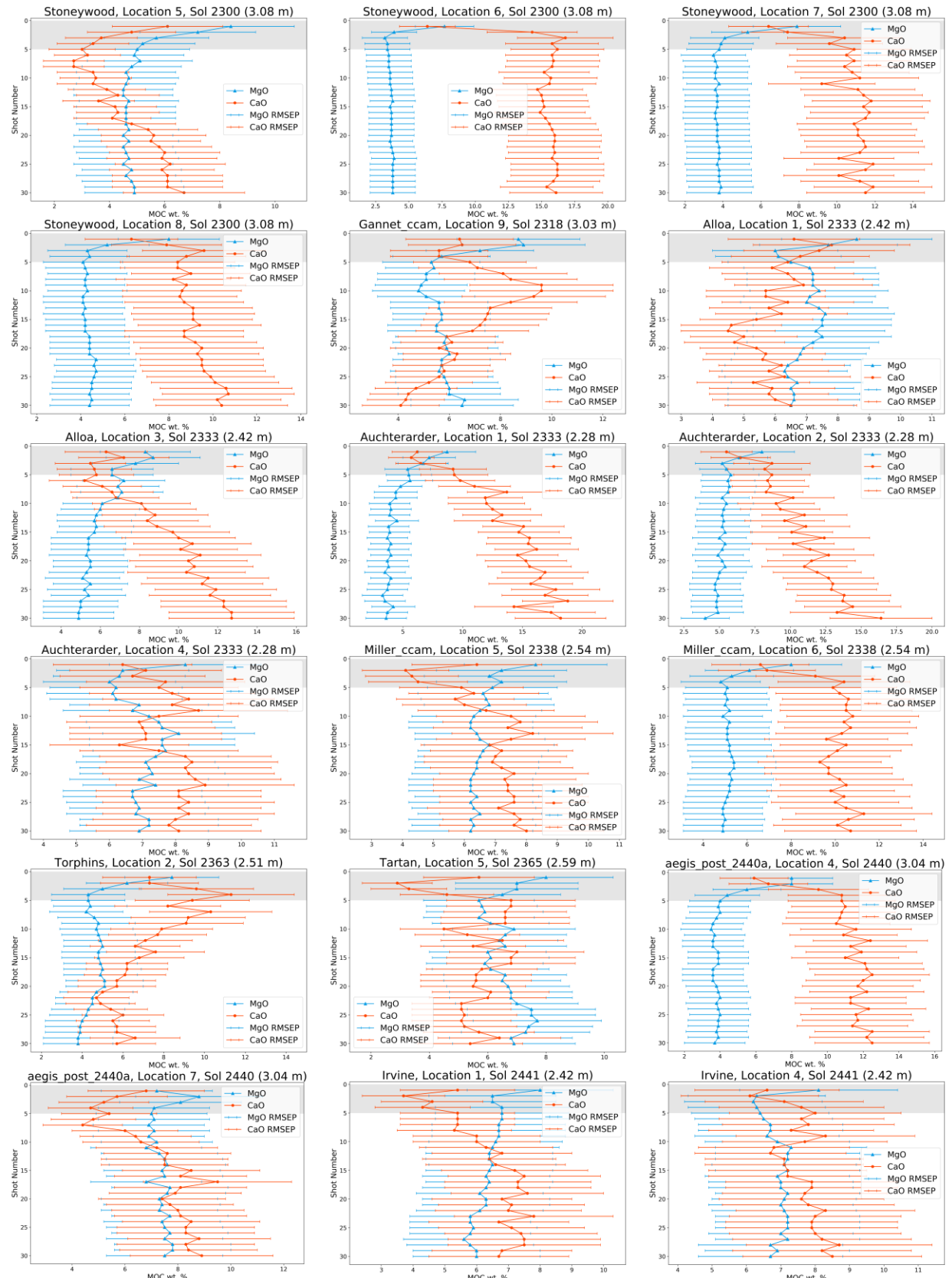


Figure S43: Depth trends of CaO (red) and MgO (blue) in likely cemented coherent observation points.

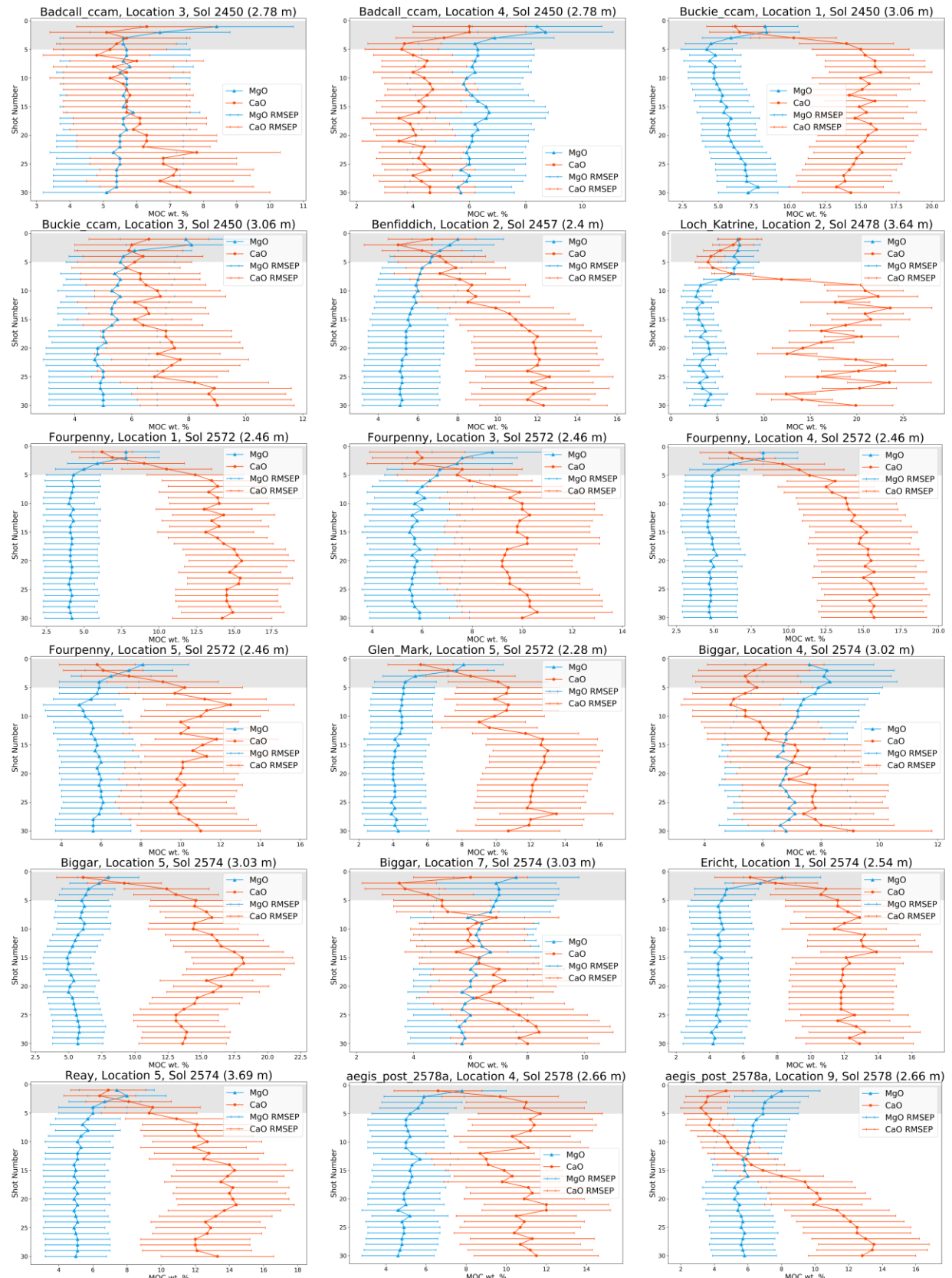


Figure S44: Depth trends of CaO (red) and MgO (blue) in likely cemented coherent observation points.

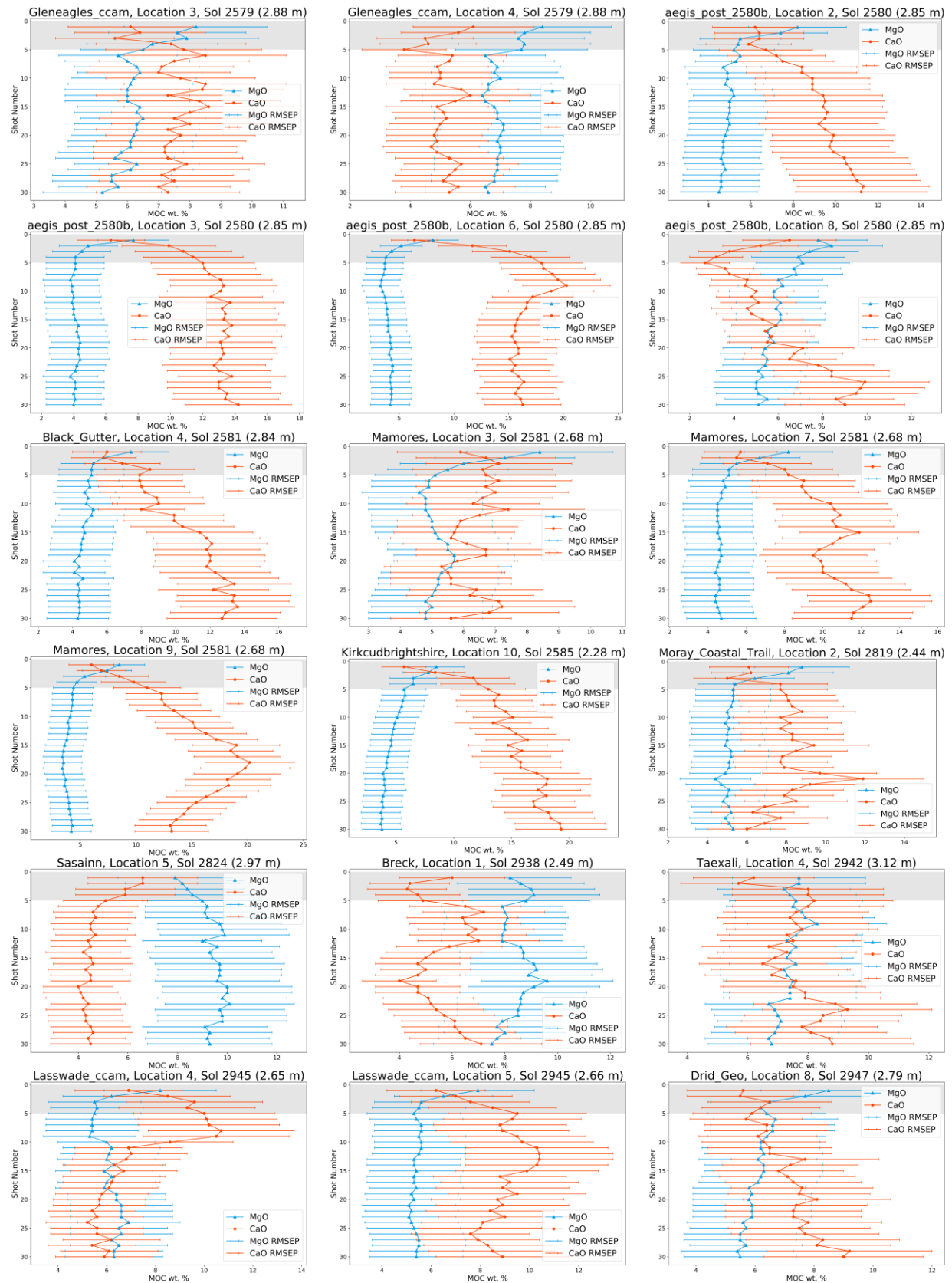


Figure S45: Depth trends of CaO (red) and MgO (blue) in likely cemented coherent observation points.

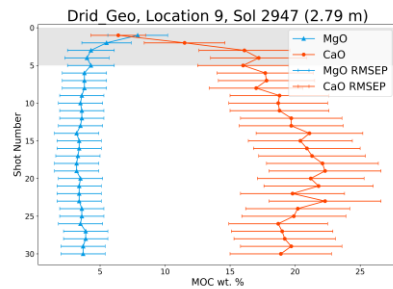


Figure S46: Depth trends of CaO (red) and MgO (blue) in likely cemented coherent observation points.

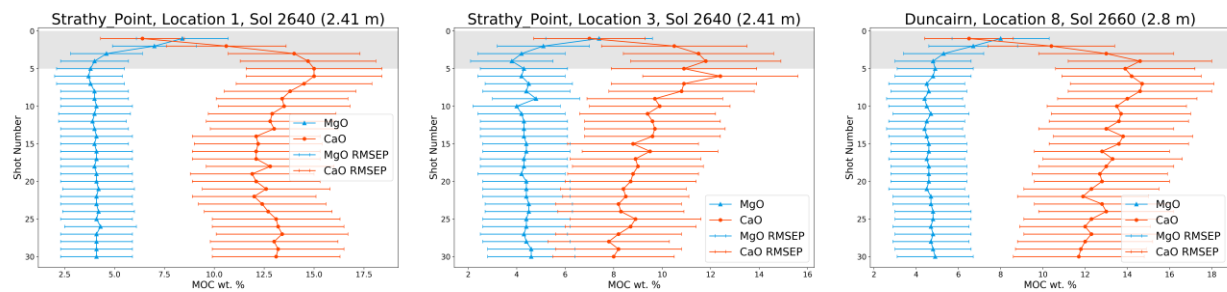


Figure S47: Depth trends of CaO (red) and MgO (blue) in likely cemented Hutton observation points.

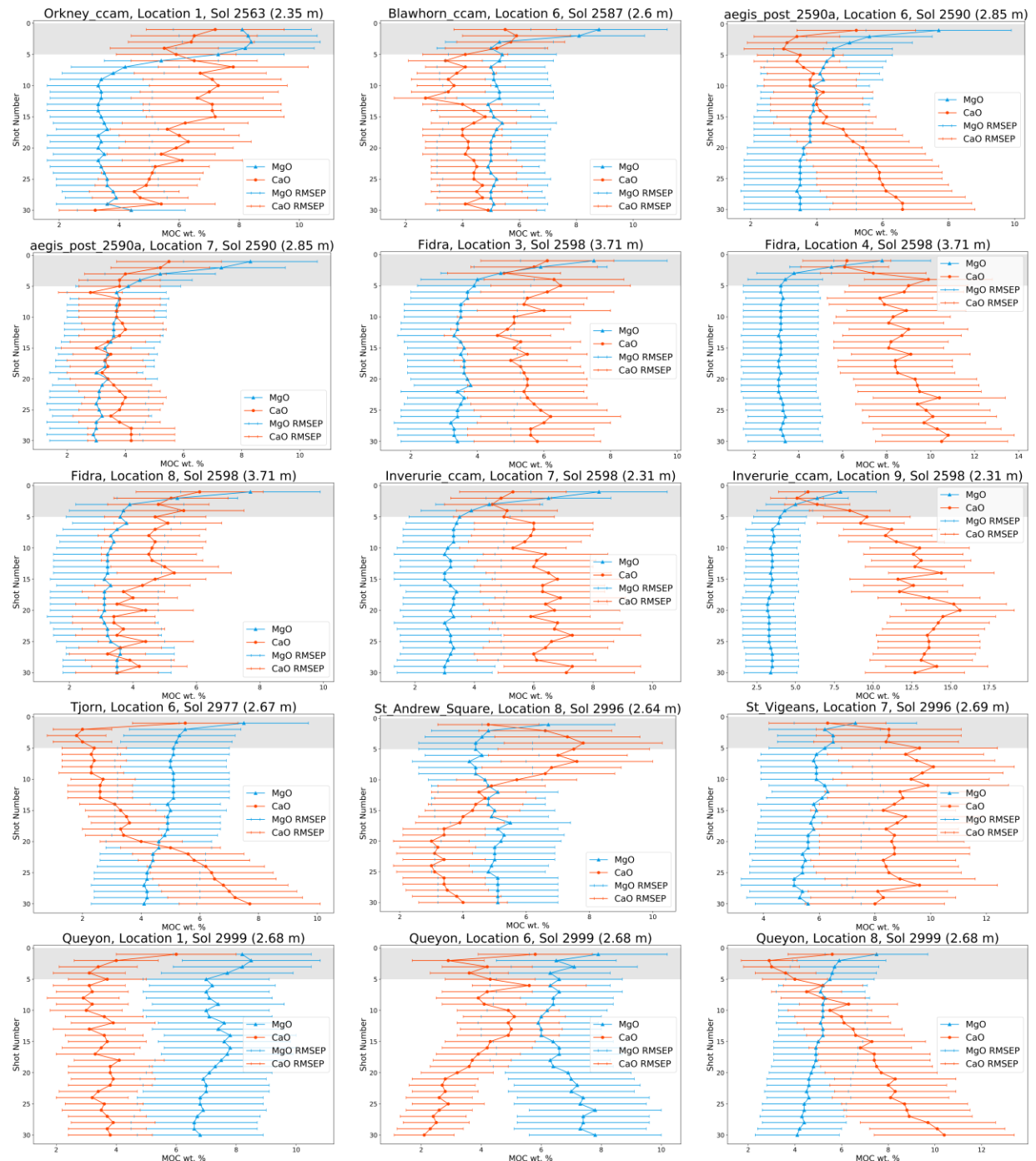


Figure S48: Depth trends of CaO (red) and MgO (blue) in likely cemented rubbly observation points.

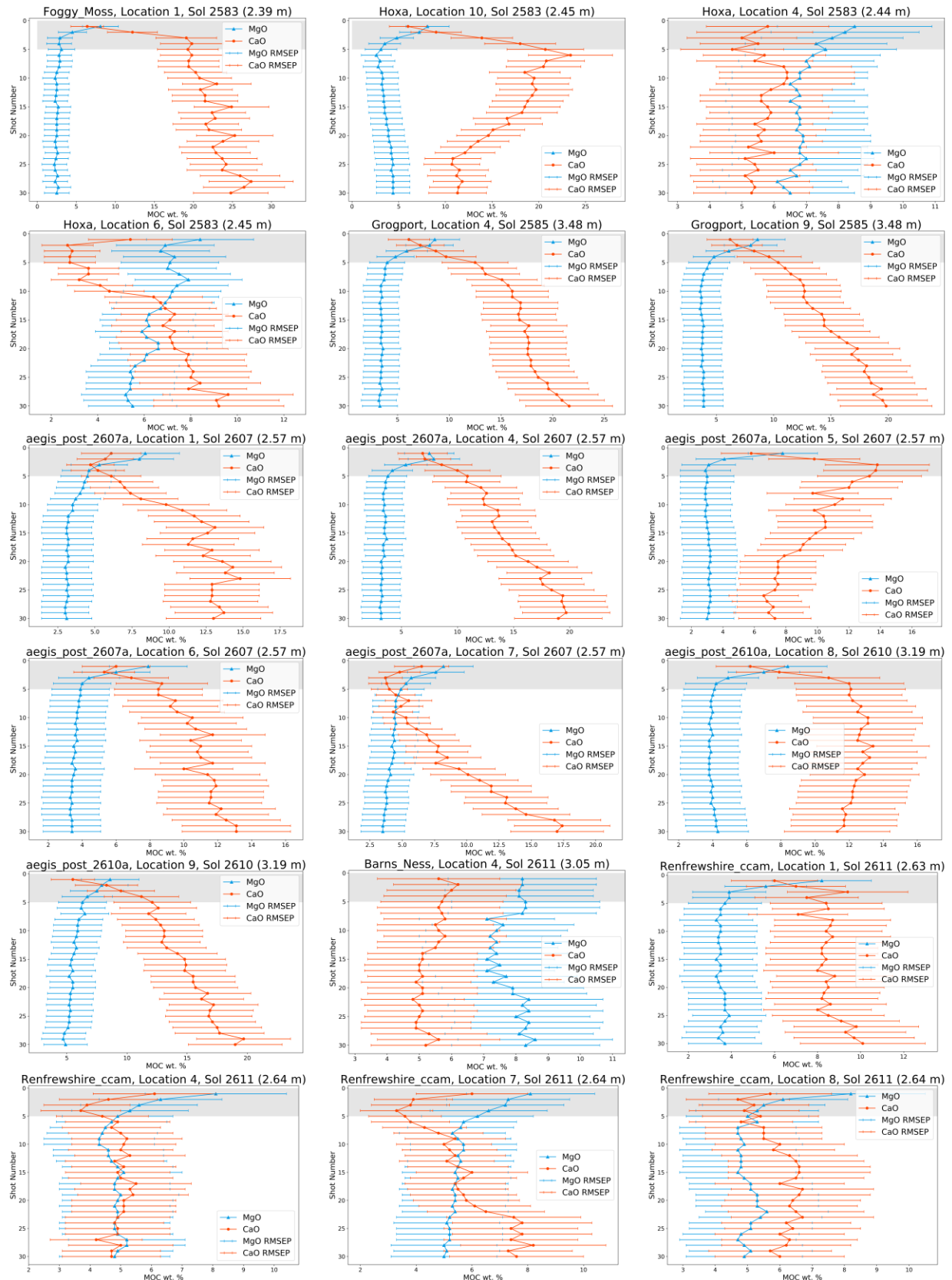


Figure S49: Depth trends of CaO (red) and MgO (blue) in likely cemented Glasgow observation points.

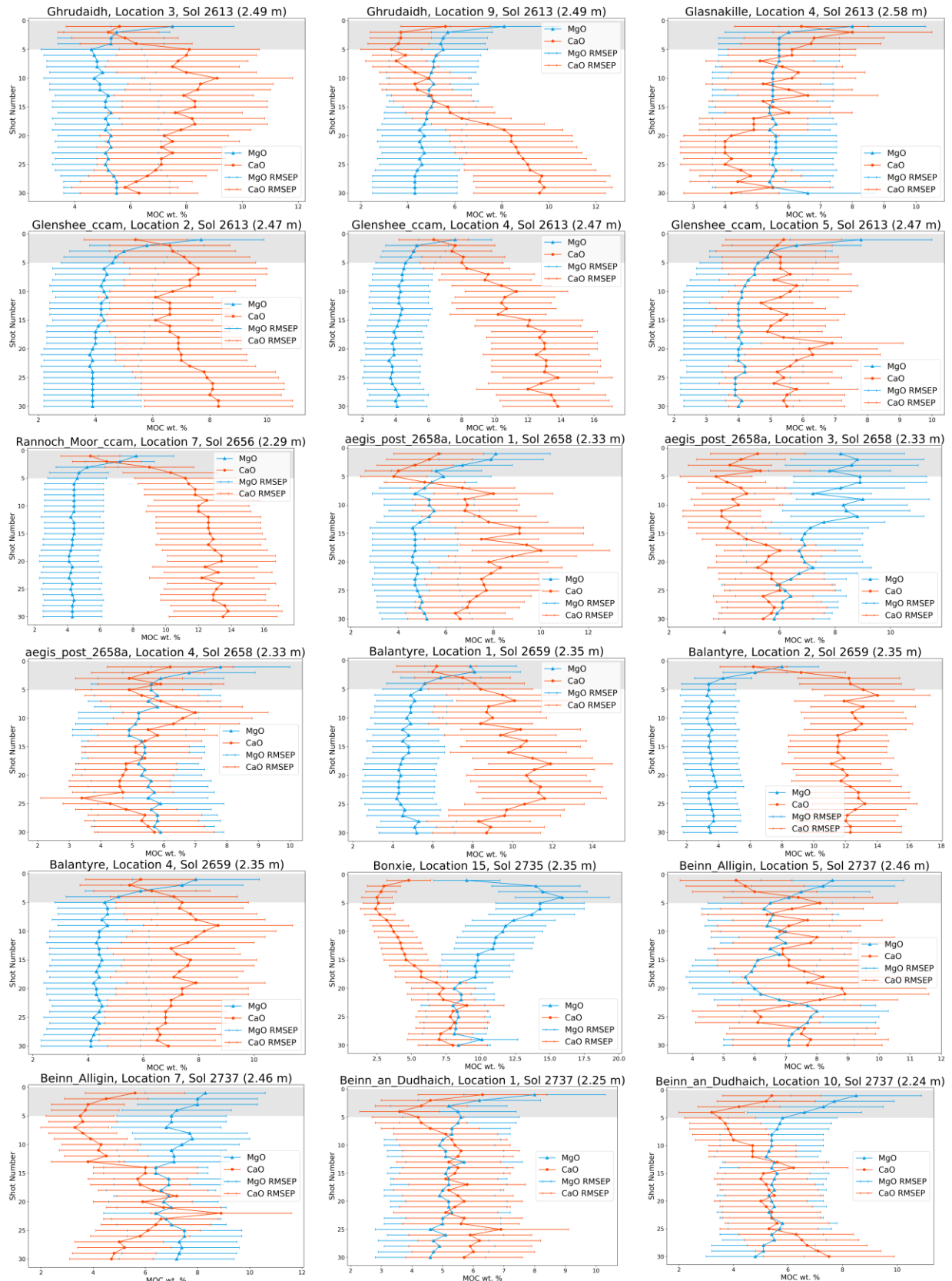


Figure S50: Depth trends of CaO (red) and MgO (blue) in likely cemented Glasgow observation points.

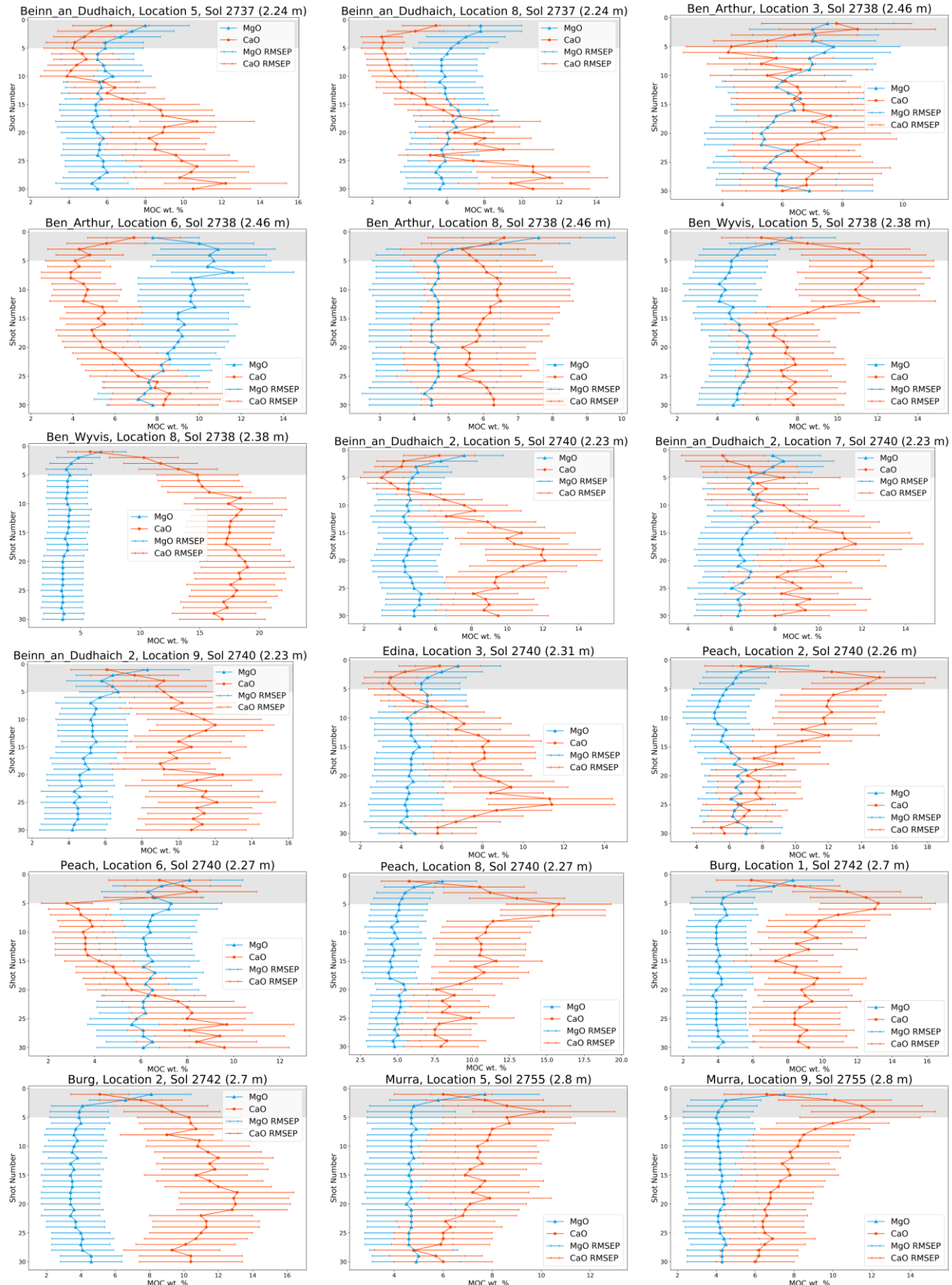


Figure S51: Depth trends of CaO (red) and MgO (blue) in likely cemented Glasgow observation points.

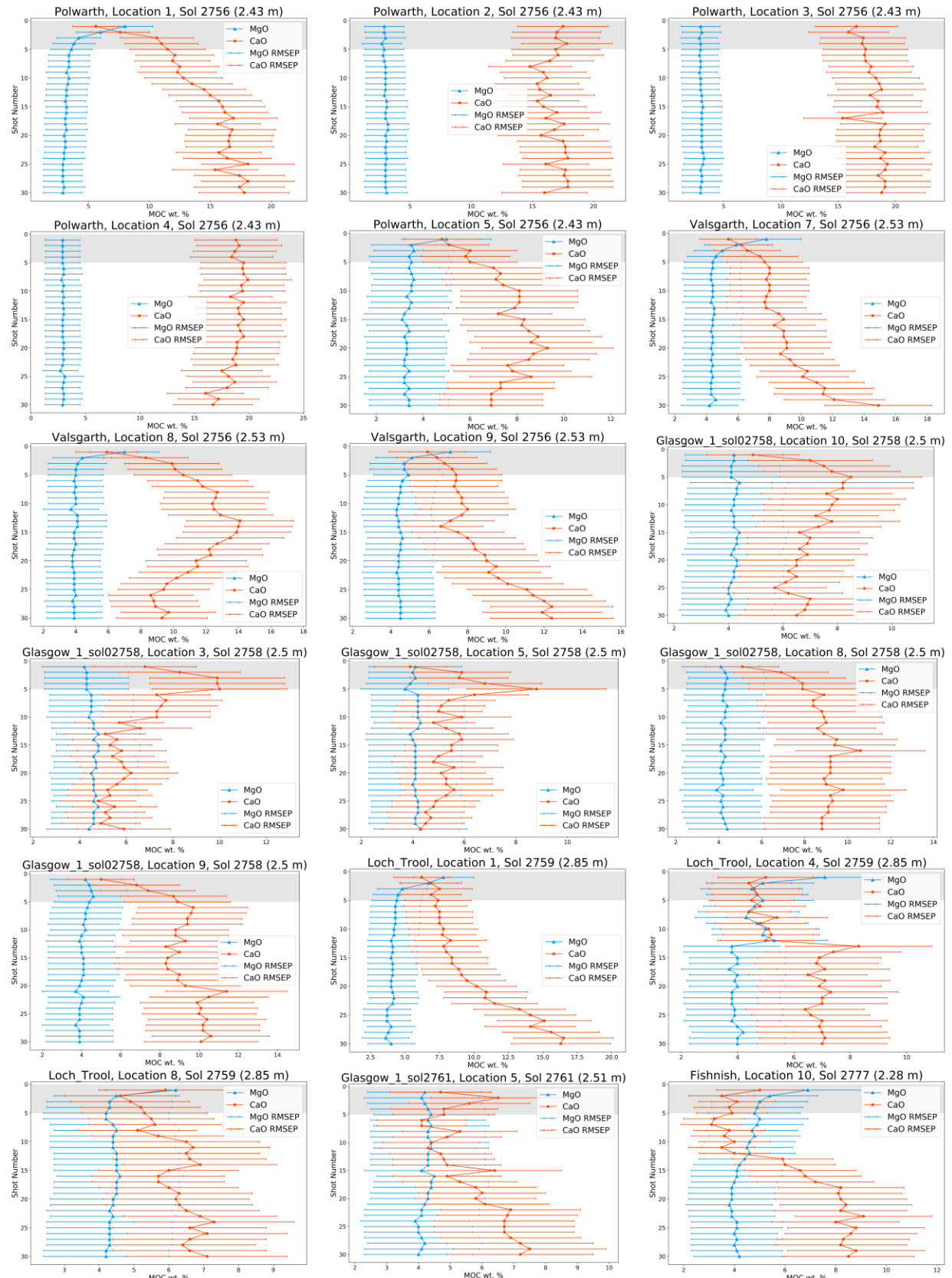


Figure S52: Depth trends of CaO (red) and MgO (blue) in likely cemented Glasgow observation points.

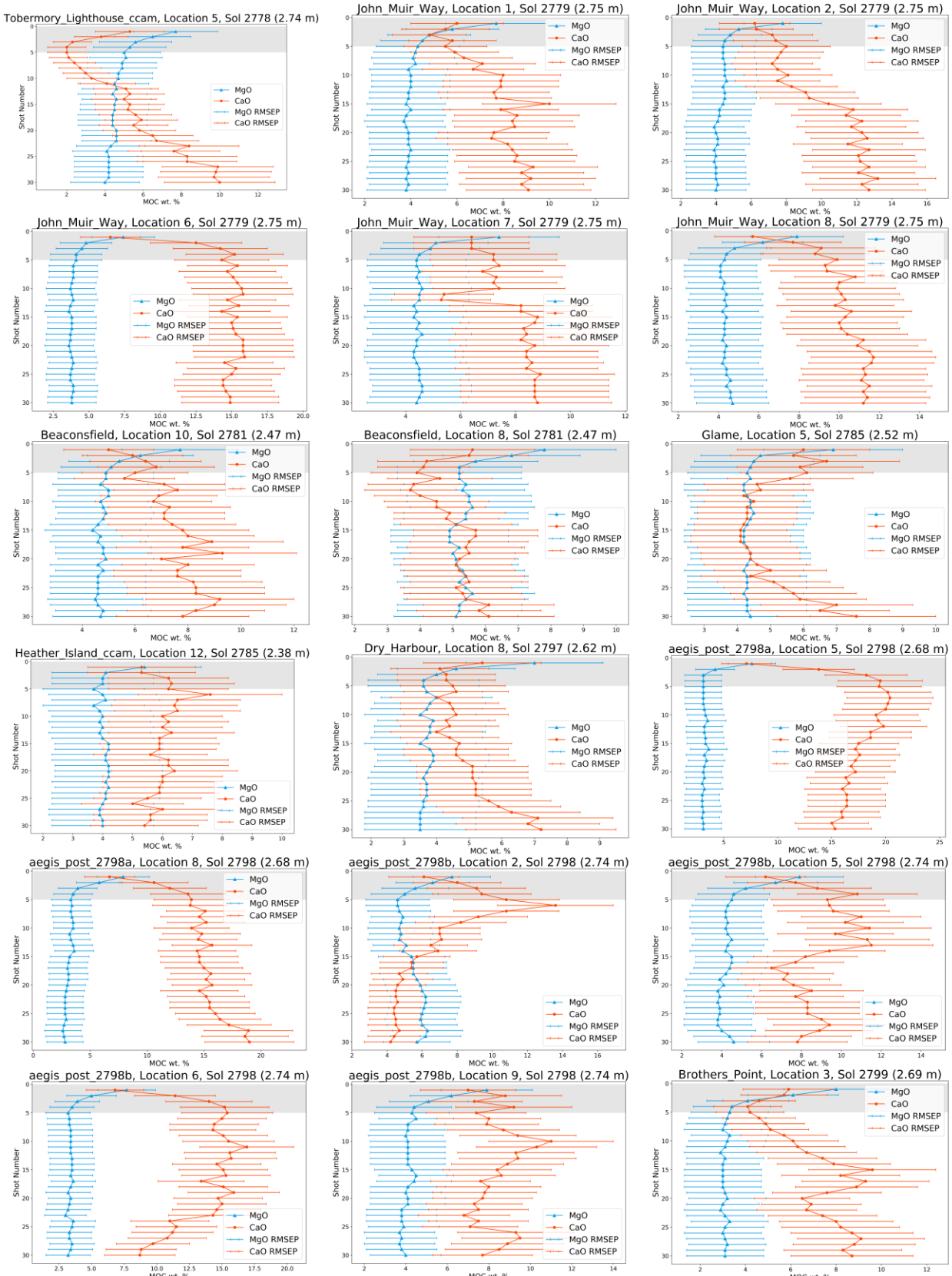


Figure S53: Depth trends of CaO (red) and MgO (blue) in likely cemented Glasgow observation points.

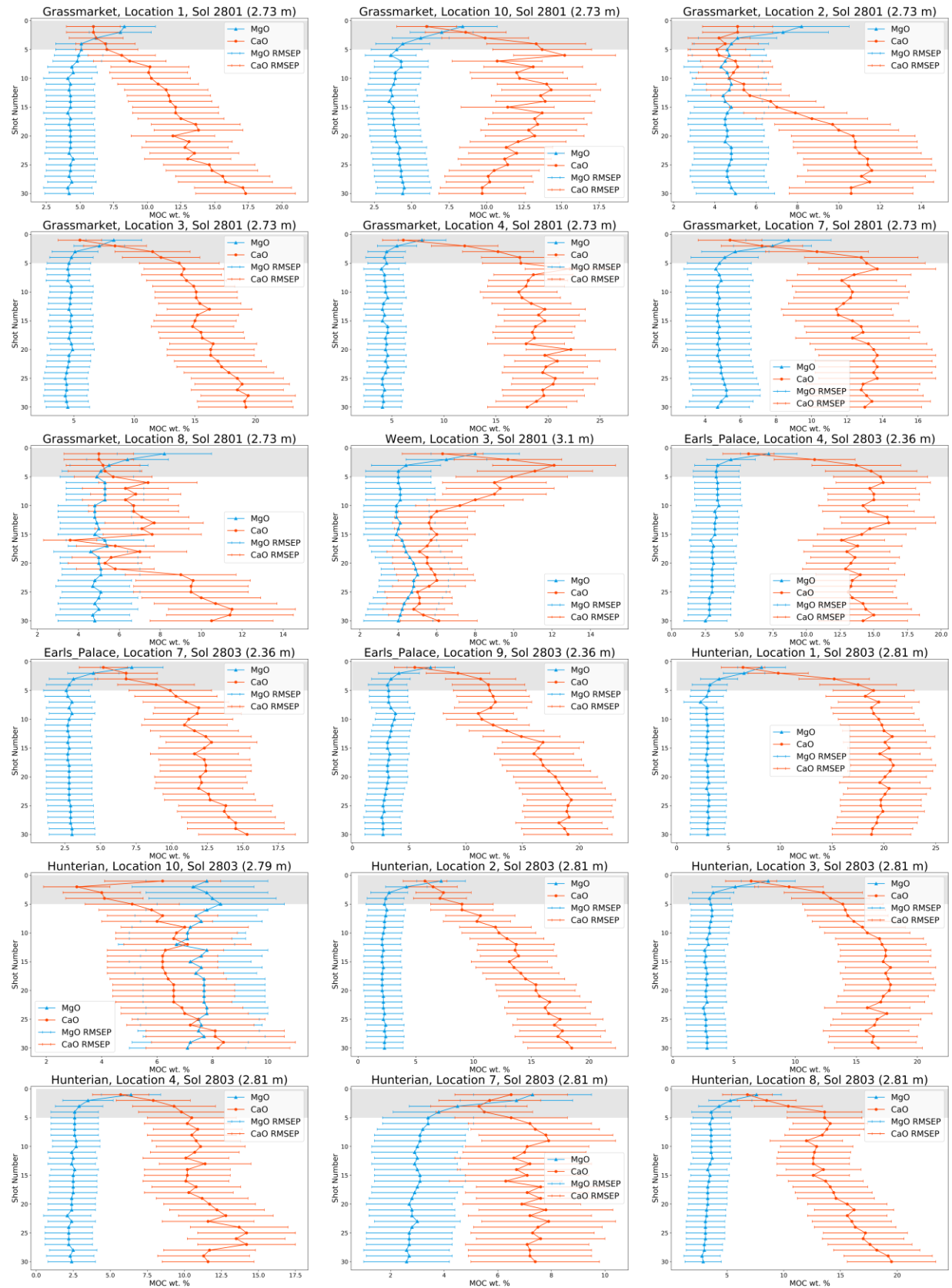


Figure S54: Depth trends of CaO (red) and MgO (blue) in likely cemented Glasgow observation points.

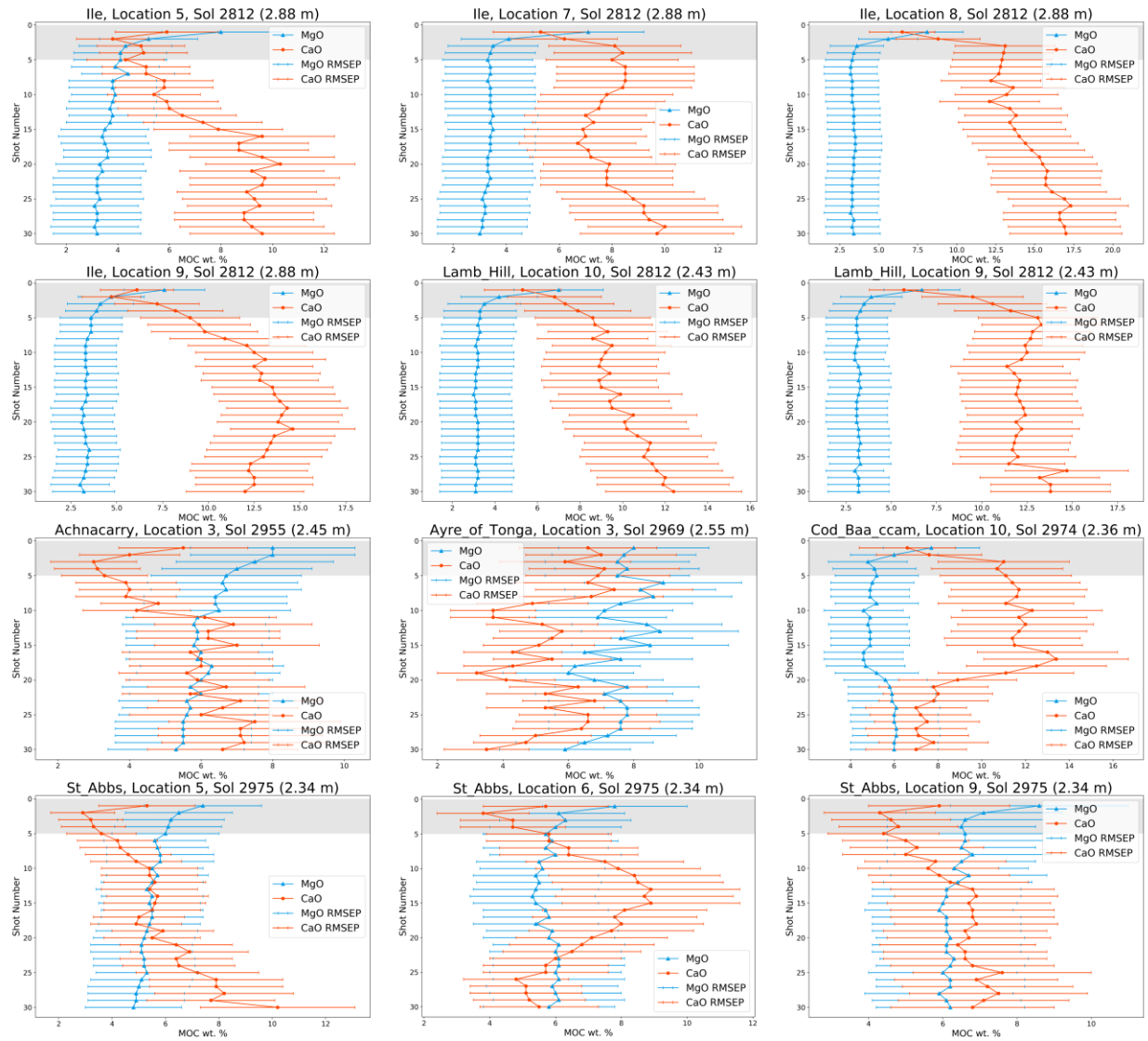


Figure S55: Depth trends of CaO (red) and MgO (blue) in likely cemented Glasgow observation points.

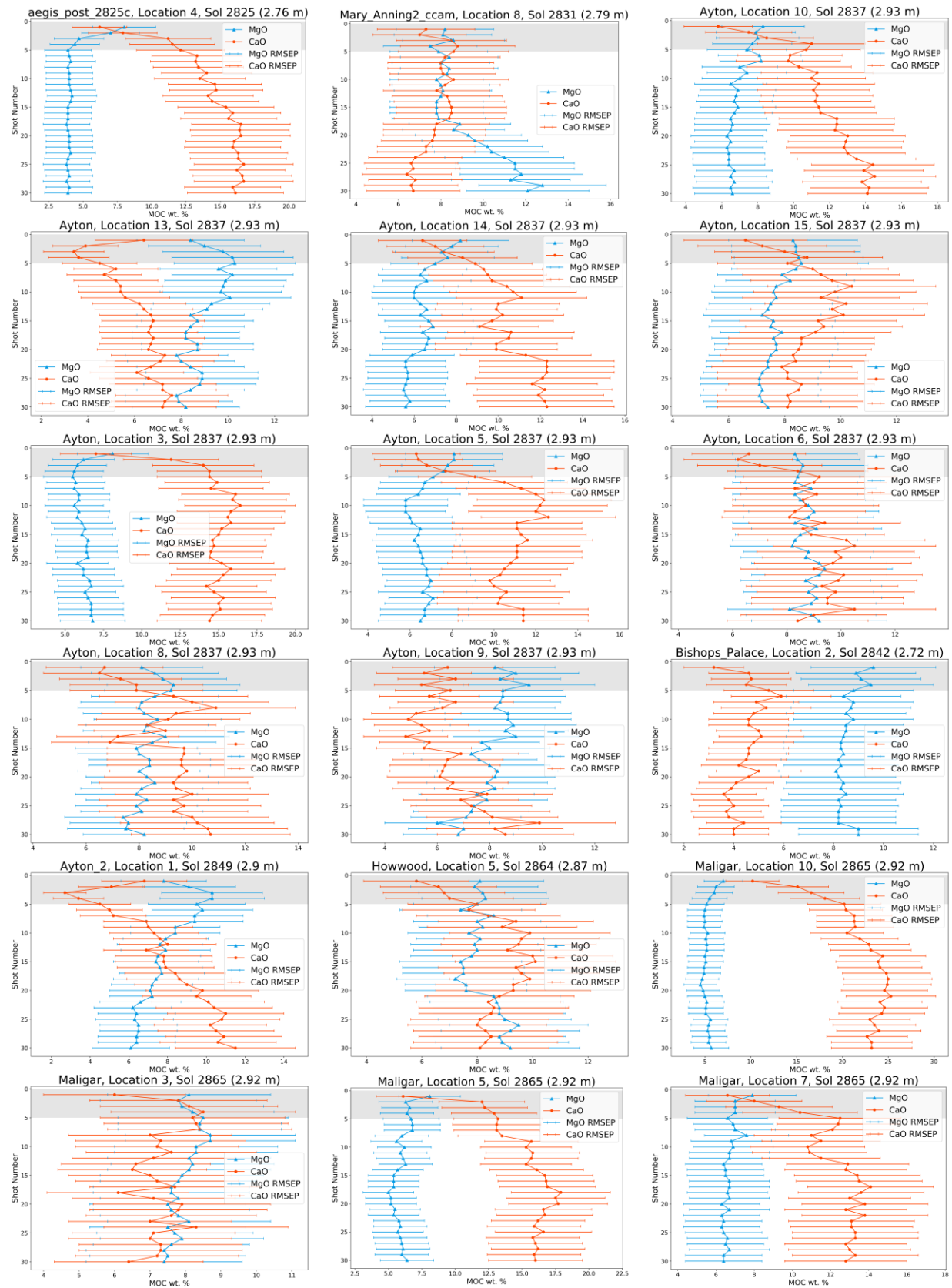


Figure S56: Depth trends of CaO (red) and MgO (blue) in likely cemented MA-GR observation points.

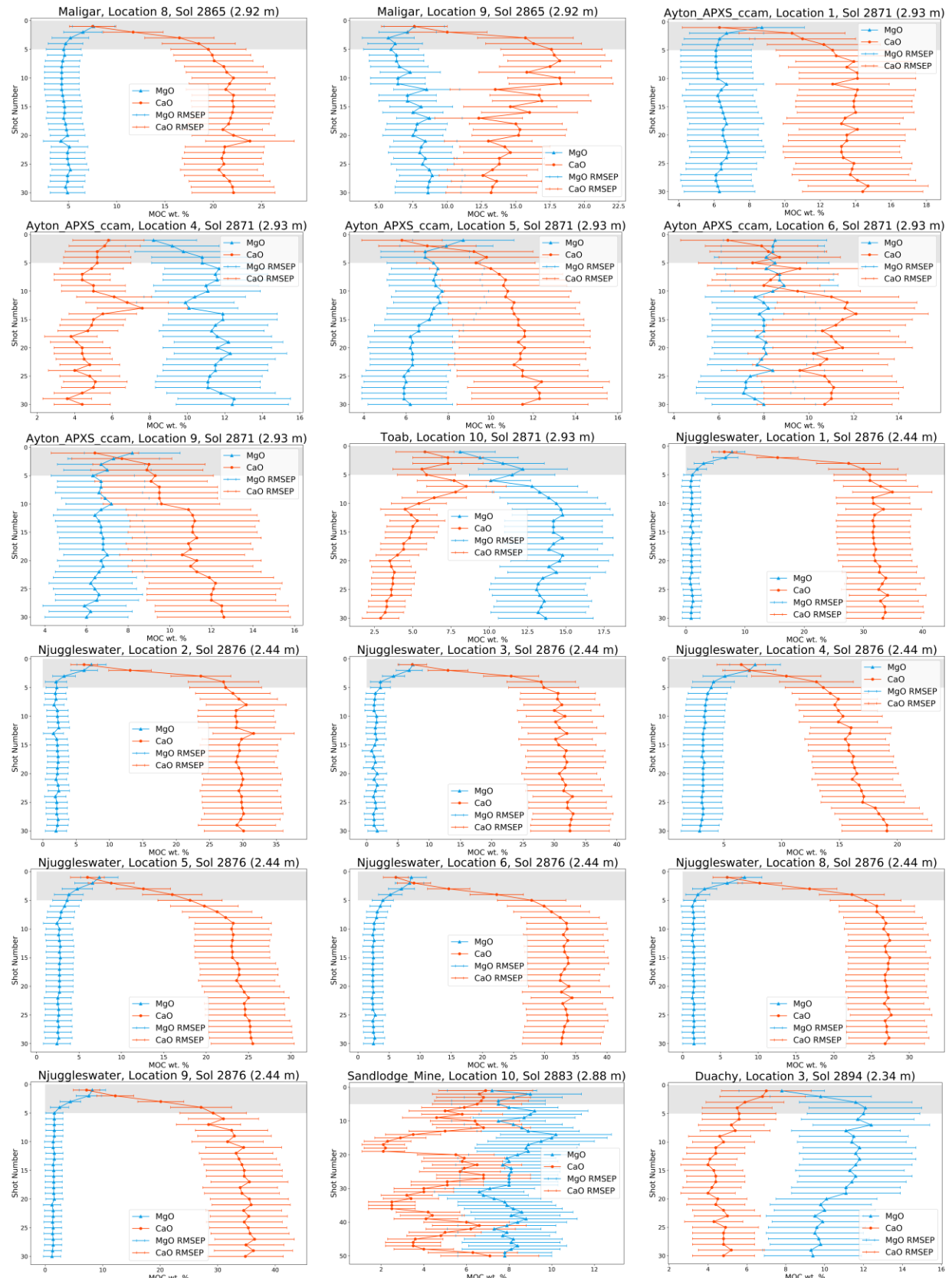


Figure S57: Depth trends of CaO (red) and MgO (blue) in likely cemented MA-GR observation points.

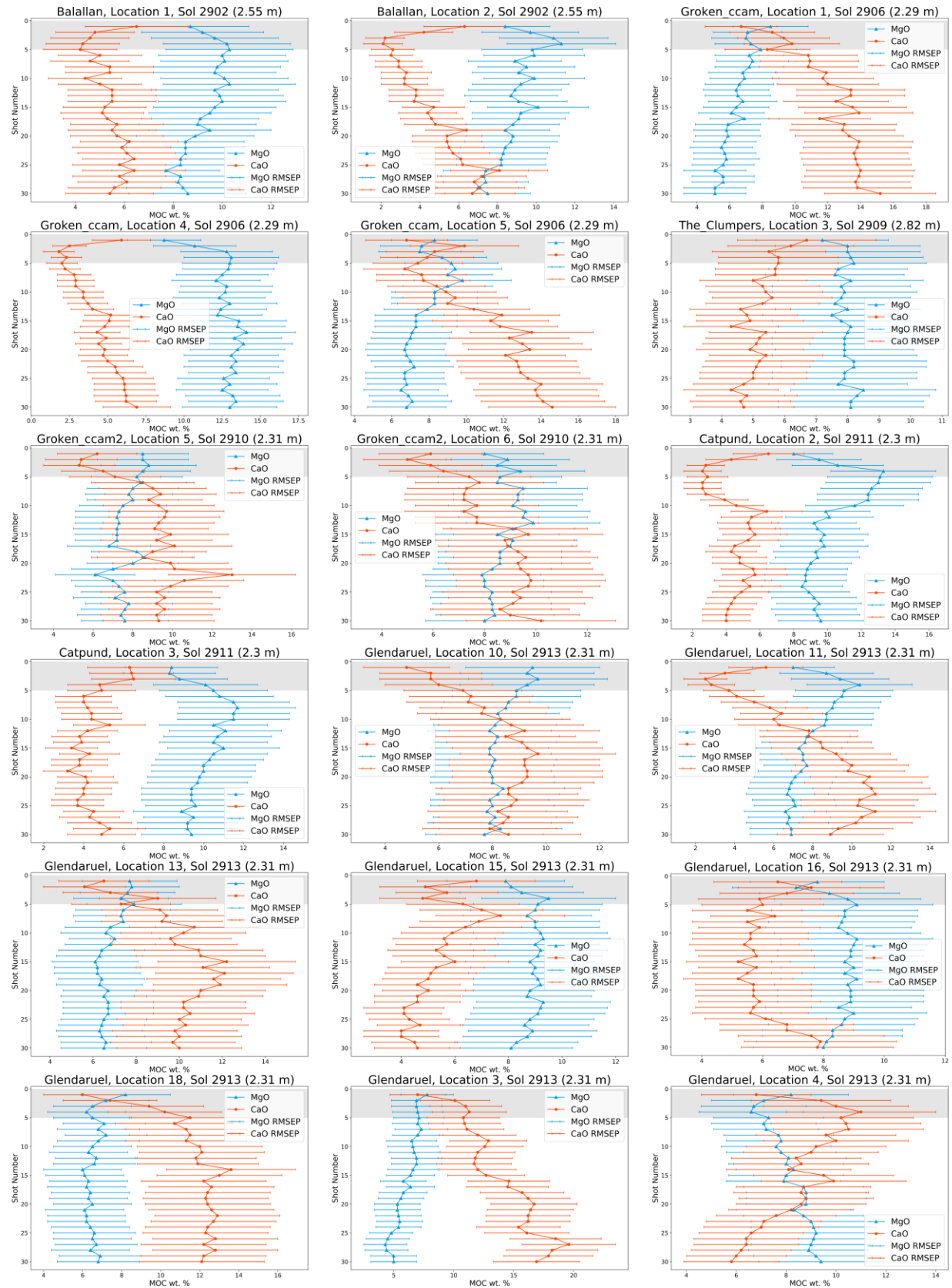


Figure S58: Depth trends of CaO (red) and MgO (blue) in likely cemented MA-GR observation points.

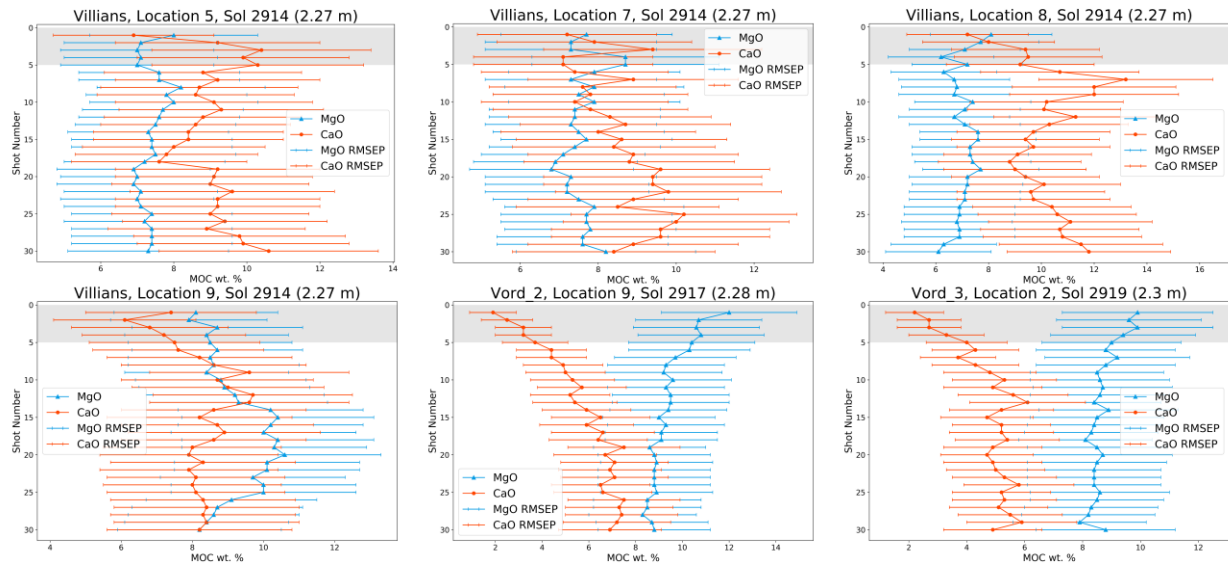


Figure S59: Depth trends of CaO (red) and MgO (blue) in likely cemented MA-GR observation points.

## Text S6. Pourbaix (Eh-pH diagrams) for Mn and Fe

### Text S6.1. Ayton Nodules

At the Mary Anning and Groken drill sample location, the rover observed Mn-rich nodules with P, and Fe-rich dark strata. If the Mn nodules are similar to nodules on Earth, they may contain a mixture of amorphous or microcrystalline phases such as todorokite, manganite, and goethite. Here, we model these phases using Geochemist's Workbench. When these three phases occur together, no major phosphate mineral is stable (Figure S6o). Only when Fe and Mn are separated, with the same amount of P present, does Mn phosphate become stable in most conditions, and the field for Fe phosphates grow (Figures S61 and S62). However, the MnHPO<sub>4</sub> phase is unlikely to form on Mars, as it is typically found in agricultural soil on Earth due to addition of P-rich fertilizer (Boyle and Lindsay, 1986).

When Fe and Mn oxides form in solution, they can adsorb P (adsorption is not modeled on the phase diagrams; see manuscript for references). These diagrams suggest that, if phosphates are present in Groken, they are most likely in the form of adsorbed P if they formed in neutral to alkaline conditions, and are more likely a phosphate phase if formed in more acidic conditions. The diagrams also suggest that Fe and Mn need to be in separate fluids (i.e., a Fe-rich fluid and a Mn-P-rich fluid) to avoid Fe phosphate formation/adsorption under most conditions.

Since the Chemin X-ray diffraction instrument did not detect any crystalline phosphate in the Groken sample (Thorpe et al., 2021), we may conclude from these diagrams that the fluids were likely neutral to alkaline, and more oxidizing (Eh > 0.5 volts). At these conditions, todorokite, manganite, and goethite are most stable, and these phases could adsorb some P from solution, if P were present.

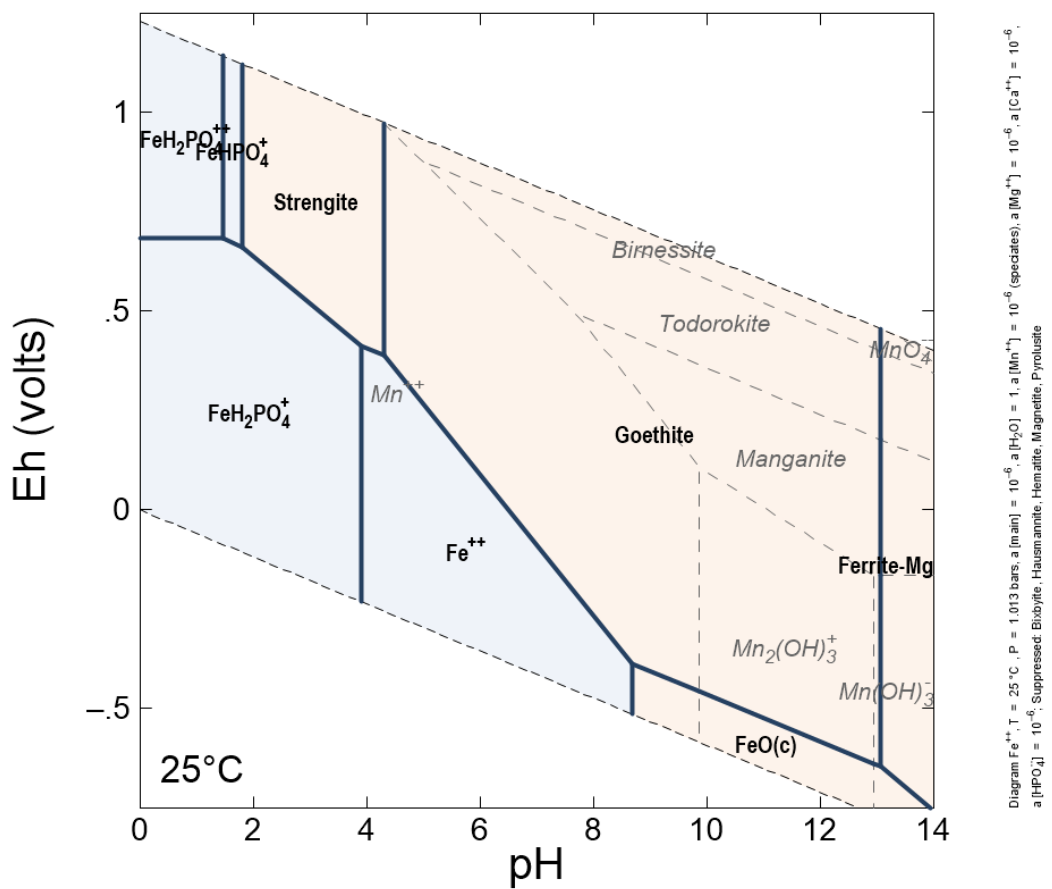


Figure S6o: Fe-Mn-Mg-Ca-P pH-Eh diagram in standard conditions. All species are  $10^{-6}$  M concentration in solution. Suppressed: bixbyite, hausmannite, hematite, magnetite, and pyrolusite.

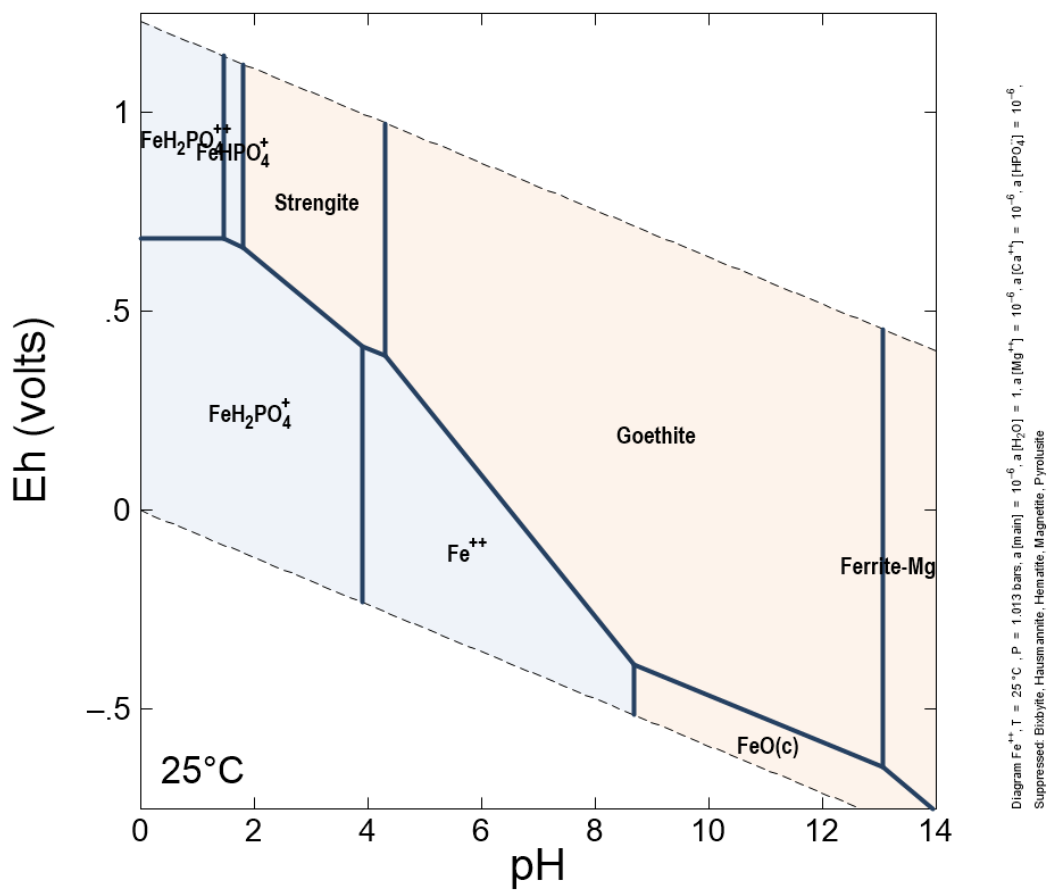


Figure S61: Fe -Mg-Ca-P pH-Eh diagram in standard conditions. All species are  $10^{-6}$  M concentration in solution. Suppressed: bixbyite, hausmannite, hematite, magnetite, and pyrolusite.

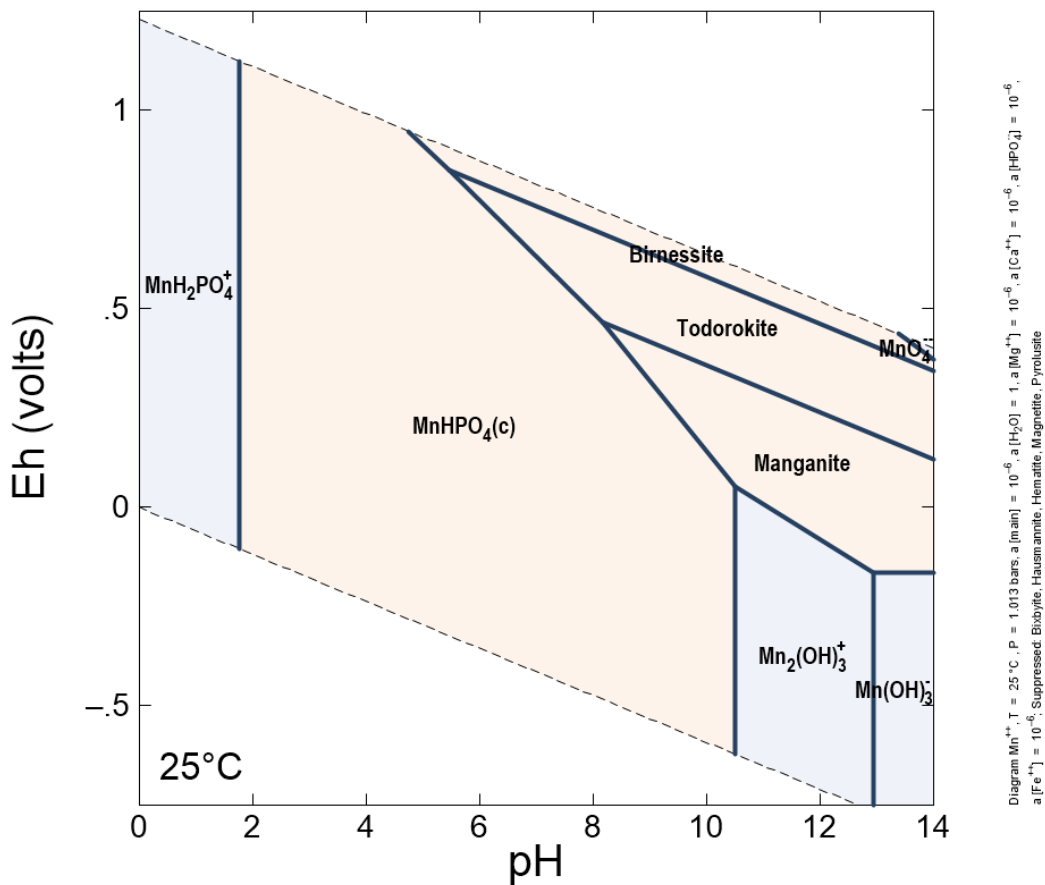


Figure S62: Mn-Mg-Ca-P pH-Eh diagram in standard conditions. All species are  $10^{-6}$  M concentration in solution. Suppressed: bixbyite, hausmannite, hematite, magnetite, and pyrolusite.

#### Text S6.2. Fe-Mn-Rich Dark-Toned Veins

At Hutton, we observed dark-toned veins with high Fe, Mn, and a large missing component that likely contains Ni, Cl, and H. The veins are spectrally flat in ChemCam passive reflectance data (Figure 6), which is consistent with magnetite, grey hematite (Fraeman et al., 2020a), and manganese oxides (Fox et al., 2015; Lanza et al., 2016). Although grey hematite is a possible phase, magnetite was detected in the bedrock directly adjacent to the veins in the Hutton drill sample (Thorpe et al., 2021).

Typically, magnetite forms in very reducing and alkaline conditions. Here, we model these phases using Geochemist's Workbench; Figures S63-S67 show that at lower temperatures, magnetite does not line up with any solid Mn phase. Only at temperatures  $>50^\circ\text{C}$  does a solid  $\text{Mn}(\text{OH})_2$  amorphous phase occur with magnetite at reducing and alkaline ( $\text{pH} > 10$ ) conditions. This stability field grows at higher temperatures ( $100^\circ\text{C}$ ) and is stable at slightly lower pH. At very high temperatures ( $200^\circ\text{C}$ ), the field begins to shrink (is overtaken by  $\text{Mn}(\text{OH})^+$  and hausmannite), but still overlaps with stable magnetite. These phase diagrams show that the veins likely formed at elevated temperatures and very reducing and alkaline conditions.

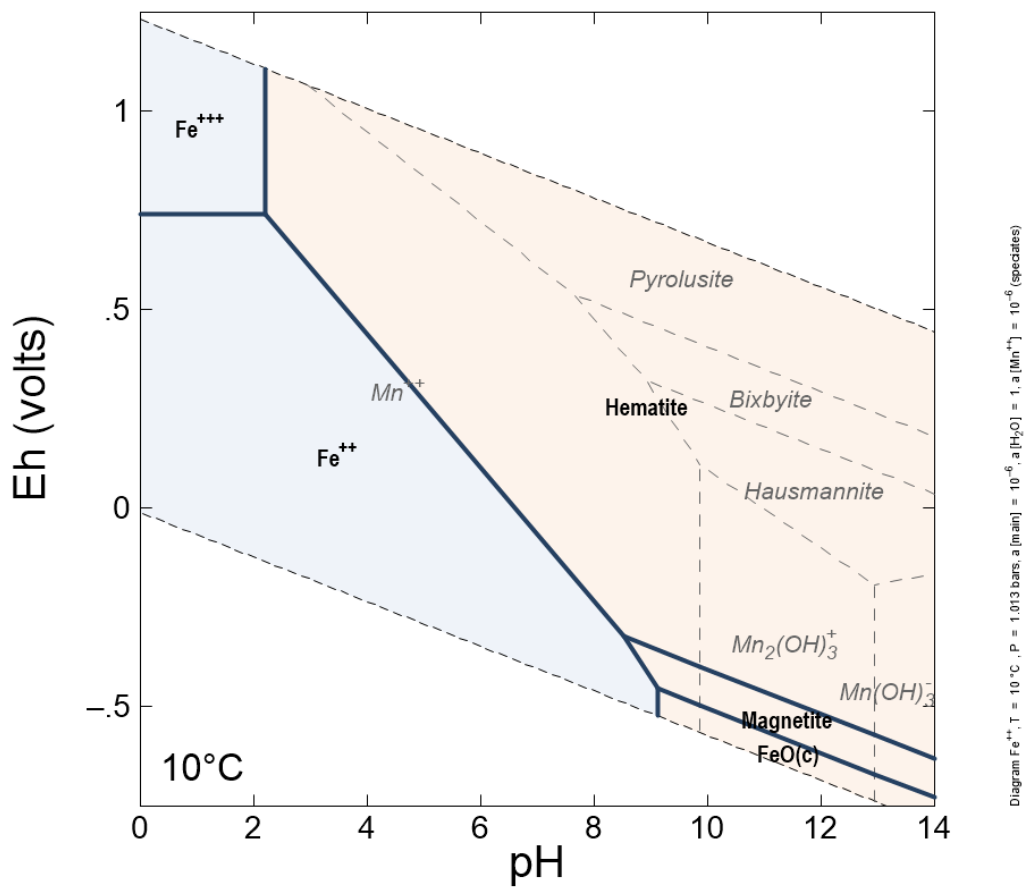


Figure S63: Fe-Mn pH-Eh diagram at 10°C. All species are  $10^{-6}$  M concentration in solution.

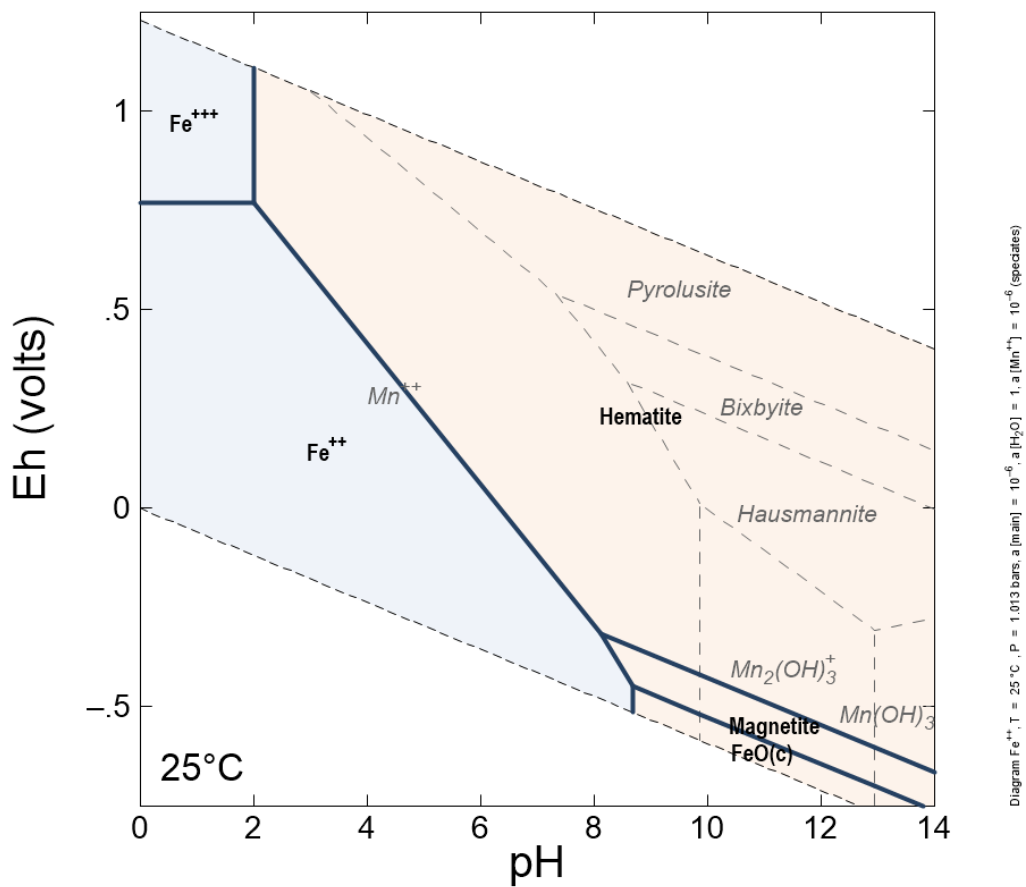


Figure S64: Fe-Mn pH-Eh diagram at 25°C. All species are  $10^{-6}$  M concentration in solution.

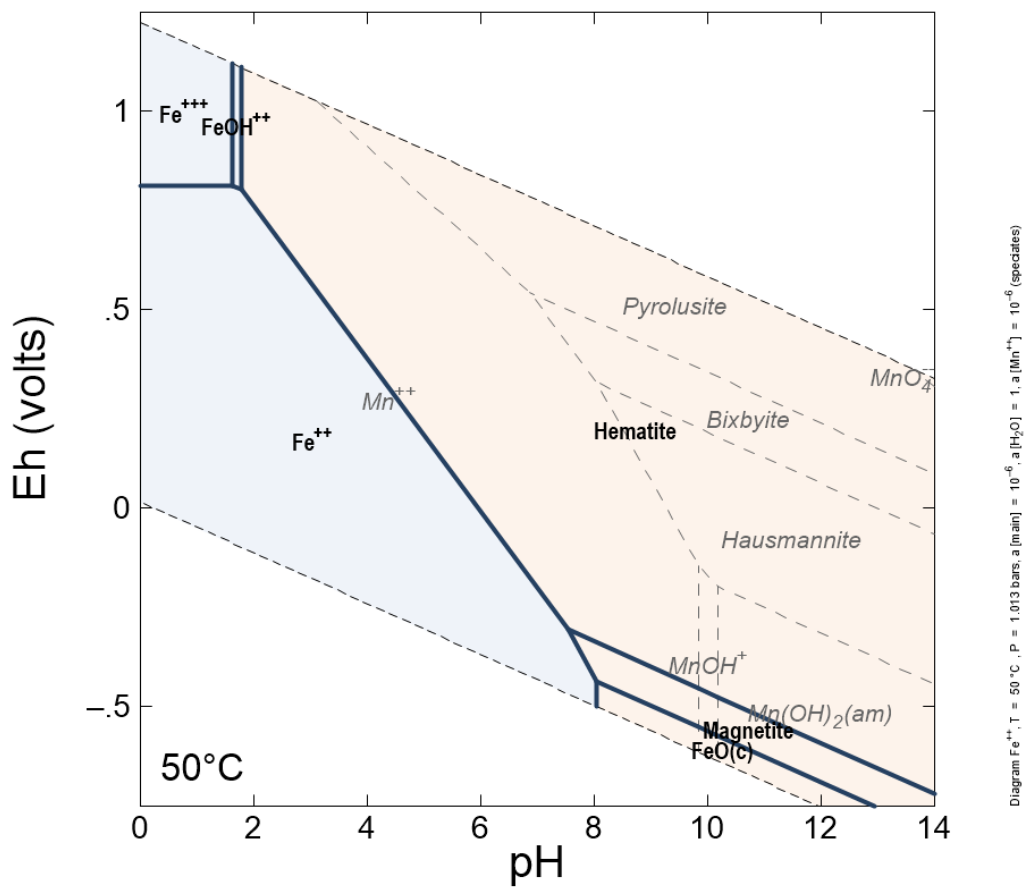


Figure S65: Fe-Mn pH-Eh diagram at 50°C. All species are  $10^{-6}$  M concentration in solution.

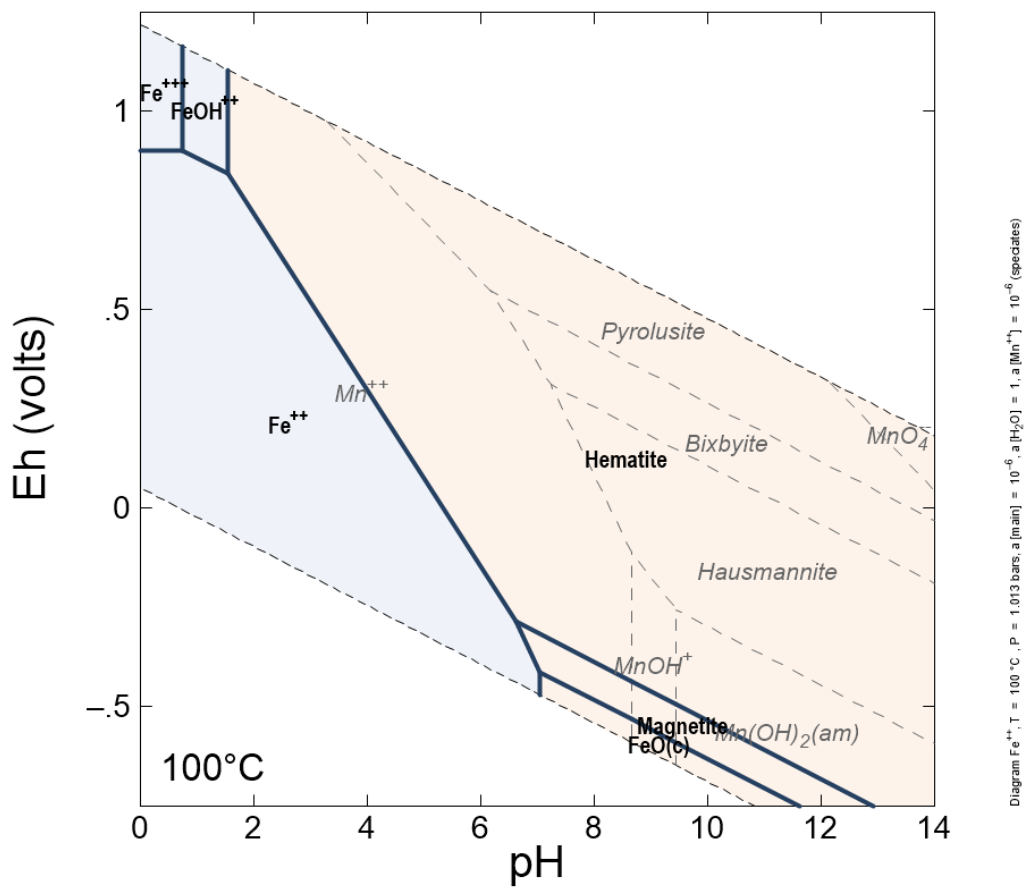


Figure S66: Fe-Mn pH-Eh diagram at 100°C. All species are  $10^{-6}$  M concentration in solution.

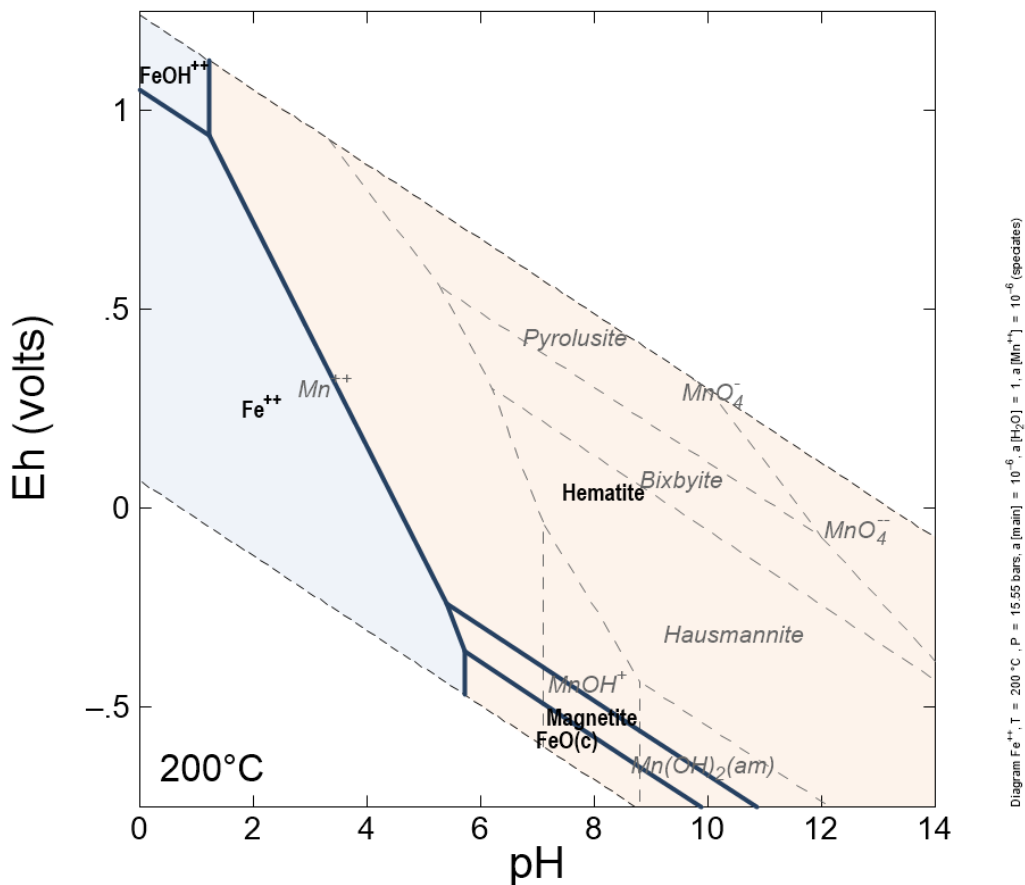


Figure S67: Fe-Mn pH-Eh diagram at 200°C. All species are  $10^{-6}$  M concentration in solution.

### Text S7. Extended Lithium Calibration

The previous univariate Li calibration model by Payré et al. (2017a) can accurately predict Li concentrations up to 72 ppm Li. In Glen Torridon, ChemCam observed Li lines in the spectra that were predicted above this threshold using the Payré et al. (2017a) model. Hence, we are required to develop an extension to the model by Payré et al. (2017a) to accurately predict Li in these following ChemCam targets that predicted values above 72 ppm Li in Glen Torridon Mt Sharp group rocks covered by this manuscript: Glen\_Rosa, aegis\_post2689a, Glen\_Cannish, Glenmoriston, and Glen\_Rosa\_DP. Several targets in other regions of *Curiosity*'s traverse also predicted Li values above 72 ppm Li, such as Idyllwild, Eaglesham, Eaglesham\_2, Marquette, Frome\_Rocks, McSherrys, Blanco\_Mountain, Aneth, Ouray, and Rocknest3\_2. We used the Python programming language to build an extended univariate Li calibration model using peak area data from the Li peak at 670.98 nm (Figure S68). The peak area data used in this model was extracted from ChemCam spectra using peak-fitting in IDL (Payré et al., 2017a). We used the curve\_fit method from the Python library scipy.optimize to optimize a power law function fit  $f(x) = (Ax^B)$  to the data (Virtanen et al., 2020).

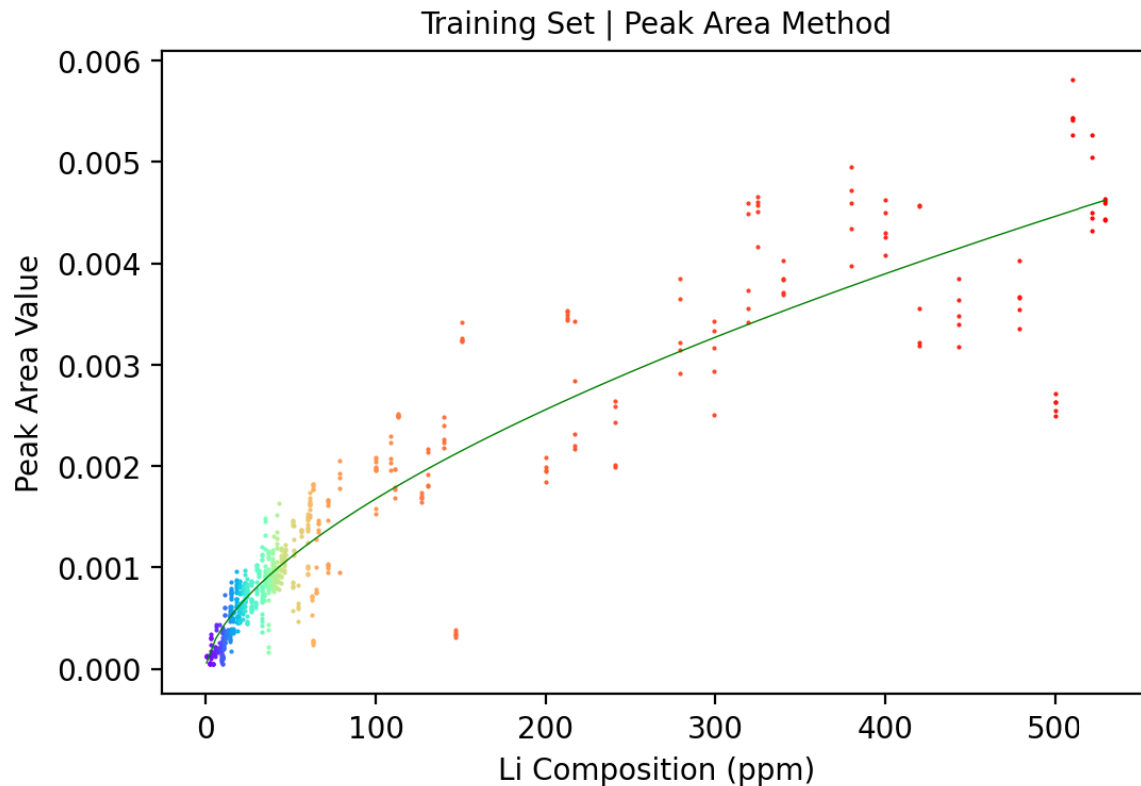


Figure S68: The calibration curve showing the peak area vs the actual Li composition of 139 standards spanning from 0.4 ppm to 530 ppm Li. The green line represents the calibration curve that uses a power law function to fit the data. Warmer colors of each dot represent higher Li standard composition of each sample measured.

Equation from the model:  $f(x) = 1.0204 \times 10^{-4} (x^{0.608})$

To increase the density of samples in our dataset with high-Li compositions, we made 15 mixtures with Li concentrations between 200 ppm and 500 ppm in increments of 20 ppm. We used two standards with high Li as dopants (OU9 and NCSDC86303) to combine with several samples with low Li to dilute the mixtures' Li compositions to the desired values. Our first dopant, OU9, is a complex-type, petalite-subtype pegmatite. NCSDC86303 is a Li ore standard that contains petalite, potassium feldspar, sodium feldspar, lepidolite, spodumene, lithium muscovite, and quartz. For a list of all the samples used in this model and their compositions, these are available on the PDS ChemCam Calibration Database (Wiens et al., 2021b).

The training set for the new model described here consists of 139 Li-bearing standards spanning from 0.4 ppm to 530 ppm Li. All of the standards below 72 ppm were used in the previous Li calibration model (Payré et. al 2017a). The test set was produced using five stratified folds where fold 3 (20% of the data) was held out as the test set. The test set includes 38 targets distributed from 0.4 ppm to 530 ppm Li.

To determine the accuracy of this model, we calculate root mean squared error of the predictions (RMSEP) ( $\sqrt{(\sum |actual - predicted|^2 / n)}$ ), where n is the number of spectra in the test set, using the actual and predicted values of samples within our test set. When only considering samples in the test set above 70 ppm, the RMSEP is 48.7 ppm (Figure S69). The average RMSEP of the entire model (0–530 ppm) is 26 ppm (Figure S70).

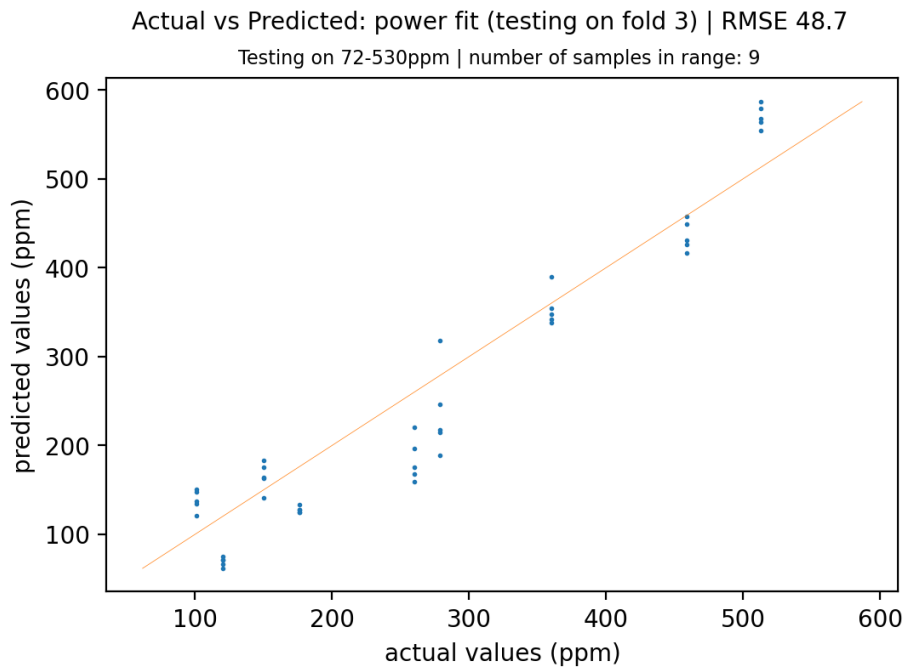


Figure S69: Predicted Li compositions using the high-Li model vs. the actual Li composition of the standards in the model's test set between 72–530 ppm. In this range, there were nine samples in the test set. The average RMSEP is 48.7. The orange line is the one-to-one line to help visualize the difference between the actual and predicted values.

Due to the variation in RMSEP with predicted value, we calculate the local RMSEP using the Python Hyperspectral Analysis Tools (PyHAT; Anderson et al., 2019; 2020) for a given Li composition between 0–530 ppm (Figure S71). Three parameters were used to optimize the rolling RMSEP output: window size, minimum number, and sigma. The minimum number of neighbors specifies the minimum number of test set predictions used to calculate the local RMSEP at a given point. The window size determines the range of test set predictions used around the simulated prediction. If there are fewer standards than the minimum number within the specified window, values from outside the window are used to reach the minimum. If there are a greater number of standards in the specified window than the minimum number, PyHAT will use all the values within the range of the window. Sigma is the standard deviation of the Gaussian smoothing that is applied in terms of number of points (the simulated prediction vector has 2000 points in it). The local RMSEP ranges from about 10 ppm at the lowest predicted values to 56 ppm at predicted values between 150–200 ppm (Figure S71).

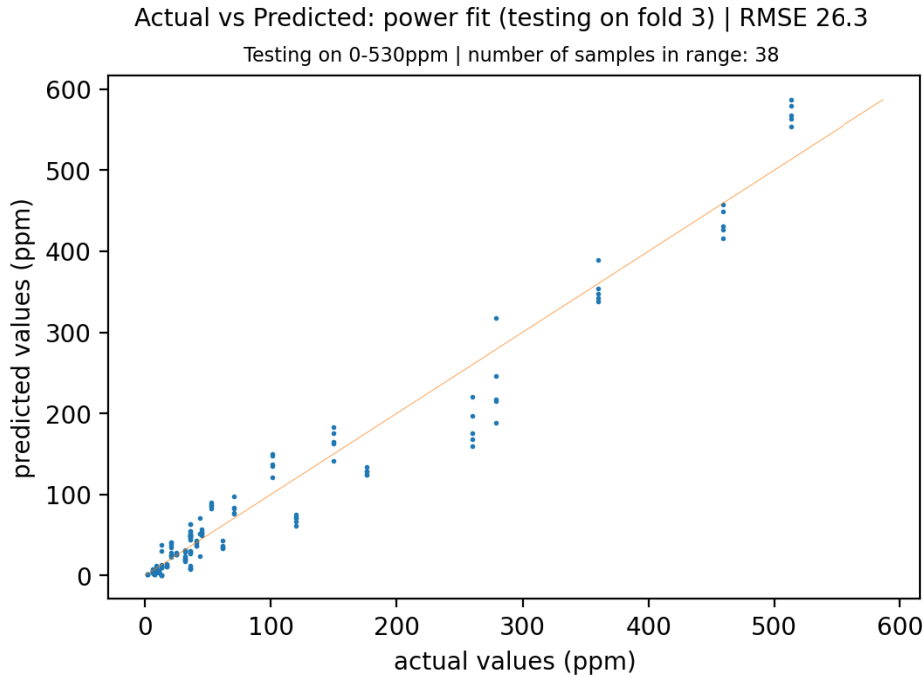


Figure S70: Predicted Li compositions using the high-Li model vs. the actual Li composition of the standards in the model's full test set. There are 38 samples total in the test set. The average RMSEP is  $\approx 26.3$ . The orange line is the one-to-one line to help visualize the difference between the actual and predicted values.

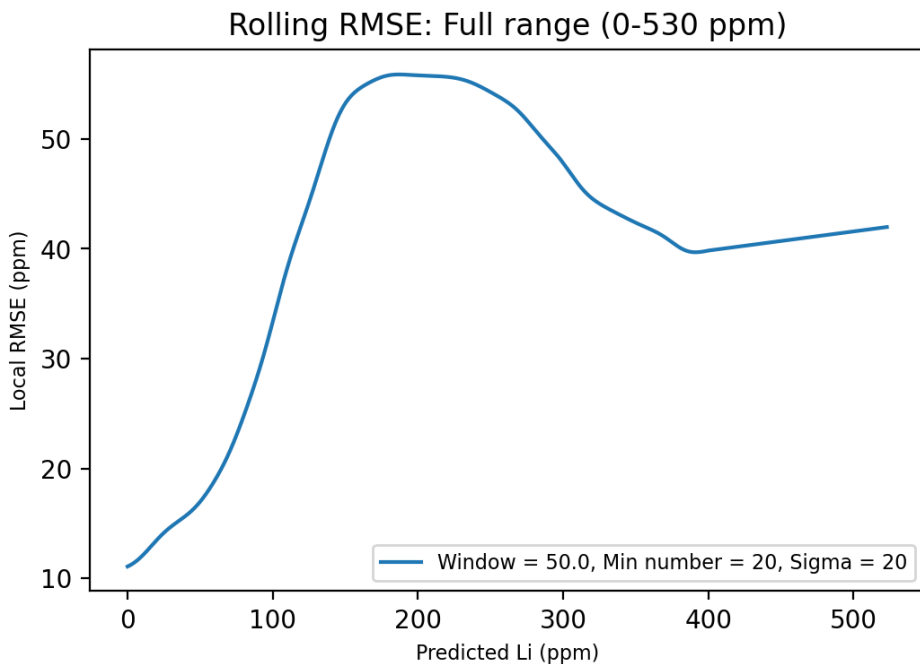


Figure S71: The local RMSEP for the range of predicted values between 0–530 ppm. We used a window size of 50 ppm with a minimum number of 20 samples. We smoothed the data using a sigma of 20.

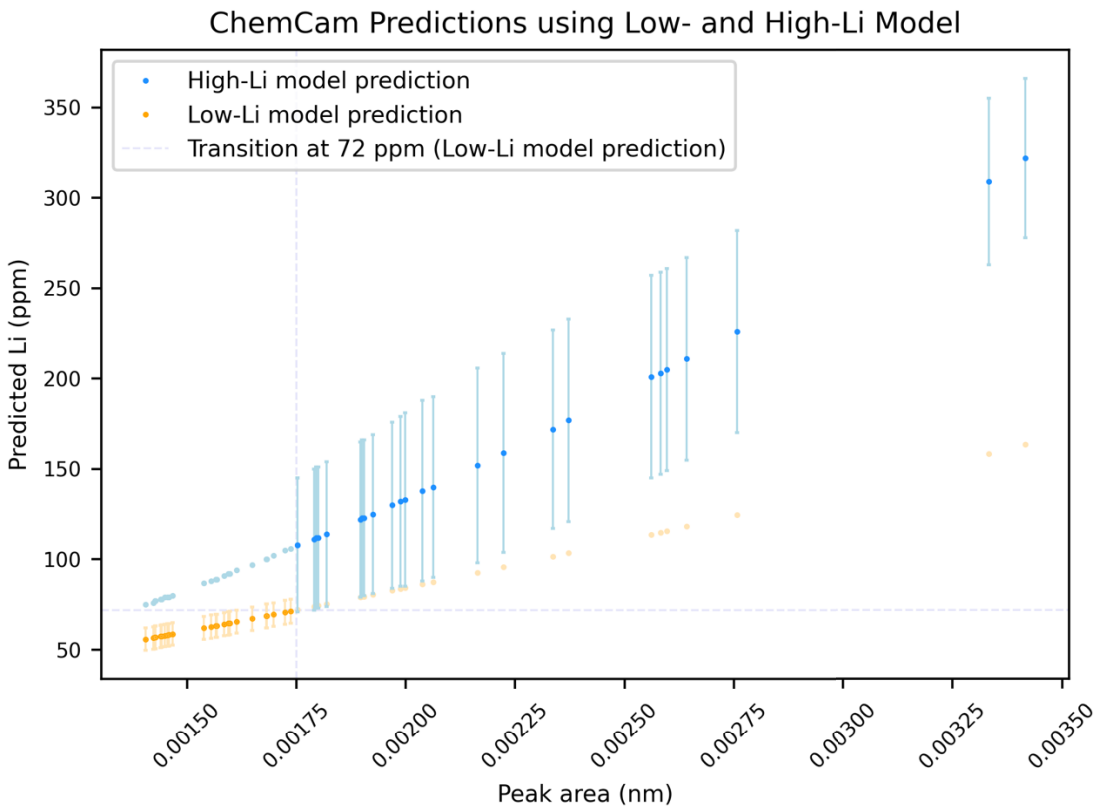


Figure S72: Transition between the low- and high-Li model at 0.00175 nm peak area (corresponding to the low-Li model prediction at its quantification limit of 72 ppm). The points shown are the 50 ChemCam targets with the highest Li peak areas. The section with dark blue points is where the high-Li model is used, while the section with bright orange points is where the low-Li model is used. The error bars represent 1 sigma (+/- the local RMSEP).

The RMSEP of the previous Li model by Payré et al. (2017a) ranges from about 5 ppm at 0 Li ppm to 6.5 ppm at 72 ppm (orange bars in Figure S72). The high-Li model has an RMSEP that varies between ~10 ppm and 23 ppm within that same range (0–72 ppm). Due to this difference in accuracy, the high-Li model will only be used to predict targets that were predicted to be above 72 ppm by the Payré et al. (2017a) model. The transition at 72 ppm corresponds to a peak area of ~0.00175 nm (Figure S72). It appears that the transition between the low and high Li models is not smooth—there is an offset by about 30 ppm at the transition zone (Figure S72). However, this difference between the two models in this transition region is still within the combined RMSEP of the predictions at the 1 sigma error level. Hence, these two models are consistent with each other.

The lithium laboratory calibration data and the local RMSEP of the Lithium calibration are included in the same dataset that contains the diagenesis data (Supplement Text S1) as \*.csv files. The local RMSEP file contains an index number vector, the Li Prediction (ppm) at each index value calculated in PyHAT, and the local RMSEP at each predicted value of Li (ppm) using a window size of 50 ppm, a minimum number of samples of 20, and a Gaussian smoothing parameter of 20.

### **Text S8. Unique Na and Mg Sulfate Compositions**

The target Hamnavoe was analyzed with 10 points (Figure S4) that produced a unique chemical composition. Figure S73 shows that point 4 has contribution by Ca-sulfate but points 1 and 9 are both uniquely enriched in MgO, Na<sub>2</sub>O, and S compared to host rock. In contrast, all other points on Hamnavoe plot close to average host rock composition. Point 9 and in particular point 1 may contain Mg-sulfate but have excess sulfate which could be attributed to Na-sulfate such as thenardite, or other hydrated Na sulfate mineral, given their enrichment in Na<sub>2</sub>O.

Figure S75 shows that both point 1 and 9 have relatively high Na<sub>2</sub>O content. It highlights in particular that for point 1, CaO is anticorrelated with MgO and Na<sub>2</sub>O content on the shot profile, while sulfate remains high, showing a mixture of sulfate phases, where Mg and Na-sulfate is intimately mixed but distinct to Ca-sulfate. These points are consistent with Mg and Na sulfates as it occurs naturally on Earth mixed in crystalline phases of various Na and Mg proportions.

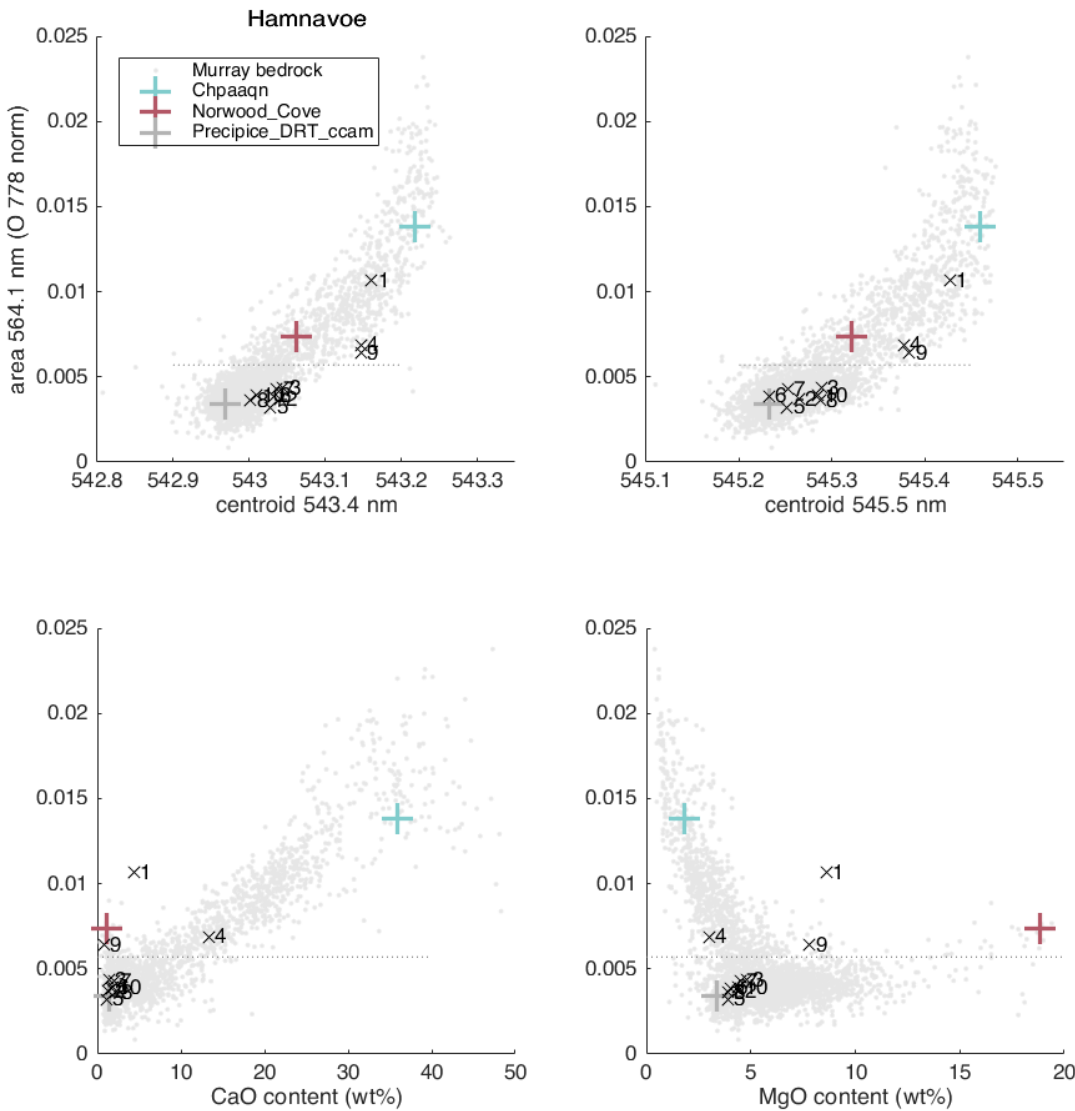


Figure S73: Sulfur signal observed on target Hamnavoe. Upper panels show sulfur signal intensity with centroid analysis as described in Rapin et al. 2019, showing that sulfur is above detection limit ( $\text{SO}_3 > 10 \text{ wt.\%}$ ) on points 1, 4 and 9. See spectra on figure S74 for detailed observations of the sulfur peaks. The two lower panels show that point 4 is pointing to a Ca-sulfate contribution mixed with host rock, but point 9 and 1 rather more likely contain Mg-sulfate along with excess sulfate, in particular for point 1, that could be present in another sulfate-bearing salt phase. This phase could correspond to a mixture of Na and Mg-sulfates as these points are particularly enhanced in  $\text{Na}_2\text{O}$  content compared to surrounding bedrock.

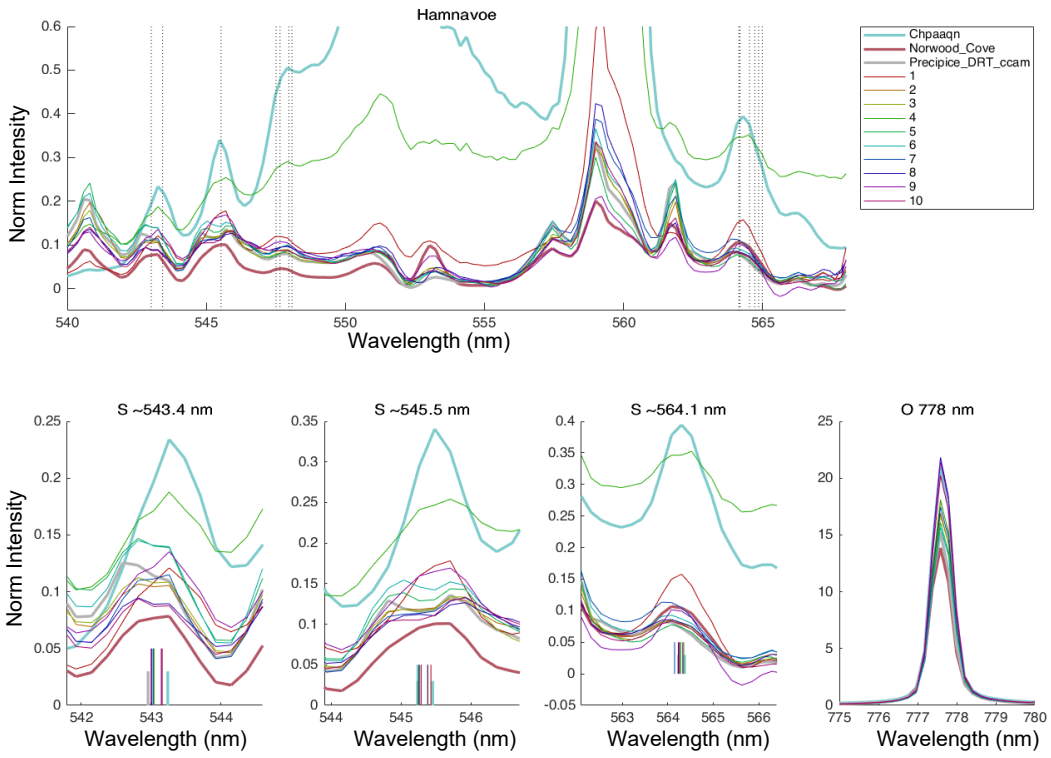


Figure S74: Sulfur region LIBS spectra for Hamanvœu compared to similar targets (Chpaaqn, Norwood Cove, Precipice DRT ccam). Sulfur signal as seen on average spectra for the 10 points on target Hamnavoe. Vertical dotted lines on upper panel show the location of sulfur peaks as identified in the NIST atomic lines database and observed on laboratory spectra. Lower panels show close-ups on areas where sulfur peaks can be measured, right most panel shows oxygen peak intensity used of normalization.

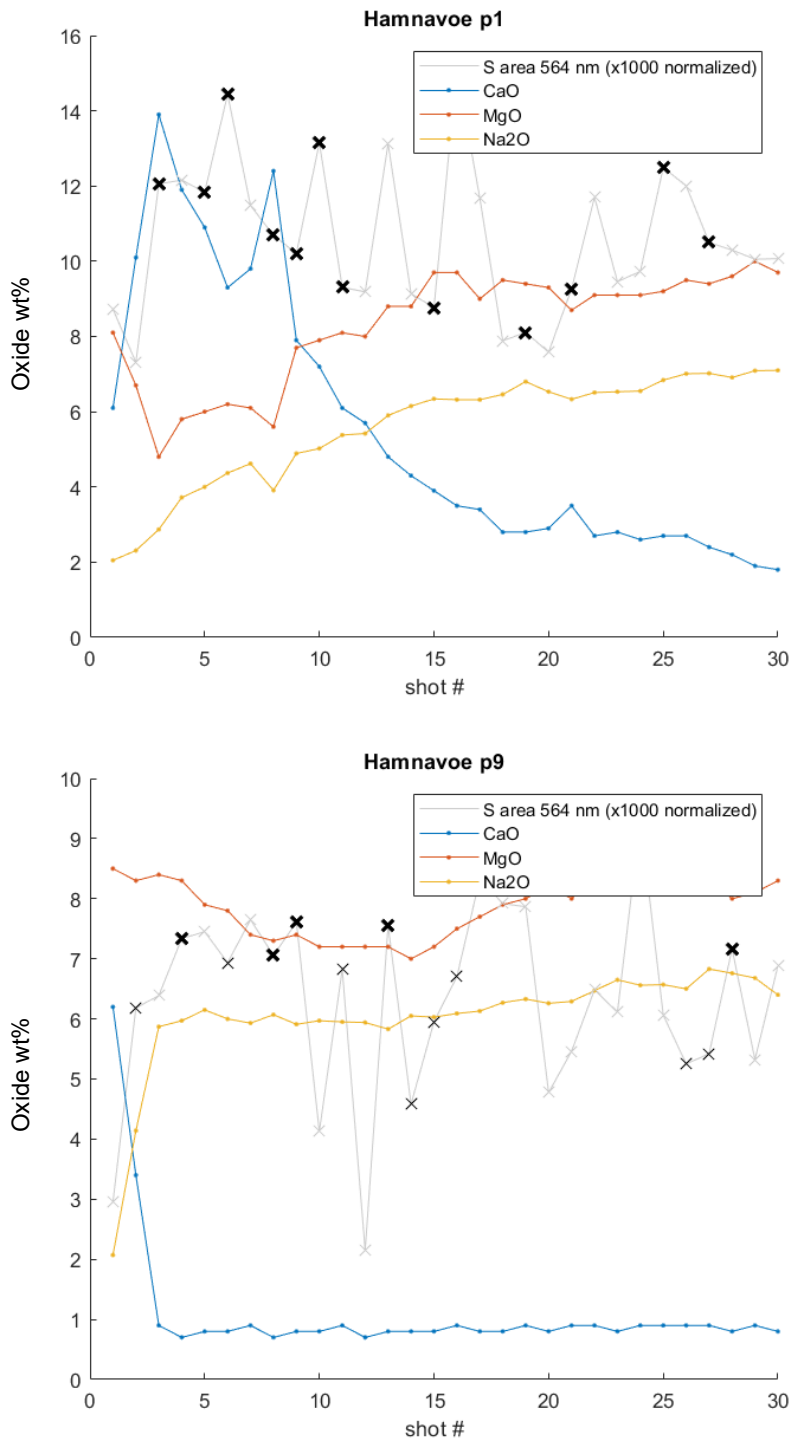


Figure S75: Shot to shot profile intensity for points 1 and 9 on Hamnavoe target. Grey line shows normalized sulfur peak intensity, with black crosses where the sulfur signal matches the peak is above the limit of detection and centroid and intensity values matches those used for calibration (Rapin et al 2019). See spectra on Figure S76 for detailed observations of the sulfur peaks.

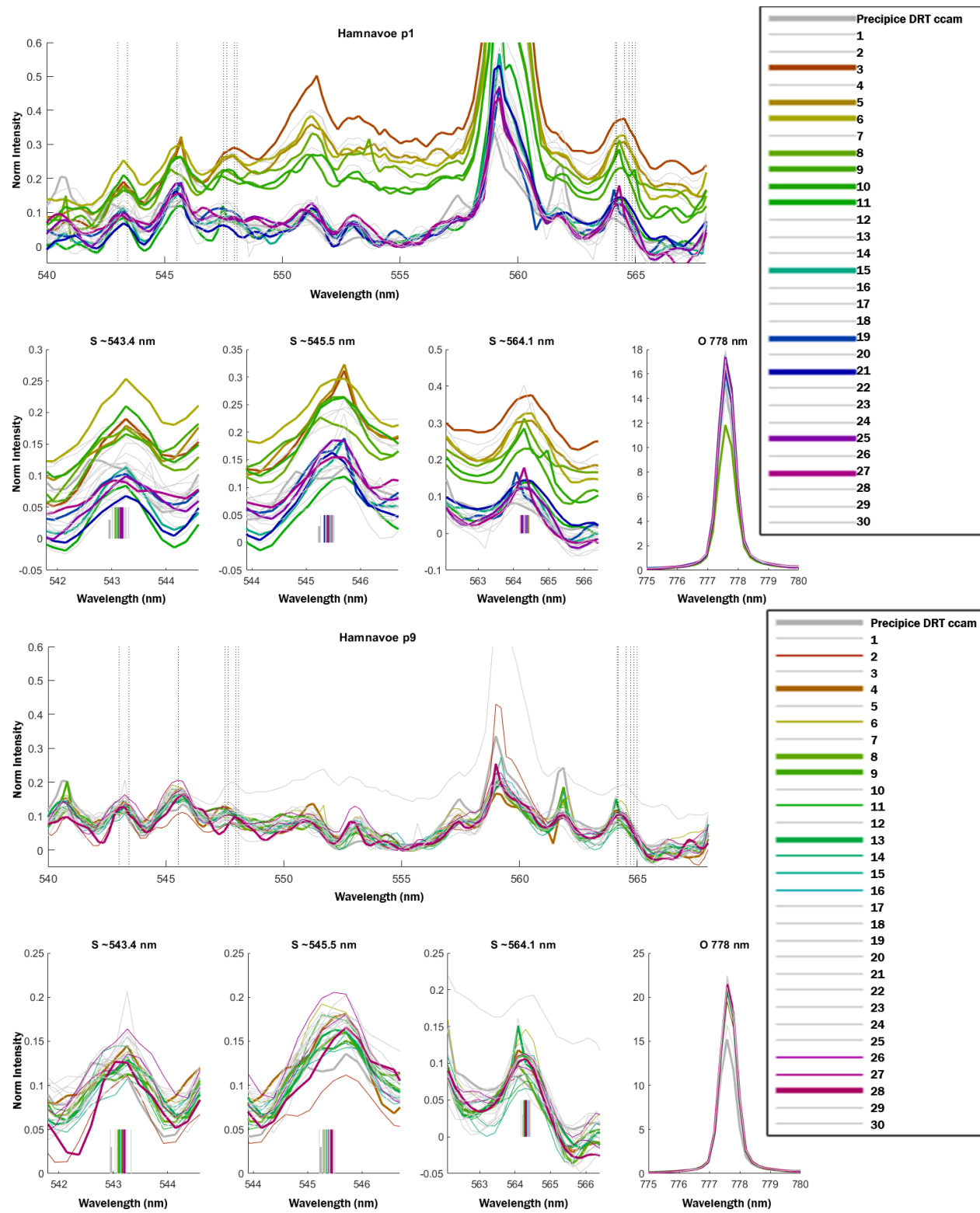


Figure S76: Shot to shot LIBS spectra for Hamanvooe observation point 1 and 9 compared to similar targets (Precipice DRT ccam) in the sulfur region. Bottom row of spectra show specific sulfur line positions and the oxygen line used for normalization.

### **Text S9. Mastcam and MAHLI Dataproducts in the Manuscript**

Figure 3 (main Mastcam mosaic) combines three mosaics from the same rover location on but on different sols (2570 and 2572): 2570ML0135000000706042E01, 2570ML0135000010706043E01, 2570ML0135000020706044E01, 2570ML0135000030706045E01, 2570ML0135000040706046E01, 2570ML0135000050706047E01; 2572ML0135080000706073C00, 2572ML0135080010706074C00, 2572ML0135080020706075C00, 2572ML0135080030706076C00, 2572ML0135080040706077C00, 2572ML0135080050706078C01, 2572ML0135080060706079C00, 2572ML0135080070706080C00, 2572ML0135080080706081C00, 2572ML0135080090706082C00, 2572ML0135080100706083C00, 2572ML0135080110706084C00; 2572MR0135070001100185C00, 2572MR0135070011100186C00, 2572MR0135070021100187C00, 2572MR0135070031100188C00, 2572MR0135070041100189C00, 2572MR0135070051100190C00, 2572MR0135070061100191C00, 2572MR0135070071100192C00, 2572MR0135070081100193C00, 2572MR0135070091100194C00, 2572MR0135070101100195C00, 2572MR0135070111100196C00, 2572MR0135070121100197C00, 2572MR0135070131100198C00, 2572MR0135070141100199C00, 2572MR0135070151100200C00, 2572MR0135070161100201C00, 2572MR0135070171100202C00, 2572MR0135070181100203C00.

Stonehive MAHLI (sol 2575) from ~5 cm standoff inset: 2575MH0003690000903949R00.

Figure 4 (main Mastcam mosaic) is a portion of the 360 degree panorama at the rover location from sol 2579: 2579ML0135470000506360C00, 2579ML0135470010506361C00, 2579ML0135470020506362C00, 2579ML0135470030506363C00, 2579ML0135470040506364C00, 2579ML0135470050506365C00, 2579ML0135470060506366C00, 2579ML0135470070506367C00, 2579ML0135470080506368C00, 2579ML0135470090506369C00, 2579ML0135470100506370C00, 2579ML0135470110506371C00, 2579ML0135470120506372C00, 2579ML0135470130506373C00, 2579ML0135470140506374C00, 2579ML0135470150506375C00, 2579ML0135470160506376C00, 2579ML0135470170506377C00, 2579ML0135470180506378C00, 2579ML0135470190506379C00, 2579ML0135470200506380C00, 2579ML0135470210506381C00, 2579ML0135470220506382C00, 2579ML0135470230506383C01, 2579ML0135470250506385C00, 2579ML0135470260506386C00, 2579ML0135470270506387C00, 2579ML0135470280506388C00, 2579ML0135470290506389C00, 2579ML0135470300506390C00, 2579ML0135470520506412C00, 2579ML0135470530506413C00, 2579ML0135470540506414C00, 2579ML0135470550506415C00, 2579ML0135470560506416C00, 2579ML0135470570506417C00, 2579ML0135470580506418C00, 2579ML0135470590506419C00, 2579ML0135470600506420C00, 2579ML0135470730506433C00, 2579ML0135470740506434C00, 2579ML0135470750506435C00, 2579ML0135470760506436C00, 2579ML0135470770506437C00, 2579ML0135470780506438C00, 2579ML0135470790506439C00, 2579ML0135470800506440C00, 2579ML0135470810506441C00, 2579ML0135470990506459C00, 2579ML0135471000506460C00, 2579ML0135471010506461C00, 2579ML0135471020506462C00, 2579ML0135471030506463C00, 2579ML0135471040506464C00, 2579ML0135471050506465C00, 2579ML0135471060506466C00, 2579ML0135471070506467C00, 2579ML0135471080506468C00, 2579ML0135471090506469C00, 2579ML0135471100506470C00, 2579ML0135471110506471C00, 2579ML0135471220506482C00, 2579ML0135471230506483C00, 2579ML0135471240506484C00, 2579ML0135471250506485C00, 2579ML0135471260506486C00, 2579ML0135471270506487C00.

Sourhope MAHLI (sol 2583) from ~3 cm standoff inset: 2583MH0001930000904254R00

Kincardineshire ChemCam target (sol 2585) inset colorized with Mastcam:

2586MR0135840001100596Coo

Gleneagles MAHLI (sol 2579) from ~5 cm standoff inset: 2579MH0001930000904029Roo

Black Gutter ChemCam target (sol 2581) inset colorized with Mastcam: 2581MR0135530001100433Coo

Figure 5 (main Mastcam mosaic) is a portion of a mosaic at the rover location from sol 2735:

2735ML0143310011004616Coo, 2735ML0143310021004617Coo, 2735ML0143310031004618Coo,

2735ML0143310041004619Coo, 2735ML0143310051004620Coo, 2735ML0143310061004621Coo,

2735ML0143310071004622Coo, 2735ML0143310081004623Coo, 2735ML0143310091004624Coo,

2735ML0143310101004625Coo, 2735ML0143310111004626Coo, 2735ML0143310121004627Coo,

2735ML0143310131004628Coo, 2735ML0143310141004629Coo, 2735MR0143310001200640Coo,

2735MR0143310011200641Coo, 2735MR0143310021200642Coo, 2735MR0143310031200643Coo,

2735MR0143310041200644Coo, 2735MR0143310051200645Coo, 2735MR0143310061200646Coo,

2735MR0143310071200647Coo, 2735MR0143310081200648Coo, 2735MR0143310091200649Coo,

2735MR0143310101200650Coo, 2735MR0143310111200651Coo, 2735MR0143310121200652Coo,

2735MR0143310131200653Coo, 2735MR0143310141200654Coo.

Bonxie ChemCam target (sol 2735) inset colorized with Mastcam: 2735MR0143310041200644Coo

Beinn an Dudhaich (sol 2737) and Beinn an Dudhaich 2 (sol 2740) ChemCam targets inset combines two colorized with Mastcam images from sol 2737 and 2741: 2737MR0143470001200690Coo,

2741MR0143700011200996Coo

Peach ChemCam target (sol 2740) inset colorized with Mastcam: 2741MR0143700021200997Coo

Ben Wyvis ChemCam target inset (sol 2738) colorized with Mastcam: 2738MR0143550001200766Coo

Figure 6 (main Mastcam mosaic) is a portion of the 360 degree panorama at the rover location from sol 2671: 2671ML0140070001002490Coo, 2671ML0140070011002491Coo, 2671ML0140070021002492Coo,

2671ML0140070031002493Coo, 2671ML0140070041002494Coo,

2671ML0140070051002495Coo, 2671ML0140070061002496Coo, 2671ML0140070071002497Coo,

2671ML0140070081002498Coo, 2671ML0140070091002499Coo, 2671ML0140070101002500Coo,

2671ML0140070111002501Coo, 2671ML0140070121002502Coo, 2671ML0140070131002503Coo,

2671ML0140070141002504Coo, 2671ML0140070151002505Coo, 2671ML0140070161002506Coo,

2671ML0140070171002507Coo, 2671ML0140070181002508Coo, 2671ML0140070191002509Coo,

2671ML0140070201002510Coo, 2671ML0140070211002511Coo, 2671ML0140070221002512Coo,

2671ML0140070231002513Coo, 2671ML0140070241002514Coo, 2671ML0140070251002515Coo,

2671ML0140070261002516Coo, 2671ML0140070271002517Coo, 2671ML0140070281002518Coo,

2671ML0140070291002519Coo, 2671ML0140070301002520Coo, 2671ML0140070311002521Coo,

2671ML0140070321002522Coo, 2671ML0140070331002523Coo, 2671ML0140070341002524Coo,

2671ML0140070351002525Coo, 2671ML0140070361002526Coo, 2671ML0140070371002527Coo,

2671ML0140070381002528Coo, 2671ML0140070391002529Coo, 2671ML0140070401002530Coo,

2671ML0140070411002531Coo, 2671ML0140070421002532Coo, 2671ML0140070431002533Coo,

2671ML0140070441002534Coo, 2671ML0140070451002535Coo, 2671ML0140070461002536Coo,

2671ML0140070471002537Coo, 2671ML0140070481002538Coo, 2671ML0140070491002539Coo,

2671ML0140070501002540Coo, 2671ML0140070511002541Coo, 2671ML0140070521002542Coo,

2671ML0140070531002543Coo, 2671ML0140070541002544Coo, 2671ML0140070551002545Coo,  
2671ML0140070561002546Coo, 2671ML0140070571002547Coo, 2671ML0140070581002548Coo,  
2671ML0140070591002549Coo, 2671ML0140070601002550Coo, 2671ML0140070611002551Coo,  
2671ML0140070621002552Coo, 2671ML0140070631002553Coo, 2671ML0140070641002554Coo,  
2671ML0140070651002555Coo, 2671ML0140070661002556Coo, 2671ML0140070671002557Coo,  
2671ML0140070681002558Coo, 2671ML0140070691002559Coo, 2671ML0140070701002560Coo,  
2671ML0140070711002561Coo, 2671ML0140070721002562Coo, 2671ML0140070731002563Coo,  
2671ML0140070741002564Coo, 2671ML0140070751002565Coo, 2671ML0140070761002566Coo,  
2671ML0140070771002567Coo, 2671ML0140070781002568Coo, 2671ML0140070791002569Coo,  
2671ML0140070801002570Coo, 2671ML0140070811002571Coo, 2671ML0140070821002572Coo,  
2671ML0140070831002573Coo, 2671ML0140070841002574Coo, 2671ML0140070851002575Coo,  
2671ML0140070861002576Coo, 2671ML0140070871002577Coo, 2671ML0140070881002578Coo,  
2671ML0140070891002579Coo, 2671ML0140070901002580Coo, 2671ML0140070911002581Coo,  
2671ML0140070921002582Coo, 2671ML0140070931002583Coo, 2671ML0140070941002584Coo,  
2671ML0140070951002585Coo, 2671ML0140070961002586Coo, 2671ML0140070971002587Coo,  
2671ML0140070981002588Coo, 2671ML0140070991002589Coo, 2671ML0140071001002590Coo,  
2671ML0140071011002591Coo, 2671ML0140071021002592Coo, 2671ML0140071031002593Coo,  
2671ML0140071041002594Coo, 2671ML0140071051002595Coo, 2671ML0140071061002596Coo,  
2671ML0140071071002597Coo, 2671ML0140071081002598Coo, 2671ML0140071091002599Coo,  
2671ML0140071101002600Coo, 2671ML0140071111002601Coo, 2671ML0140071121002602Coo,  
2671ML0140071131002603Coo, 2671ML0140071141002604Coo, 2671ML0140071151002605Coo,  
2671ML0140071161002606Coo, 2671ML0140071171002607Coo, 2671ML0140071181002608Coo,  
2671ML0140071191002609Coo, 2671ML0140071201002610Coo, 2671ML0140071211002611Coo,  
2671ML0140071221002612Coo, 2671ML0140071231002613Coo, 2671ML0140071241002614Coo,  
2671ML0140071251002615Coo.

Roxburghshire ChemCam target (sol 2670) inset colorized with Mastcam:

2670MR0140030000804326Coo

Glen Rosa (sol 2686) and Glen Rosa DP (sol 2691) ChemCam targets inset combines two colorized with Mastcams from sol 2686 and 2691: 2686MR0140600060604796Coo, 2691MR0140760000604809Coo

Figure 7 (main Mastcam mosaic) is two portons of the 360 degree panorama at the rover location from sol 2831: 2831ML0148180000108777Coo, 2831ML0148180010108778Coo,  
2831ML0148180020108779Coo, 2831ML0148180030108780Coo, 2831ML0148180040108781Coo,  
2831ML0148180050108782Coo, 2831ML0148180060108783Coo, 2831ML0148180070108784Coo,  
2831ML0148180080108785Coo, 2831ML0148180090108786Coo, 2831ML0148180100108787Coo,  
2831ML0148180110108788Coo, 2831ML0148180120108789Coo, 2831ML0148180130108790Coo,  
2831ML0148180140108791Coo, 2831ML0148180150108792Coo, 2831ML0148180160108793Coo,  
2831ML0148180170108794Coo, 2831ML0148180180108795Coo, 2831ML0148180190108796Coo,  
2831ML0148180200108797Coo, 2831ML0148180210108798Coo, 2831ML0148180350108812Coo,  
2831ML0148180360108813Coo, 2831ML0148180370108814Coo, 2831ML0148180380108815Coo,  
2831ML0148180390108816Coo, 2831ML0148180400108817Coo, 2831ML0148180410108818Coo,  
2831ML0148180420108819Coo, 2831ML0148180430108820Coo, 2831ML0148180440108821Coo,

2831ML0148180450108822Coo, 2831ML0148180460108823Coo, 2831ML0148180470108824Coo,  
2831ML0148180480108825Coo, 2831ML0148180490108826Coo, 2831ML0148180500108827Coo,  
2831ML0148180510108828Coo, 2831ML0148180520108829Coo, 2831ML0148180530108830Coo,  
2831ML0148180540108831C01, 2831ML0148180550108832Coo, 2831ML0148180560108833Coo,  
2831ML0148180570108834Coo, 2831ML0148180580108835Coo, 2831ML0148180590108836Coo,  
2831ML0148180600108837Coo, 2831ML0148180610108838Coo, 2831ML0148180620108839Coo,  
2831ML0148180630108840Coo, 2831ML0148180640108841Coo, 2831ML0148180650108842Coo,  
2831ML0148180660108843Coo, 2831ML0148180670108844Coo, 2831ML0148180680108845Coo,  
2831ML0148180690108846Coo, 2831ML0148180700108847Coo, 2831ML0148180710108848Coo,  
2831ML0148180720108849Coo, 2831ML0148180730108850Coo, 2831ML0148180740108851Coo,  
2831ML0148180750108852Coo, 2831ML0148180760108853Coo, 2831ML0148180770108854Coo,  
2831ML0148180780108855Coo, 2831ML0148180790108856Coo, 2831ML0148180800108857Coo,  
2831ML0148180810108858Coo, 2831ML0148180820108859Coo, 2831ML0148180830108860Coo,  
2831ML0148180840108861Coo, 2831ML0148180850108862Coo, 2831ML0148180860108863Coo,  
2831ML0148180870108864C01, 2831ML0148180880108865Coo, 2831ML0148180890108866Coo,  
2831ML0148180900108867Coo, 2831ML0148180910108868Coo, 2831ML0148180920108869Coo,  
2831ML0148180930108870Coo, 2831ML0148180940108871Coo, 2831ML0148180950108872Coo,  
2831ML0148180960108873Coo, 2831ML0148180970108874Coo, 2831ML0148180980108875Coo,  
2831ML0148180990108876Coo, 2831ML0148181000108877Coo, 2831ML0148181010108878Coo,  
2831ML0148181020108879Coo, 2831ML0148181030108880Coo, 2831ML0148181040108881Coo,  
2831ML0148181050108882Coo, 2831ML0148181060108883Coo, 2831ML0148181070108884Coo,  
2831ML0148181080108885Coo, 2831ML0148181090108886Coo, 2831ML0148181100108887Coo,  
2831ML0148181110108888Coo, 2831ML0148181120108889Coo, 2831ML0148181130108890Coo,  
2831ML0148181140108891Coo, 2831ML0148181150108892Coo, 2831ML0148181160108893C01,  
2831ML0148181170108894Coo, 2831ML0148181180108895Coo, 2831ML0148181190108896Coo,  
2831ML0148181200108897Coo, 2831ML0148181210108898Coo, 2831ML0148181220108899Coo,  
2831ML0148181230108900Coo, 2831ML0148181240108901Coo, 2831ML0148181250108902Coo.

Ayton MAHLI (sol 2857) from ~3 cm standoff inset: 2857MH0008140021003309Coo

Foulden ChemCam target (sol 2867) inset colorized with Mastcam: 2867MR0149570000505548Coo

Mary Anning ChemCam target (sol 2831) inset colorized with Mastcam: 2833MR0148220450704611Coo